

DEVELOPMENT AND CHARACTERIZATION OF NEW LAYERED  
CATHODE MATERIALS FOR LITHIUM ION BATTERIES

A THESIS SUBMITTED TO  
THE GRADUATE SCHOOL OF NATURAL AND APPLIED SCIENCES  
OF  
MIDDLE EAST TECHNICAL UNIVERSITY

BY

BERKE PİŞKİN

IN PARTIAL FULFILLMENT OF THE REQUIREMENTS  
FOR  
THE DEGREE OF DOCTOR OF PHILOSOPHY  
IN  
METALLURGICAL AND MATERIALS ENGINEERING

APRIL 2018



Approval of the thesis:

**DEVELOPMENT AND CHARACTERIZATION OF NEW LAYERED  
CATHODE MATERIALS FOR LITHIUM ION BATTERIES**

submitted by **BERKE PİŞKİN** in partial fulfillment of the requirements for the degree of **Doctor of Philosophy in Metallurgical and Materials Engineering Department, Middle East Technical University** by,

Prof. Dr. Halil KALIPÇILAR  
Dean, Graduate School of **Natural and Applied Sciences** \_\_\_\_\_

Prof. Dr. C. Hakan GÜR  
Head of Department,  
**Metallurgical and Materials Engineering** \_\_\_\_\_

Prof. Dr. M. Kadri AYDINOL  
Supervisor,  
**Metallurgical and Materials Engineering Dept., METU** \_\_\_\_\_

**Examining Committee Members:**

Prof. Dr. Tayfur ÖZTÜRK  
Metallurgical and Materials Engineering Dept., METU \_\_\_\_\_

Prof. Dr. M. Kadri AYDINOL  
Metallurgical and Materials Engineering Dept., METU \_\_\_\_\_

Prof. Dr. Ali Arslan KAYA  
Metallurgical and Materials Engineering Dept.,  
Muğla Sıtkı Koçman University \_\_\_\_\_

Prof. Dr. Servet TURAN  
Materials Science and Engineering Dept.,  
Anadolu University \_\_\_\_\_

Assoc. Prof. Dr. Y. Eren KALAY  
Metallurgical and Materials Engineering Dept., METU \_\_\_\_\_

**Date:** 30.04.2018

**I hereby declare that all information in this document has been obtained and presented in accordance with academic rules and ethical conduct. I also declare that, as required by these rules and conduct, I have fully cited and referenced all material and results that are not original to this work.**

Name, Last name: Berke, Pişkin

Signature :

## ABSTRACT

### DEVELOPMENT AND CHARACTERIZATION OF NEW LAYERED CATHODE MATERIALS FOR LITHIUM ION BATTERIES

Pişkin, Berke

Ph.D., Department of Metallurgical and Materials Engineering

Supervisor: Prof. Dr. M. Kadri Aydınol

April 2018, 128 pages

In the present study, the effects of Ni:Mn:Co mole ratio and doping elements, i.e. Mo, W, Ag and Cu, in  $\text{Li}(\text{Ni}_x\text{Mn}_y\text{Co}_{1-x-y-z}\text{M}_z)\text{O}_2$  (NMC) were systematically investigated as cathode materials for Li-ion batteries.  $\text{Li}(\text{Ni}_{1/3}\text{Mn}_{1/3}\text{Co}_{1/3})\text{O}_2$  (NMC-111),  $\text{Li}(\text{Ni}_{0.2}\text{Mn}_{0.2}\text{Co}_{0.6})\text{O}_2$  (NMC-226),  $\text{Li}(\text{Ni}_{0.6}\text{Mn}_{0.2}\text{Co}_{0.2})\text{O}_2$  (NMC-622),  $\text{Li}(\text{Ni}_{0.2}\text{Mn}_{0.6}\text{Co}_{0.2})\text{O}_2$  (NMC-262) and their doped compositions were synthesized via spray pyrolysis. Spray pyrolysis method was used to attain a spherical fine-sized morphology in the powders synthesized. This procedure was followed by a heat-treatment to provide well-defined splitting of (006)/(102) and (108)/(110) diffraction peaks in XRD spectra as an indicator for layered structure and good hexagonal ordering. SEM and TEM studies were carried out to investigate the structural properties of the powders synthesized. XRD analyses were performed to reveal the present phases in the structure, while XPS analyses were carried out to identify surface chemistry. Moreover, ICP-MS was employed so as to quantify the contents of elements in the powders. Galvanostatic tests and EIS were carried out to examine the electrochemical performance of NMC cathode materials. Of the undoped NMC cathode materials, NMC-111 performed relatively lower cation mixing in the structure

leading highest discharge capacity. In the doped compositions, Mo-doped cathode materials in all Ni:Mn:Co mole ratio exhibited relatively lower cation mixing together with the wider Li-gap. This was also valid for all 622 compositions independent from the doping elements, except W. The cathode materials which had a low cation mixing, while having a wide Li-gap were performed better discharge capacity and capacity retention up to  $140 \text{ mAhg}^{-1}$  and  $\sim 80\%$ , respectively in the 2.7-4.2 V potential window.

The morphology of the powder might be considered as another factor affecting the electrochemical performance. In the structural investigations, two type of particle formation was observed; one was spherical aggregates having large and loose primary particles and the second was spherical aggregates having small and relatively denser particles. The morphology of loose aggregates with relatively larger particles was determined in the cathode materials, e.g. 622-Mo, that were performed higher discharge capacity with a lower internal resistance. This structure provided a higher effective surface area to participate in the electrochemical reactions. This high surface area allowed the intercalation/deintercalation of Li-ions took place at a shorter diffusion time.

Present findings revealed the how the doping elements and the Ni:Mn:Co content affect the electrochemical performance and the structure stability of the NMC cathode materials.

**Keywords:** Lithium-Ion Batteries, Spray Pyrolysis, Doping, Electrochemical Characterization

## ÖZ

### LİTYUM İYON BATARYALAR İÇİN YENİ TABAKALI KATOT MALZEMELERİNİN GELİŞTİRİLMESİ VE KARAKTERİZASYONU

Pişkin, Berke

Doktora, Metalurji ve Malzeme Mühendisliği Bölümü

Tez Yöneticisi: Prof. Dr. M. Kadri Aydınol

Nisan 2018, 128 sayfa

Bu çalışmada,  $\text{Li}(\text{Ni}_x\text{Mn}_y\text{Co}_{1-x-y})\text{O}_2$  (NMC) içerisindeki Ni:Mn:Co mol oranı ve Mo, W, Ag ve Cu katkı elementlerinin bu kompozisyonlardaki etkileri, Li-iyon piller için sistematik olarak incelenmiştir.  $\text{Li}(\text{Ni}_{1/3}\text{Mn}_{1/3}\text{Co}_{1/3})\text{O}_2$  (NMC-111),  $\text{Li}(\text{Ni}_{0.2}\text{Mn}_{0.2}\text{Co}_{0.6})\text{O}_2$  (NMC-226),  $\text{Li}(\text{Ni}_{0.6}\text{Mn}_{0.2}\text{Co}_{0.2})\text{O}_2$  (NMC-622) ve  $\text{Li}(\text{Ni}_{0.2}\text{Mn}_{0.6}\text{Co}_{0.2})\text{O}_2$  (NMC-262) ve bu malzemelerin katkılı kompozisyonları sprey piroliz ile sentezlenmiştir. Sprey piroliz yöntemi, küresel yapıda ince tane boyutu dağılımına sahip tozlar elde etmek için kullanılmıştır. Bu prosesi takiben, tabakalı yapı ve düzgün hekzagonal yapının bir göstergesi olan net bir şekilde ayrılmış (006)/(102) ve (108)/(110) kırınım piklerinin elde edilmesi için ısıtma işlemi uygulanmıştır. Sentezlenen tozların yapısal özelliklerini incelemek için SEM ve TEM çalışmaları yapılmıştır. Yapıdaki mevcut fazları ortaya belirlemek için XRD analizleri yapılmış, yüzey kimyası için XPS analizleri yapılmıştır. Ayrıca, tozlar içindeki elementlerin içeriğini ölçmek için ICP-MS kullanılmıştır. NMC katotlarının elektrokimyasal performansını incelemek için galvanostatik testler ve EIS ölçümleri yapılmıştır. Katkısız NMC katotlarından, NMC-111 diğer katkısız katot malzemelerine oranla, yapıda daha az katyon karışımı göstermiştir ve bu durumla

birlikte en yüksek deşarj kapasitesine sahiptir. Katkılı kompozisyonlardan, tüm Ni:Mn:Co mol oranlarındaki Mo-katkılı katotlar, daha geniş Li aralığı ile birlikte nispeten düşük katyon karışımına sahiptir. Bu bulgu, aynı zamanda W dışındaki diğer katkı elementlerinden bağımsız olarak tüm 622 kompozisyonları için de geçerlidir. Düşük katyon karışımı ve daha geniş Li aralığını sergileyen katotlar, 2.7-4.2V potansiyel aralığında 140 mAhg<sup>-1</sup> e kadar deşarj kapasitesi gösterirken, kapasitesini çevrim sonunda ~% 80' e kadar koruduğu gözlemlenmiştir.

Elektrokimyasal performansı etkileyen bir diğer unsurun toz morfolojisi olduğu da gözlemlenmiştir. Toz yapısının incelemek üzere yapılan araştırmalar sonucunda, iki tip parça oluşumu gözlemlenmiştir. Bunlardan biri, daha büyük parçacıklara sahip olan daha boşluklu küresel kümeleşmiş parçalardır. İkincisi ise, daha küçük parça boyutuna sahip oranla daha sıkı yapıya sahip olan küresel parçalardır. Daha boşluklu ve nispeten iri parçalara sahip olan katotlarda, 622-Mo örneğinde olduğu gibi, daha düşük direnç ve yüksek deşarj kapasitesi gözlemlenmiştir. Bu yapının, elektrokimyasal reaksiyonlara katılmak için daha yüksek etkili yüzey alanı sağladığı düşünülmektedir. Gözlemlenen yüksek yüzey alanının, Li-iyonlarının interkalasyon/deinterkalasyonunun daha kısa bir difüzyon zamanında gerçekleşmesine izin vermiştir.

Mevcut bulgular, katkı elementlerinin ve Ni:Mn:Co içeriğinin, NMC katotlarının elektrokimyasal performansa ve yapı kararlılığına nasıl etki ettiğini ortaya koymuştur.

**Anahtar Kelimeler:** Lityum – İyon Bataryalar, Sprey piroliz, katkılandırma, elektrokimyasal karakterizasyon

*To Fatih Pişkin*

## ACKNOWLEDGEMENTS

I would like to express my gratitude to my supervisor, Prof. Dr. M. Kadri Aydınol for his guidance, advice, support, encouragement and valuable suggestions throughout the course of the studies.

I would like to thank my labmates for their support and sharing their knowledge and experience without stinting; especially Cansu Savaş, Ayşegül Afal Geniş, Burcu Arslan and Kadir Özgün Köse. I also would like to thank Atıl Büyükburç for his guidance and support during this period. Thanks are also to Serkan Yılmaz for his patience and support during SEM and grateful TEM studies.

I would also like to thank Stavros Salapatas Professor of Materials Science and Engineering, Carl V. Thompson, due to giving the opportunity to work in his research group, Materials for Micro and Nano Systems group at the Massachusetts Institute of Technology (MIT) and also his guidance and support. This research was supported by TUBITAK with a scholarship under 2214-A International Doctoral Research Fellowship Programme, Grant No. 1059B141501226.

Besides, thanks to my family, especially my sister for their support, encouragement, and trust in me throughout my life.

I would also like to acknowledge METU Central Laboratory for ICP-MS, XPS and BET analysis.

Finally, very special thanks to Fatih Pişkin, for his endless love, encouragement, patience, advice, and support during my thesis studies. I am very grateful for his support and answers to my unlimited questions and every problem.

## TABLE OF CONTENTS

ABSTRACT.....	v
ÖZ .....	vii
ACKNOWLEDGEMENTS .....	x
TABLE OF CONTENTS .....	xi
LIST OF TABLES .....	xiii
LIST OF FIGURES .....	xiv
LIST OF ABBREVIATIONS .....	xx
CHAPTERS	
1. INTRODUCTION .....	1
2. LITERATURE SURVEY .....	5
2.1 Cathode Materials .....	5
2.1.1 Layered ( $\alpha$ -NaFeO <sub>2</sub> ) Structure .....	9
2.1.2 Spinel Structure .....	12
2.1.3 Olivine Structure .....	12
2.2 Lithium Nickel Manganese Cobalt Oxide .....	15
2.3 Synthesis Methods for NMC Cathode materials .....	21
2.3.1 Powder Synthesis via Spray Pyrolysis .....	24
3. EXPERIMENTAL PROCEDURE .....	27
3.1 Synthesis of Li(Ni <sub>x</sub> Mn <sub>y</sub> Co <sub>1-x-y</sub> )O <sub>2</sub> .....	27
3.2 Electrode fabrication and cell configuration.....	28
3.3 Structural Characterization .....	29
3.4 Chemical Characterization.....	30
3.5 Electrochemical Characterization .....	31
4. RESULTS AND DISCUSSION .....	35
4.1 Processing Preliminary Parameters .....	35
4.1.1 Selection of Precursors.....	36

4.1.2 Determination of Additives.....	38
4.1.3 Carrier Gas .....	41
4.1.4 Reaction Temperature and Post-Heat-treatment.....	43
4.1.5 Determination of Doping Replacement .....	55
4.2 Structural Characterization Results .....	58
4.2.1 NMC Cathode materials .....	58
4.2.2 Doped NMC cathode materials.....	62
4.3 Chemical Characterization Results.....	76
4.3.1 NMC Cathode materials .....	76
4.3.2 Doped NMC.....	79
4.4 Electrochemical Characterization Results .....	86
4.4.1 NMC Cathode materials .....	86
4.4.2 Doped NMC.....	90
5. CONCLUSIONS.....	101
REFERENCES .....	105
APPENDICES	
A. PERMISSION LICENSES .....	125
CURRICULUM VITAE.....	127

## LIST OF TABLES

### TABLES

Table 1. Properties of cathode materials in commercial lithium-ion batteries. ....	13
Table 2. Parameters tried to be optimized during preliminary experiments. ‘A’ and ‘N’ are used to abbreviate acetate and nitrate salts of Li, Ni, Mn, and Co, respectively. ....	28
Table 3. Spray pyrolysis parameters optimized. ....	35
Table 4. The lattice parameters, oxygen positions and Li-gap size of all synthesized cathode materials. ....	48
Table 5. First discharge capacities of synthesized cathode materials. ....	54
Table 6. The precursor of dopants using experiments. ....	55
Table 7. Ionic radii of elements used in the current study, in an octahedrally coordinated oxygen environment. ....	56
Table 8. Lattice parameters and oxygen positions refined of NMC cathode materials. ....	59
Table 9. Refined lattice parameters and oxygen positions of doped NMC layered cathode materials. ....	65
Table 10. Compositions of doped NMC layered cathode materials. ....	80
Table 11. Electrochemical Properties of the layered NMC cathode materials. ....	88
Table 12. The first discharge capacity of the doped NMC-111, NMC-622 and NMC-226 layered cathode materials and their capacity retention after cycles. ....	92
Table 13. Equivalent circuit values of impedance fittings for the electrodes ( $\tau$ is the time constant). ....	96

## LIST OF FIGURES

### FIGURES

Figure 1. Safety, capacity and cost change with varieties of the composition. ....	3
Figure 2. The dendrite formation on lithium anode [19]. ....	5
Figure 3. Schematic diagram showing the intercalation of lithium in graphite. ....	6
Figure 4. Diagram of Li-ion cell during charging and discharging [21]. ....	6
Figure 5. Reversible lithium storage mechanisms in Li-ion batteries [23]. ....	7
Figure 6. Structure of common cathode materials in Li-ion batteries; a) layered ( $\alpha$ -NaFeO <sub>2</sub> ) structure, b) spinel structure and c) olivine structure. ....	8
Figure 7. Schematics of the lithium intercalation pathways in a) 1-D, b) 2-D, and c) 3-D structures. ....	8
Figure 8. General comparison of commonly used cathode materials (adapted from website of Battery University [58]). ....	13
Figure 9. Voltage versus capacity for cathode and anode materials [59]. ....	14
Figure 10. Changes at the anode/electrolyte interface [39]. ....	14
Figure 11. Degradation mechanisms of composite cathode materials [60]. ....	15
Figure 12. Rietveld refinement data of LiNi <sub>1/3</sub> Mn <sub>1/3</sub> Co <sub>1/3</sub> O <sub>2</sub> [68]. ....	16
Figure 13. Schematic representation of the droplet-to-solid particle conversion route during spray pyrolysis process (adapted from [129,130]). ....	24
Figure 14. Schematic of spray pyrolysis system. ....	27
Figure 15. Schematic illustration of Li-gap in NMC structure. ....	29
Figure 16. Deconvolution of EIS spectra proposed by Barsoukov <i>et al.</i> , [137]. ....	31
Figure 17. Equivalent circuit models used in the study, where R <sub>el</sub> is electrolyte resistance, R <sub>CT</sub> is charge transfer resistance. Eventually, Q <sub>DL</sub> represents the constant phase element for the double layer and W <sub>FSW</sub> the finite space Warburg element for Li-ion diffusion. ....	32

Figure 18. XRD spectra of NMC-111 cathode materials produced using acetates and nitrate salts. ....	36
Figure 19. SEM images of NMC-111 cathode materials produced by a) ANAA, and b) NNNN. Here, “A” represents the acetate salt as a precursor for the respective metal, where “N” stands for nitrate salts.....	37
Figure 20. SEM images of NMC cathode materials produced at 600°C with a) no additive, with b) both 0.1M CA and EG, and with c) both 0.3M EG and CA.....	38
Figure 21. SEM images of NMC cathode materials synthesized with an addition of 0.1 M EG and 0.05 M CA at 600°C.....	40
Figure 22. SEM images of NMC cathode materials produced with an additive of a) 0.1M oxalic acid, b) 0.1 M DMF c) 0.3 M DMF and d) 1 M DMF.....	41
Figure 23. XRD spectrum of NMC cathode synthesized under a) argon, and b) oxygen atmosphere.....	42
Figure 24. XRD patterns of the NMC cathode materials as-synthesized at 500°C, 600°C, and 800°C and post heat-treated at 800°C. ....	43
Figure 25. XRD patterns of layered NMC-111 cathode materials produced by spray pyrolysis and then post heat-treated at 800 °C, 900 °C, and 1000 °C. ....	44
Figure 26. SEM images of NMC-111 cathode materials heat-treated at a) 800 °C for 2h, b) 800 °C for 4h, c) 800 °C for 8h, d) 900 °C for 2h, e) 900 °C for 4h, f) 900 °C for 8h, g) 1000 °C for 2h, h) 1000 °C for 4h and i) 1000 °C for 8h. ....	45
Figure 27. X-ray pattern of cathode materials heat-treated at 800°C for 2, 4, 8, 12 and 20h.....	47
Figure 28. X-ray pattern of cathode materials with 5% excess Li heat-treated at 800 °C for 2, 4, 8, 12 and 20h.....	47
Figure 29. SEM images of cathode materials heat-treated at 800°C for 2h (a,b), 4h (c,d), 8h (e,f), 12h (g,h) and 20h (i, j). ....	49
Figure 30. SEM images of synthesized cathode materials heat-treated using excess amount of Li at 800°C for 2h (a,b), 4h (c,d), 8h (e,f), 12h (g,h) and 20h (i, j). ....	50
Figure 31. Particle size distribution of NMC-111 heat-treated at 800 °C for 2, 4, 8, 12 and 20h.....	51

Figure 32. Particle size distribution of NMC-111 prepared using an excess amount of Li, heat-treated at 800 °C for 2, 4, 8, 12 and 20h. ....	51
Figure 33. Voltage profiles of all samples, charged and discharged at 0.1C.....	52
Figure 34. Voltage profiles of all excess amount of Li samples, charged and discharged at 0.1C.....	52
Figure 35. Comparison of charge-discharge tests of NMC-111 heat-treated at 800°C for 2, 4, 8,12 and 20h. ....	53
Figure 36. Comparison of charge-discharge tests of NMC-111 heat-treated using an excess amount of Li at 800°C for 2, 4, 8,12 and 20h.....	53
Figure 37. XRD pattern of NMC-111 doped with selected elements yielding secondary phases.....	57
Figure 38. XRD patterns refined of a) NMC-111, b) NMC-622, c) NMC-226 and d) NMC-262.....	58
Figure 39. SEM images of a) NMC-111, b) NMC-622, c) NMC-226 and d) NMC-262 active materials. ....	60
Figure 40. a) BF and b) HR images of NMC-111 cathode. c) SAED pattern of NMC-111, d) which was successfully indexed to $R\bar{3}m$ . ....	60
Figure 41. a) BF and b) HR images of NMC-622 cathode. c) SAED pattern of NMC-111, d) which was successfully indexed to $R\bar{3}m$ . ....	61
Figure 42. a) BF and b) HR images of NMC-226 cathode. c) SAED pattern of NMC-111, d) which was successfully indexed to $R\bar{3}m$ . ....	61
Figure 43. XRD patterns of Mo-doped NMC-111, NMC-226, and NMC-622 heat-treated at 800 °C for 20h.....	62
Figure 44. XRD patterns of W-doped NMC-111, NMC-226, and NMC-622 heat-treated at 800 °C for 20h.....	63
Figure 45. XRD patterns of Ag-doped NMC-111, NMC-226, and NMC-622 heat-treated at 800 °C for 20h.....	63
Figure 46. XRD patterns of Cu-doped NMC-111, NMC-226, and NMC-622 heat-treated at 800 °C for 20h.....	64

Figure 47. SEM images of Mo-doped NMC-111, NMC-622, and NMC-226 cathode materials. ....	66
Figure 48. SEM images of W-doped NMC-111, NMC-622, and NMC-226 cathode materials. ....	66
Figure 49. SEM images of Ag-doped NMC-111, NMC-622, and NMC-226 cathode materials. ....	67
Figure 50. SEM images of Cu-doped NMC-111, NMC-622, and NMC-226 cathode materials. ....	67
Figure 51. a) BF and b) HR images of the Mo-doped NMC-111 cathode. c) Respective SAED pattern, d) which was successfully indexed to $R\bar{3}m$ .....	69
Figure 52. a) BF and b) HR images of the Mo-doped NMC-226 cathode. c) Respective SAED pattern, d) which was successfully indexed to $R\bar{3}m$ .....	70
Figure 53. a) BF and b) HR images of the Mo-doped NMC-622 cathode. c) Respective SAED pattern, d) which was successfully indexed to $R\bar{3}m$ .....	70
Figure 54. a) BF and b) HR images of the W-doped NMC-111 cathode. c) Respective SAED pattern, d) which was successfully indexed to $R\bar{3}m$ .....	71
Figure 55. a) BF and b) HR images of W-doped NMC-226cathode. c) Respective SAED pattern, d) which was successfully indexed to $R\bar{3}m$ .....	71
Figure 56. a) BF and b) HR images of the W-doped NMC-622 cathode. c) Respective SAED pattern, d) which was successfully indexed to $R\bar{3}m$ .....	72
Figure 57. a) BF and b) HR images of the Ag-doped NMC-111 cathode. c) Respective SAED pattern, d) which was successfully indexed to $R\bar{3}m$ .....	72
Figure 58. a) BF and b) HR images of the Ag-doped NMC-226 cathode. c) SAED pattern of NMC-111, d) which was successfully indexed to $R\bar{3}m$ .....	73
Figure 59. a) BF and b) HR images of the W-doped NMC-622 cathode. c) Respective SAED pattern, d) which was successfully indexed to $R\bar{3}m$ .....	73
Figure 60. a) BF and b) HR images of the Cu-doped NMC-111 cathode. c) Respective SAED pattern, d) which was successfully indexed to $R\bar{3}m$ .....	74

Figure 61. a) BF and b) HR images of the Cu-doped NMC-226 cathode. c) Respective SAED pattern, d) which was successfully indexed to $R\bar{3}m$ .....	74
Figure 62. a) BF and b) HR images of the Cu-doped NMC-622 cathode. c) Respective SAED pattern, d) which was successfully indexed to $R\bar{3}m$ .....	75
Figure 63. a) BF and b) HR images of Mo-doped NMC-622 cathode after cycling. c) Respective SAED pattern, d) which was successfully indexed to $R\bar{3}m$ . .....	75
Figure 64. Comparison of the transition metals content determined by EDS (black marks) and the values targeted (red marks) for NMC-111, NMC-622, NMC-226, and NMC-262. ....	76
Figure 65. XPS tight-scans of C1s, O1s, Li1s, Ni2p, Mn2p, Mn3s and Co2 for undoped 111, 622, and 226 NMC cathode materials. ....	78
Figure 66. C1s, O1s, and Li1s XPS profiles for doped NMC-111, NMC-622, and NMC-226 cathode materials. ....	81
Figure 67. XPS profile of doped 111, 622 and 226 NMC cathode materials for Ni2p, Mn2p, and Co2 peaks. ....	83
Figure 68. Representative Mn3s XPS profile, spectra of each related doped element of 111, 622 and 226 NMC cathode materials. ....	86
Figure 69. Comparison of the discharge capacity of NMC-111, NMC-622, NMC-226, and NMC-262. ....	87
Figure 70. Voltage profiles of undoped NMC cathode materials, a) charged at 0.1C and discharged at 0.1C, b) charged at 0.1C and discharged at 0.3C c) charged at 0.1C and discharged at 1C d) charged at 0.3C and discharged at 0.1C e) charged at 0.3C and discharged at 0.3C. ....	89
Figure 71. The discharge capacity of doped NMC cathode materials as a function of cycles. ....	91
Figure 72. Initial charge-discharge profile of NMC cathode materials from 2.7 V to 4.2 V at 0.1C. ....	93
Figure 73. Coulombic efficiency of doped NMC cathode materials. ....	94
Figure 74. EIS spectrum of Mo-doped NMC-111, NMC-622, and NMC-226 layered cathode materials. ....	95

Figure 75. EIS spectrum of W-doped NMC-111, NMC-622, and NMC-226 layered cathode materials.....	97
Figure 76. EIS spectrum of Ag-doped NMC-111 and NMC-622 layered cathode materials. ....	98
Figure 77. EIS spectrum of Cu-doped NMC-111 and NMC-622 layered cathode materials. ....	98

## LIST OF ABBREVIATIONS

LCO	Lithium Cobalt Oxide
LFP	Lithium Iron Phosphate
NMC	Lithium Nickel Manganese Cobalt Oxide
NCA	Lithium Nickel Cobalt Aluminum Oxide
LMO	Lithium Manganese Oxide ( $\text{LiMn}_2\text{O}_4$ )
LMP	Lithium Manganese Phosphate ( $\text{LiMnPO}_4$ )
LNO	Lithium Nickel Oxide ( $\text{LiNiO}_2$ )
SEI	Solid Electrolyte Interface
LNMO	Lithium Nickel Manganese Oxide ( $\text{LiNi}_{0.5}\text{Mn}_{0.5}\text{O}_2$ )
DCCA	Drying Control Chemical Additive
EIS	Electrochemical Impedance Spectroscopy
FSW	Finite Space Warburg
PVDF	Polyvinylidene difluoride
NMP	N-methyl pyrrolidinone
EC:DEC	Ethylene carbonate:diethylene carbonate
XRD	X-Ray Diffractometer
SEM	Scanning Electron Microscopy
HRTEM	High Resolution Transmission Electron Microscopy
BF	Bright Field
SAED	Selected Area Electron Diffraction
EDS	Energy Dispersive Spectroscopy
ICP-MS	Inductively Coupled Plasma-Mass Spectroscopy
XPS	X-ray Photoelectron Spectroscopy
DMF	N,N Dimethylformamide
CA	Citric Acid
CT	Charge Transfer

## CHAPTER 1

### INTRODUCTION

Lithium-ion batteries are key components for mobile applications as a power source. They offer higher gravimetric and volumetric energy density compared to other rechargeable batteries such as NiMH and NiCd [1]. Thus, Li-ion batteries can be considered as candidate power source for electric vehicles (EVs). They have also potential to be used in grid-energy storage applications. Thus, there is a requirement to improve the current Li-ion technology for present and potential applications. The most important innovation that can be brought to this technology is the development of high capacity electrodes, particularly cathode materials which can provide higher voltages.

The history of the development of new cathode materials has started with  $\text{Li}_x\text{MO}_2$  ( $M = \text{Co}, \text{Mn}, \text{and Ni}$ ) system by Goodenough in 1980 [2]. Later on,  $\text{LiFePO}_4$  was developed as more stable positive electrode materials for rechargeable Li-ion batteries in 1996 [3]. Yazami developed new intercalation anode material [4], graphite, and this achievement enabled the commercialization of Li-ion battery by Sony in 1991 [5]. Olivine structured  $\text{LiFePO}_4$  (LFP), layered  $\text{LiCoO}_2$  (LCO) and its variations such as  $\text{LiNi}_x\text{Mn}_y\text{Co}_{1-x-y}\text{O}_2$  (NMC) and  $\text{LiNi}_x\text{Co}_{1-x-y}\text{Al}_y\text{O}_2$  (NCA) became more favorable due to their higher energy density and better cycle life.

$\text{LiCoO}_2$  has been used as a cathode for Li-ion batteries for many years. The stability of LCO in ambient atmosphere and its easy production at large scale are the main advantages of this particular cathode material. However, the capacity of layered LCO used in commercial products is limited to perform 50% of its theoretical capacity.

LCO could only perform a capacity about  $140 \text{ mAhg}^{-1}$ , while its theoretical capacity is  $274 \text{ mAhg}^{-1}$  [6]. Besides, the cost and the potential toxicity of Co, which is one of the main component of LCO, bring other drawbacks. In this regard, LFP-based cathode materials have taken attention due to its low cost and environmental impact. LFP-based cathode materials also exhibit relatively higher thermal stability and power capability. However, they have relatively lower average potential and lower ionic and electrical conductivity with a limited practical capacity up to  $160 \text{ mAhg}^{-1}$  [7]. Another important issue for LFP-based cathode materials is the presence of one-dimensional channel diffusion path for lithium ions. These channels can be easily blocked which hinders the lithium ion diffusion because of the impurities and the defects in the structure. There are several studies to improve such drawbacks [7–11]. These mainly focus on reducing the particle size, cationic doping and coating the surface with carbon to increase the conductivity and higher rate performance [12].

$\text{Li}_{1-x}\text{MO}_2$  (M=Ni, Mn, and Co) compounds have been developed offering good lithium ion conduction with two-dimensional channels. In this system, Mn also provides the least toxicity at a lower cost. This makes NMC as a favorable cathode material with the reduced Co content with a very good combination of energy, power, cycle life and thermal stability. Thus, NMC has found a widespread use in the industry [1,13]. However, some problems such as irreversible capacity loss at first charge-discharge cycle and the low rate capability should be improved so as to meet the requirements of EVs applications [14,15].

In the present study, two approaches to improve charge/discharge performance at high rates were dealt. First one relies on the effect of Ni:Mn:Co ratio, thus different NMC compositions, namely  $\text{Li}(\text{Ni}_{1/3}\text{Mn}_{1/3}\text{Co}_{1/3})\text{O}_2$  (NMC-111),  $\text{Li}(\text{Ni}_{0.2}\text{Mn}_{0.2}\text{Co}_{0.6})\text{O}_2$  (NMC-226),  $\text{Li}(\text{Ni}_{0.6}\text{Mn}_{0.2}\text{Co}_{0.2})\text{O}_2$  (NMC-622) and  $\text{Li}(\text{Ni}_{0.2}\text{Mn}_{0.6}\text{Co}_{0.2})\text{O}_2$  (NMC-262) were investigated for the search of a good combination in high discharge capacities with rate capability, Figure 1. In the second approach the effect of doping elements such as Mo, W, Cu and Ag in NMC cathode

materials with various Ni:Mn:Co content was investigated. In the present study, spray pyrolysis method was used to attain spherical aggregates having fine-sized particles in powder of active materials. The effect of morphology, and the specific surface area of particles were also investigated.

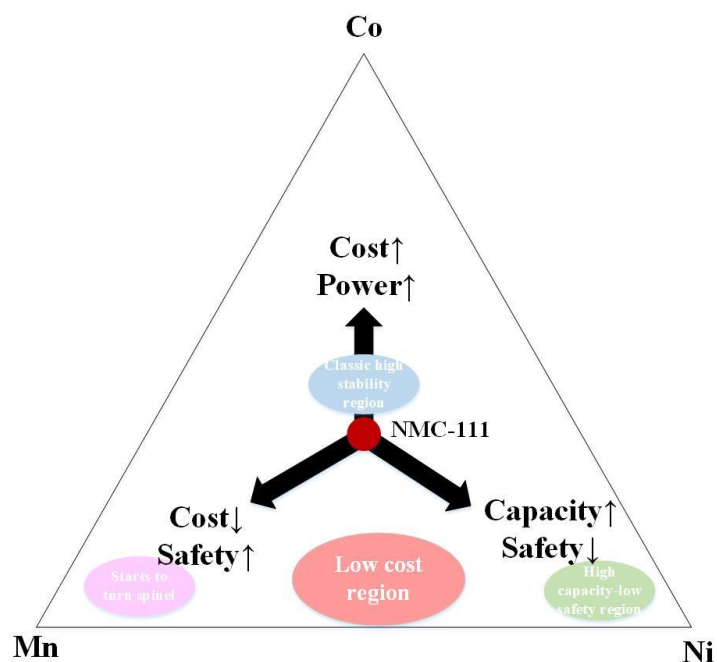


**Figure 1.** Safety, capacity and cost change with varieties of the composition.

This thesis was organized as follows. Chapter 2 focuses on the properties of commonly used cathode materials including NMC. It is followed by the experimental procedure including the synthesis and characterization of NMC. The results and discussion are given in Chapter 4 and it is followed by the conclusion of the study in Chapter 5.



## CHAPTER 2

### LITERATURE SURVEY

#### 2.1 Cathode Materials

Li-ion batteries could not be used commercially until the early 1970's despite the first attempt was made by Lewis in 1912 [16].  $\text{TiS}_2$  was offered as an intercalated cathode material by Whittingham in 1976 [17], where Li metal was the anode. Although  $\text{TiS}_2$  worked well as a cathode material in the proposed system, the main problem raised from the anode i.e. the dendrite formation during cycling, Figure 2. Thereafter, the lithium intercalation in graphite was discovered by Yazami *et al.* in 1986 [18], Figure 3, and graphite was offered as a promising anode for Li-ion batteries due to its ordered structure with a high capacity and relatively lower voltage profile.

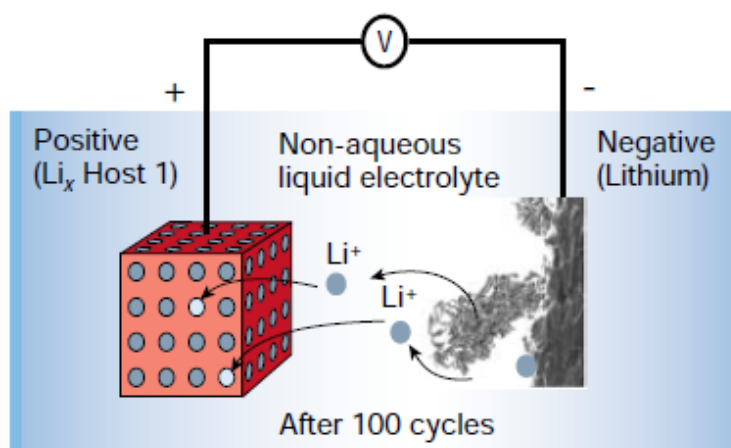


**Figure 2.** The dendrite formation on lithium anode [19].

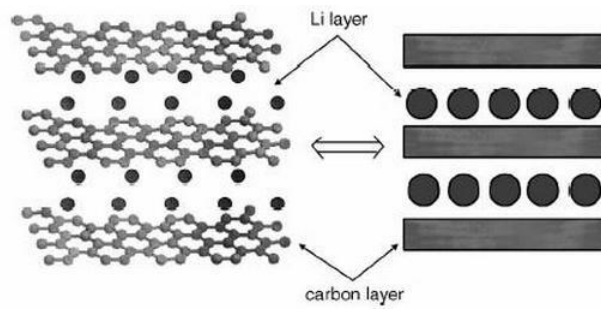


**Figure 3.** Schematic diagram showing the intercalation of lithium in graphite.

The intercalation is a process where metal ions are reversibly removed or inserted into a host material without a significant structural change [18,20] These reactions take place with the movement of lithium ions back and forth between the cathode and the anode. Thus, Li-ion batteries are known as “Rocking-chair” batteries.

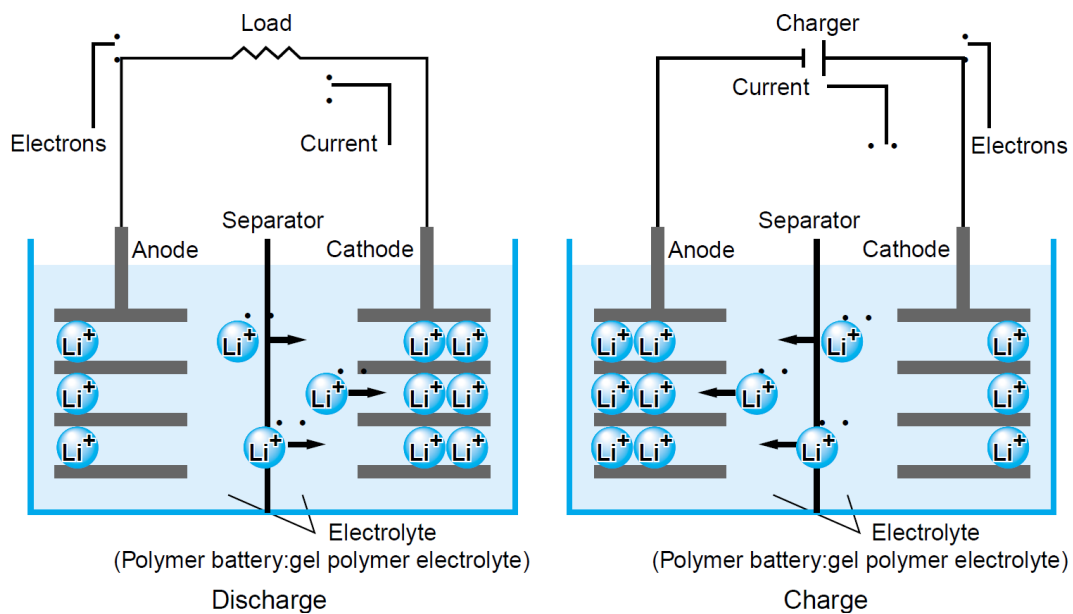
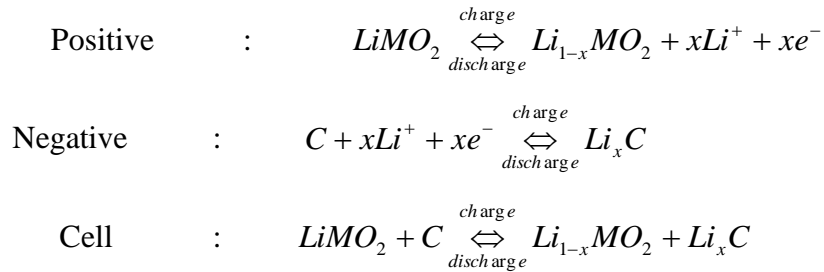


**Figure 4.** Diagram of Li-ion cell during charging and discharging [21].

In a typical cell, there are four type components; a positive electrode, a negative electrode, electrolyte and the separator. Here, the electrolyte provides a path for ion migration between electrodes, while the separator prevents the physical contact

between anode and cathode, Figure 4. The electrode and cell reactions in an intercalation type lithium-ion battery are as follows.



These reactions take place reversibly depending on whether the cell is charging or discharging. During charging, lithium ions are extracted from the cathode and inserted into the anode while the reverse case is valid in discharging. There are other mechanisms for lithium in Li-ion batteries which are given together with intercalation reaction in Figure 5 [22].

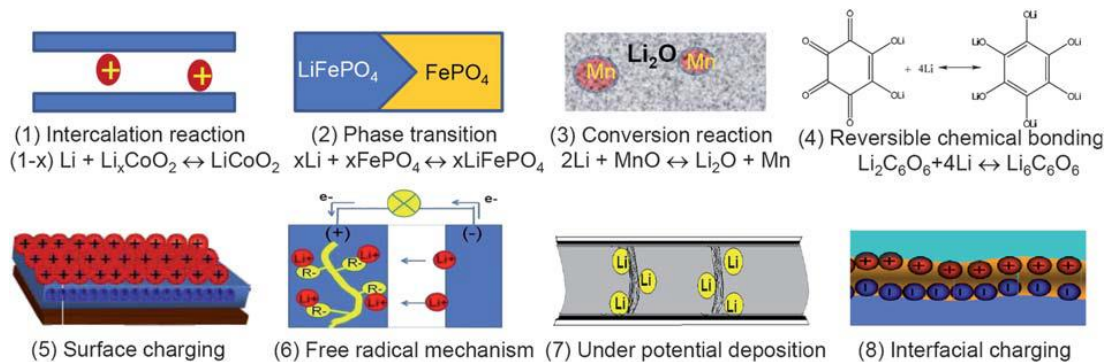


**Figure 5.** Reversible lithium storage mechanisms in Li-ion batteries [23].

The crystal structure of cathode materials used in Li-ion batteries can be classified into three categories, Figure 6. These are;

- Layered ( $\alpha\text{-NaFeO}_2$ ) structure
- Spinel structure
- Olivine structure

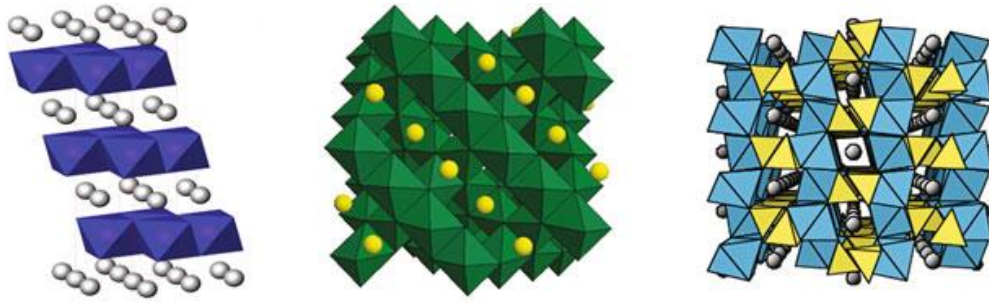


**Figure 6.** Structure of common cathode materials in Li-ion batteries; a) layered ( $\alpha$ -NaFeO<sub>2</sub>) structure, b) spinel structure and c) olivine structure

The common cathode materials, which have layered ( $\alpha$ -NaFeO<sub>2</sub>) structure, are LiCoO<sub>2</sub> (LCO), LiNiO<sub>2</sub> (LNO), Li(Ni<sub>1/3</sub>Mn<sub>1/3</sub>Co<sub>1/3</sub>)O<sub>2</sub> (NMC) and Li(Ni<sub>0.8</sub>Co<sub>0.15</sub>Al<sub>0.05</sub>)O<sub>2</sub> (NCA). LiMn<sub>2</sub>O<sub>4</sub> (LMO) is a typical example of the spinel structure, while LiFePO<sub>4</sub> (LFP) and LiMnPO<sub>4</sub> (LMP) are for the olivine structure.

The intercalation structures could also be divided into three major groups according to the intercalation pathways; 1-D, 2-D, and 3-D structures, Figure 7. The intercalation reaction does not chemically affect the host structure independent from the type of the diffusion path. However, host structure might be a subject of a tremendous expansion and shrinkage through perpendicular pathways during intercalation and deintercalation of lithium ions.

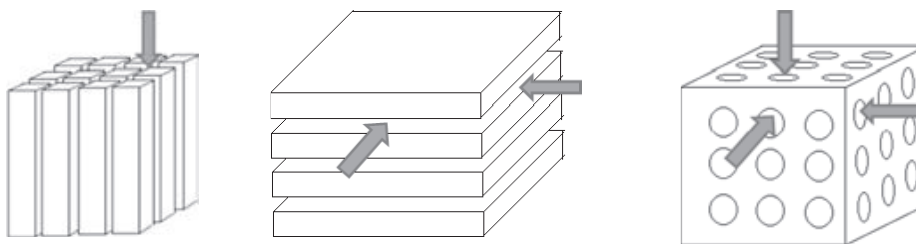


**Figure 7.** Schematics of the lithium intercalation pathways in a) 1-D, b) 2-D, and c) 3-D structures.

The oxides are challenging in terms of their structural stability particularly at the fully delithiated state due to their weak van der Waal's forces between the oxide layers

[24]. The diffusion pathways also vary depending on the structure, thus the reaction mechanisms and the lattice stability might differ for each structure. The 2-D layered materials are more attractive as compared to 1-D and 3-D counterparts due to its capability for lithium ion diffusion and higher selectivity for the intercalating species. The common examples for the layered cathode materials in Li-ion batteries are graphite and layered oxides such as LCO, NMC, and NCA. The cathode materials having layered structures are discussed in a greater detail in the following section.

### **2.1.1 Layered ( $\alpha$ -NaFeO<sub>2</sub>) Structure**

The first commercial product in layered structured cathode materials is LCO which has been introduced by Sony. LCO has a crystal structure, where Co and Li elements located in octahedral sites occupying alternating layers along the 111 planes in a cubic closed-packed (ccp) oxygen array to form a hexagonal structure (which is called O3 stacking arrangement) [24].

LCO is an attractive cathode material due to its theoretical capacity of  $\sim 280 \text{ mAhg}^{-1}$ . However, the instability and the high volume change in the structure result in capacity fading when LCO was cycled up to 4.2V [25]. Thus, it is not possible to obtain its theoretical capacity and it typically performs a capacity up to  $\sim 140 \text{ mAhg}^{-1}$  in the range of 3.0-4.2V. Moreover, LCO degrades when it is overcharged which results in failure of the battery. This also causes safety problems in the battery. Therefore, the efforts are concentrated on finding alternative cathode materials to obtain better stability at a lower cost.

LNO is another layered cathode material which was promoted by Dyer in 1954 [26]. It has been studied as an alternative cathode for the replacement of LCO. It eliminates Co content and thus it potentially reduces the cost and the toxicity. Moreover, it also provides higher energy density as compared to LCO. However, it brings some challenges caused by structural instability. During synthesis, it has a tendency to loss

of Li and reduction of some Ni to the +2 oxidation state. These result in lithium deficient compounds and cause cation disorder between Li and Ni. Moreover, it undergoes serious phase transformations during cycling, which might lead decreasing in rate capability.  $\text{Ni}^{3+}$  in the structure can fully oxidized to  $\text{Ni}^{4+}$  at high temperatures and this causes severe problems such as chemical instability and thermal runaway [1,27,28].  $\text{Ni}^{4+}$  can react with organic electrolytes used in the lithium-ion battery [29]. This results in the formation of thick solid electrolyte interface (SEI) at the surface of the anode. It increases the impedance of the battery and consumes active Li. This leads to non-stoichiometry in LNO and effects the electrochemical performance [30,31]. For this reasons, the studies have focused on the partial substitution of Co with Ni rather than completely replacing Co [32]. The cationic disorder could be reduced and better structural stability was observed with partial substitution of Co as in the case of  $\text{LiNi}_{0.8}\text{Co}_{0.2}\text{O}_2$  [33]. Co also helps to control further oxidation in the structure and thus improve structural stability and the safety [34,35].

Several elements were studied as a partial substitution for Co so as to improve the electrochemical properties in LNO and LCNO. Among them, particularly Al alloyed compounds such as  $\text{LiNi}_{0.8}\text{Co}_{0.15}\text{Al}_{0.05}\text{O}_2$  (NCA) has gained importance in commercial applications, [36]. NCA is an attractive cathode material since it has a high capacity of  $\sim 200\text{mAhg}^{-1}$  up to 4.2V vs  $\text{Li}^+/\text{Li}$  and it is resistant to side reactions with electrolytes. However, although Co amount is reduced in this particular compounds, it has still a high amount of Ni and Co that increase the cost of the product. The last but not the least, SEI growth and micro-crack formation at grain boundaries cause severe capacity fade at elevated temperatures ranging from 40 to 70°C [34,37].

$\text{LiMnO}_2$  (LMO) is another cathode material for Li-ion batteries and it is a promising candidate due to its lower cost and less toxicity. This cathode material was developed aiming to improve deficiencies in the structure such as poor crystallinity and the

structure stability during cycling [38]. However, the cycling performance of LMO is not sufficient because of the phase transformation from layered to spinel structure. During cycling,  $\text{Mn}^{3+}$  in the structure has a tendency to change into  $\text{Mn}^{2+}$  and  $\text{Mn}^{4+}$ , where the  $\text{Mn}^{2+}$  ions subsequently migrate into vacant sites in the lithium layers via low-energy pathways. This often results in the phase transformation from layered to spinel easier [36,39–42].

Similarly, layered Li-Ni-Mn-O (LNMO) compounds have been studied as a cathode for Li-ion batteries. In LNMO, Ni and Mn exist as +2 and +4 oxidation states, respectively.  $\text{Ni}^{2+}$  is the electrochemically active species and provides high-rate pathways which are crucial to obtain higher capacities. On the other hand,  $\text{Mn}^{4+}$  is electrochemically inert and thus preserve more stable structure [43].  $\text{LiNi}_{0.5}\text{Mn}_{0.5}\text{O}_2$  with a capacity of  $170 \text{ mAhg}^{-1}$  was firstly reported by Spahr in 1998 [44]. Ohzuku and Lu also studied the same compound and they reported better electrochemical performances [45,46].

Addition of Co in LNMO compounds was found as an effective way to enhance the structural stability by blocking Ni atoms from entering Li layers [47].  $\text{LiNi}_{1-y-z}\text{Mn}_y\text{Co}_z\text{O}_2$  (NMC) was first proposed by Liu *et al.*, in 1999 [48] and the common compound of NMC is  $\text{LiNi}_{1/3}\text{Mn}_{1/3}\text{Co}_{1/3}\text{O}_2$  which has high capacity and ability to operate at high voltages. [49]. In this structure, Ni element has high specific energy but low stability, while Mn provides low internal resistance but offers low capacity in NMC. This particular compound brings better electrochemical properties compared to other cathode materials. NMC shows a reversible discharge capacity about  $200 \text{ mAhg}^{-1}$  in the range of 2.5-4.6 V. Higher capacities can also be achieved when the cells are charged to the higher voltage limits even this usually lowers the capacity retention [24]. The increasing amount of Ni in NMC also provides higher capacity as high as  $230 \text{ mAhg}^{-1}$  [50]. Therefore,  $\text{LiNi}_{0.4}\text{Mn}_{0.3}\text{Co}_{0.3}\text{O}_2$  (NMC-433) and  $\text{LiNi}_{0.6}\text{Mn}_{0.23}\text{Co}_{0.2}\text{O}_2$  (NMC-622) have been the subject of considerable attention [1].

However, rapid capacity loss during first cycling is the major drawback of NMC and thus the studies are concentrating on improvement of this problem [51].

### 2.1.2 Spinel Structure

One of the common examples for cathode materials which have spinel structure is  $\text{LiMn}_2\text{O}_4$  (LMO). LMO and its variants are low-cost, high rate performance, high operating voltage, and moderate safety with no resource limitations. LMO cathode materials offer the capacity in the range of 100-120  $\text{mAhg}^{-1}$  up to 4.1V vs  $\text{Li}^+/\text{Li}$ . However, this compound is unstable and tends to self-discharge at elevated temperatures causing lower capacity [52,53]. Moreover, the solubility of Mn in the electrolyte is another problem affecting the cycle life. Therefore, surface treatments and cation substitution have been employed to address these problems [54]. There are also Li-rich variations such as  $\text{Li}_{1.12}\text{Mn}_{1.88}\text{O}_4$  having ordered mesoporous structure which exhibits better electrochemical performance as compared to dense spinel structure [55].

### 2.1.3 Olivine Structure

$\text{LiFePO}_4$  (LFP) was first announced olivine structured cathode material for rechargeable Li-ion batteries. LFP has a theoretical capacity of  $\sim 170 \text{mAhg}^{-1}$  and it operates at a very flat voltage regime which is about 3.4 V vs  $\text{Li}^+/\text{Li}$  [7]. LFP has an orthorhombic structure with *Pnma* space group, where  $\text{Li}^+$  and  $\text{Fe}^{2+}$  occupy octahedral sites, while P is located in tetrahedral sites in a slightly distorted hexagonal close-packed (hcp) oxygen array. Low average potential and insufficient electrical and ionic conductivity causing a decrease in rate performance are the major drawbacks of the LFP compounds [56]. Reduction in particle size in combination with carbon coating [57] and cation doping [12] are the effective approaches so as to increase its rate performance.

LFP variants such as  $\text{LiMnPO}_4$  and  $\text{LiCoPO}_4$  provide high rate performance, better resistance to side reactions with electrolyte and better safety. However, they exhibit low capacity with a limited voltage range [24].

The comparison of the cathode materials discussed above are shown in Figure 8 and their general properties are summarized in Table 1.

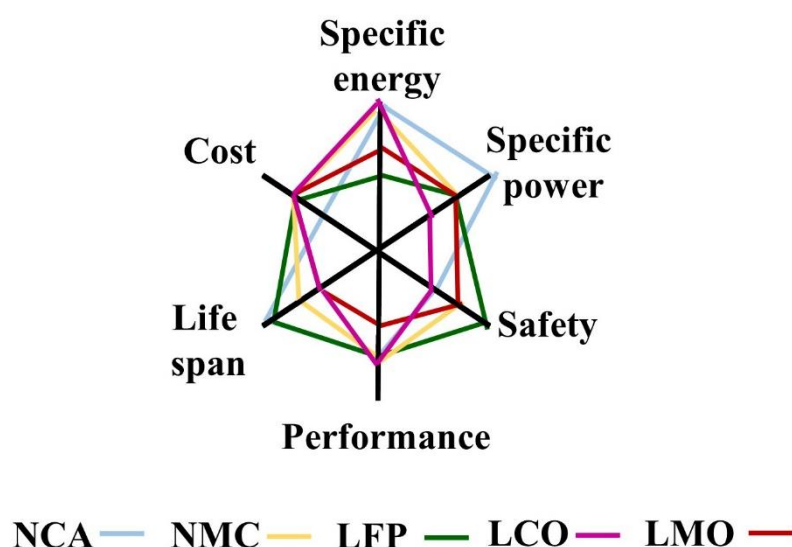


**Figure 8.** General comparison of commonly used cathode materials (adapted from website of Battery University [58]).

**Table 1.** Properties of cathode materials in commercial lithium-ion batteries.

Cathode Materials	LCO	LMO	NMC	LFP	NCA
Reversible capacity (mAh/g)	150-200	100-150	150-220	90-120	200-260
Charge termination plateau (V)	4.20	4.20	4.3	3.65	4.2
Cycle Life (cycles)	500-1000	300-700	1000-2000	1000-2000	500
Thermal runaway (°C)	150	250	210	270	150
Specific energy (Wh/kg)	546	410-492	610-650	518-587	680-760

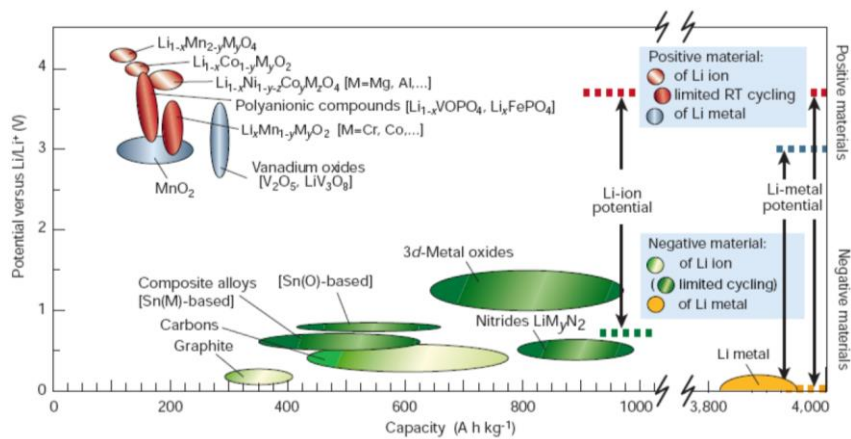


**Figure 9.** Voltage versus capacity for cathode and anode materials [59].

For many years, Li-ion batteries have been studied and several potential cathode materials and anodes were developed, seen in Figure 10. Although there is some adaptation to commercial products, there are still limiting factors to choose cathode and anode. In this respect, the choice of the cathode and anode materials is very critical since there are several side reactions between the electrodes and the electrolyte. The side reactions can be in the form of SEI formation at the anode surface, Figure 9, and dissolution/aging of the cathode materials. The side reactions on the cathode materials are given in Figure 10. Thus, these reactions also have to be taken into account in the battery design.

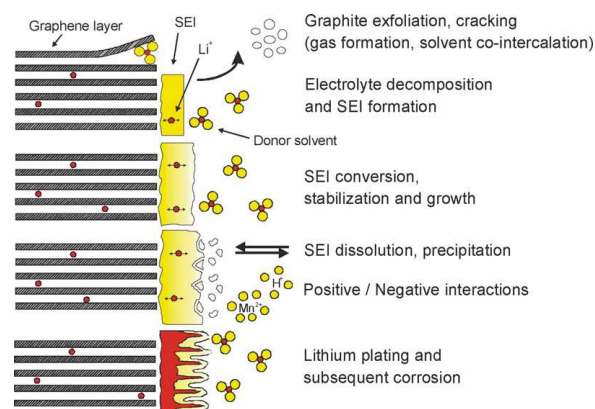


**Figure 10.** Changes at the anode/electrolyte interface [39].

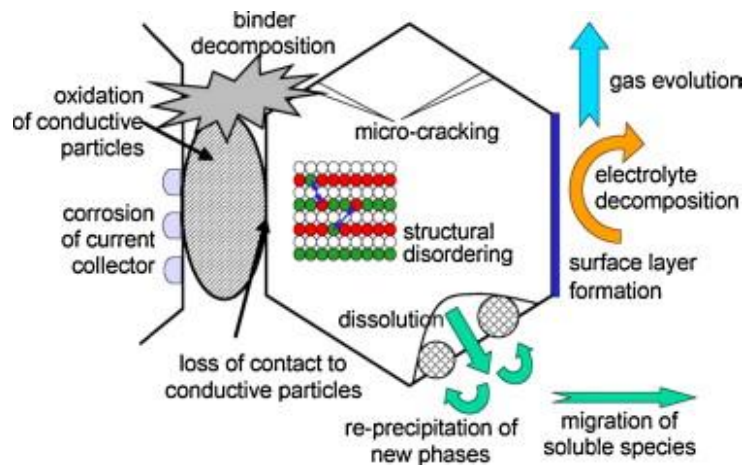


**Figure 11.** Degradation mechanisms of composite cathode materials [60].

## 2.2 Lithium Nickel Manganese Cobalt Oxide

NMC compounds are very attractive due to their optimum electrochemical performance. They also provide a diversity in terms of their metal content which results in different properties such as discharge capacity, rate capability and safety. In NMC, it is important to attain a stable structure operating at high voltages with high capacity. Thus, the studies are concentrated on eliminating the drawbacks of NMC as discussed in the previous section so as to use it in commercial applications.

For the structural stability, oxidation states of the transition metals in NMC both after the production and during cycling are critical. In principle, the oxidation states of transition metals in NMC are;  $\text{Ni}^{2+}$ ,  $\text{Mn}^{4+}$ , and  $\text{Co}^{3+}$ . Here,  $\text{Mn}^{4+}$  is electrochemically inactive and it plays a role in transferring the electric charge over Ni cations. Change in the oxidation states of Mn causes irreversible reactions in the structure [61]. The oxidation state of Co is also important because dissolution of  $\text{Co}^{4+}$  in the liquid electrolyte causes the structural instability leading the capacity fade [62,63].

$\text{Ni}^{2+}$  has a similar ionic radius, 0.69 Å, with  $\text{Li}^+$ , i.e. 0.76 Å. This might cause cation mixing between Ni and Li ions in the structure [64]. This cation mixing reduces

lithium ion diffusion which results in inferior electrochemical properties such as loss of capacity. Synthesis methods are also important for the electrochemical performance of NMC since they also affect the oxidation states of transition metals in the structure [65–67].

Determination of cation mixing and the hexagonal ordering in the structure is important since it directly affects the electrochemical properties. There are various methods proposed to estimate the lattice ordering in layered oxides. One way is the determination of intensity ratio of (003) and (104) peaks, ( $I_{[003]}/I_{[104]}$ ) [64]. Here,  $I_{[003]}/I_{[104]}$  ratio larger than 1.2 indicates that there is negligible or no cation mixing in the structure, while the ratio lower than 1.2 indicates a considerable extent of cation mixing. Additionally, splitting of both (006)/(102) and (108)/(110) diffraction peaks are signs of good hexagonal ordering of the layered structure, Figure 12.

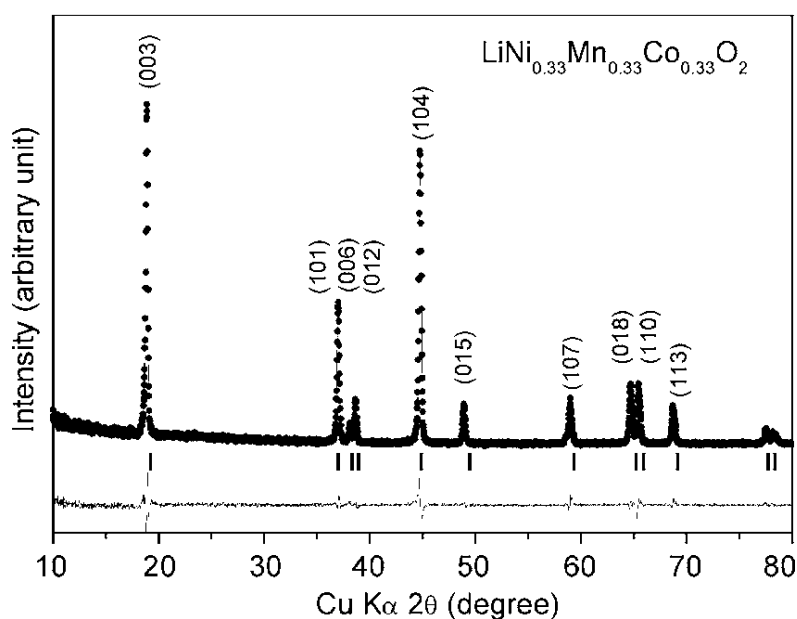


**Figure 12.** Rietveld refinement data of  $\text{LiNi}_{1/3}\text{Mn}_{1/3}\text{Co}_{1/3}\text{O}_2$  [68].

Another way to estimate the structural ordering is proposed by Arof in 2008 for layered oxides. In this method, the degree of lattice disorder,  $R$ , can be calculated by;

$$R = I_{(102)} + I_{(106)} / I_{(101)} \quad (1)$$

This also allows the determination of lattice ordering,  $y$ , with the equation as given follows;

$$y = 1.073 - 0.228R + 0.039R^2 \quad (2)$$

Of the methods discussed above, the  $I_{[003]}/I_{[104]}$  ratio is more common and adopted approach so as to determine the ordering of the structure in layered oxides [68]. There are also other parameters that have an important role in the performance of the battery besides cation mixing. These are the phase purity, degree of crystallinity, particle morphology and size affecting the surface area. Thus, synthesis method has a potentially great effect on these parameters [69].

The variations in Li content and transition metals in NMC also result in different electrochemical performance. In this regard, Choi *et al.*, [70] studied  $\text{Li}_{1-x}(\text{Ni}_{1/3}\text{Mn}_{1/3}\text{Co}_{1/3})\text{O}_2$  cathode material as a function of Li content. They reported that Li content should be at least 0.65 for chemical stability, while 0.77 was determined as a critical limit for the structural stability.  $\text{Li}_{1-x}(\text{Ni}_{1/3}\text{Mn}_{1/3}\text{Co}_{1/3})\text{O}_2$  performed a capacity as high as  $180 \text{ mAhg}^{-1}$ , however, they determined the considerable cation mixing in the structure which might cause a capacity loss. Mohanty *et al.*, [71] investigated the structural stability of both Li-rich and Mn-rich compound,  $\text{Li}_{1.2}(\text{Ni}_{0.15}\text{Mn}_{0.55}\text{Co}_{0.1})\text{O}_2$ , up to 4.8 V cut-off voltage. They reported that  $c$  lattice parameter decreased when charged over 4.4 V, while it started to increase during discharging down to 3.5 V. They stated that this  $c$  lattice parameter was an indicator for Li extraction from transition metal layers. This caused transformation from layered to spinel structure transformation. Similarly, Pimenta *et al.*, [72] studied Li-rich NMC cathode and investigated the effects of morphology, particle size, and composition on the electrochemical performance. Of the compositions,

$\text{Li}_{1.2}(\text{Ni}_{0.13}\text{Mn}_{0.54}\text{Co}_{0.13})\text{O}_2$  exhibited the highest first discharge capacity with  $269 \text{ mAhg}^{-1}$  and a retention of 89.6% after 100 cycles.

Mn content is another factor that can affect the electrochemical properties. Of the studies concentrated Mn content, Liu *et al.*, [73] showed that increasing amount of Mn in  $\text{Li}(\text{Ni}_{0.9-y}\text{Mn}_y\text{Co}_{0.1})\text{O}_2$  caused faster capacity loss and poorer rate capability. More importantly, they observed a layered-to-spinel transition in structure when Mn content was higher than 0.5. In a recent study, Zheng *et al.*, [74] studied that the role of Mn content in Ni-rich NMC cathode materials. They observed an improvement in the cycling stability with the increase in Mn content and decrease in Ni content.

Another alternative method to alter the properties of NMC is changing the Ni content. Of these, Ni-rich NMC cathode materials are the most promising candidates since Ni provides higher capacity when the battery is charged to the higher voltages [75]. Liu *et al.*, studied the effect of Ni content on the capacity and thermal stability of NMC. Although Ni-rich compositions exhibited higher capacity, the high Ni content resulted in lower structural and thermal stability because of its tendency of reacting with electrolyte [76,77]. This lower structural and thermal stability was stated as one of the major drawbacks of Ni-rich compounds. Thus, high Ni content increases a risk factor for safety issues [78,79]. Similarly, Liu *et al.*, [76] investigated the effect of Ni on the cycle life of NMC. For this purpose, they produced cathode materials with different Ni:Mn:Co mole ratio as 523 and 433. NMC-433 offered improved cycle performance with a higher rate performance and lower impedance. Thus, a more stable structure in NMC was attributed to the lower amount of Ni.

The content of Co similarly affect the structural stability of NMC and thus electrochemical performance. Ngala *et al.*, [80] studied the effect of Co in NMC and synthesized  $\text{Li}(\text{Ni}_{0.4}\text{Mn}_{0.4}\text{Co}_{0.2})\text{O}_2$  which exhibited good rate capability. They also reported a reversible capacity ranging from 180 to  $155 \text{ mAhg}^{-1}$  at current densities from 0.1 to  $2.0 \text{ mAcm}^{-2}$ . The role of Co was emphasized on the stabilization of

layered structure and suppressing the migration of transition metal ions into the interlayer Li sites. Similarly, Yoshio et al., [47] reported that Co suppressed the cation mixing, however, they could not observe any change in the discharge capacity.

Morphology, porosity, particle size and thus the specific surface area of the active materials also affect the electrochemical properties of NMC. In this respect, the synthesis methods yielding different powder characteristics have an impact on the performance of the cathode materials. For instance, NMC synthesized by spray pyrolysis differs on surface resistance as compared to synthesized with coprecipitation [81]. The synthesis methods also yield different particle morphology and density in the cathode materials. There are some studies indicating that highly dense cathode materials exhibited better performance [82]. On the other hand, there are contradictory studies stating the importance of obtaining loose aggregates in the cathode material so as to increase the overall electrochemical performances [83–85].

Surface modification is another approach to prevent side reactions with electrolyte and attain a structural stability. Thus, studies are concentrated on the coating of NMC cathode surfaces. For this purpose, a coating of a protective layer such as  $\text{Al}_2\text{O}_3$ ,  $\text{LiCoO}_2$ , and carbon is very common. Son *et al.*, [86] examined the effect of  $\text{LiCoO}_2$  coating on NMC which improved the electrical contact within the cathode active particles. They reported that the coating minimized the interfacial impedance. However,  $\text{LiCoO}_2$  could not improve the capacity fading in NMC cathode. Kim *et al.*, [87] studied the effect of carbon coating focusing on the rate capability and the thermal stability. They also investigated the effect of carbon content and suggested that 1 wt.% carbon coating was sufficient to enhance rate capability and the thermal stability. In another study focused on  $\text{Al}_2\text{O}_3$ -coated NMC, Kim *et al.*, [88] reported an improved electrochemical performance as compared to the bare NMC. In this study,  $\text{Al}_2\text{O}_3$  was offered an effective coating layer for NMC cathode materials.

Doping of NMC is another way of affecting the electrochemical properties so as to improve the structural stability. Since doping might avoid the cation mixing and the phase transformation during cycling, it is a very common approach. In this respect, Na *et al.*, [89] successfully produced Si-doped NMC cathode materials without any impurity. The cathode materials exhibited enhanced cycle life and rate capability. In a similar work by Wei *et al.*, [90] reported that Si doping had an influence on Li-gap which was attributed to improved diffusion kinetics and the rate performance. Doeff *et al.*, [99] studied Ti doping in NMC and reported 15% higher discharge capacity. Additionally, they observed a decrease in volume change during insertion and extraction of lithium ions providing better capacity retention. Wilcox *et al.*, [91] examined the effects of Ti, Al, and Fe for the replacement of Co in NMC. Ti doping resulted in a relatively higher capacity and higher rate capability, while Fe doping resulted in lower capacity and rate capability. Al-doped NMC could not be synthesized without impurity phases and thus, they exhibited lower capacity despite it improved the capacity retention. Contrarily, Li *et al.*, [92] and Wang *et al.*, [93] showed that Al doping of improved the cyclability of NMC. They also reported a reduction in the formation of SEI layer and better structural stability due to the stable oxidation states of transition metals. Li *et al.*, [94] studied Y-doped NMC and obtained high discharge capacity and a better structural stability with a very low mole ratio of Y, i.e. 0.06. They stated that  $Y^{+3}$  was responsible for the stabilized structure. Doping of Zn was studied by Li *et al.*, [95] and Wei *et al.*, [96] and they found that Zn-doped NMC exhibited faster Li-ion diffusion with a lower impedance. The initial discharge capacity in Zn-doped NMC was measured as  $142 \text{ mAhg}^{-1}$  with only 0.20% capacity loss after 100 cycles. Zhang *et al.*, [97] studied doping of Mg, Cr, and Al for the replacement of Co so as to improve the cycling performance of NMC, especially at high voltage. Undoped NMC showed capacity retention of 86.6% after 50 cycles, while Cr-doped NMC showed negligible capacity fade with a capacity retention higher than 97% after 50 cycles. Mg and Al-doped NMC could only exhibit a capacity retention of 82.1% and 76.4%, respectively. This was attributed to prevention of dissolution of Co in the electrolyte especially at higher voltages with

Cr doping. Buyukburc *et al.*, [98] observed similar findings with Mo doping on retarding the dissolution of Co during cycling. Schipper *et al.*, [99] investigated the effect of Zr doping in Ni-rich NMC which exhibited faster kinetics in the potential range of 3.7–4.3V. This improvement was attributed to the prevention of layered-to-spinel structural transformation by Zr doping. Ates *et al.*, [100] examined the Na-doped Li-rich NMC which performed improved electrical conductivity with a better efficiency. Na doping also hindered the layered-to-spinel transformation and cation mixing in NMC.

Consequently, doping of layered cathode materials is an effective approach so as to improve electrode performance and their structural stability [101,102] where the synthesis methods provide different powder characteristics affecting on the performance of the cathode materials. The synthesis methods are discussed in a greater detail in the following section.

### **2.3 Synthesis Methods for NMC Cathode materials**

The electrochemical performance of the cathode materials in Li-ion batteries are strongly affected by the powder characteristics such as particle morphology, the active surface area, and the crystallinity [103]. Thus, the synthesis method plays a critical role so as to control the powder properties.

There are a variety of methods to produce NMC powders and particularly, solution-based methods such as co-precipitation [104], sol-gel [105,106], solid-state synthesis [95,107–109], spray drying [110,111], and microwave synthesis [112,113] have taken a considerable attention. Additionally, spray pyrolysis method is also attractive due to its better control on the particle size and morphology [114].

Of these, one of the easy way to produce NMC powder is the co-precipitation method. It is quite attractive since it also provides a control on particle shape and the

size without complex parameters. Luo *et al.*, [104] synthesized spherical and well-ordered layered NMC cathode materials via this method. NMC cathode materials in this study exhibited a good capacity of  $166 \text{ mAhg}^{-1}$  with 7% capacity loss after 30 cycles. Similar findings were reported by Wang *et al.*, [83] who produced Li-rich NMC cathode materials exhibited  $264.6 \text{ mAhg}^{-1}$  capacity with ~90% capacity retention after 50 cycles. On the other hand, Zhang *et al.*, [115] produced NMC cathode materials with a smaller particle size,  $<40\text{nm}$ , by the same technique and cathode materials, performed the first discharge capacity of  $160 \text{ mAhg}^{-1}$ . However, the capacity retention was only ~60% after 10 cycles. They stated that the side reactions with electrolyte and structural instability were responsible for the capacity loss and suggested coating a protective layer such as carbon.

Sol-gel is another synthesis method to produce NMC powders, particularly aiming for layered structures. In this regard, Lin *et al.*, [105] studied Al-doped NMC and synthesized  $\text{LiNi}_{1/3}\text{Mn}_{0.23}\text{Co}_{1/3}\text{Al}_{0.1}\text{O}_2$  layered cathode via sol-gel method. The cathode materials performed an initial discharge capacity of  $194.6 \text{ mAhg}^{-1}$ . Ding *et al.*, successfully synthesized La, Cr and Pr doped NMC cathode materials without any impurity via sol-gel method. They measured the initial capacity up to  $164 \text{ mAhg}^{-1}$  using La, Cr, and Pr as dopants. The rise in charge-transfer resistance during cycling could be suppressed with the dopants [116].

Solid-state synthesis is another method for powder synthesis of active materials. Bin *et al.*, [95] produced Zn-doped NMC cathode materials with this method, where the precursor was already prepared by co-precipitation method. They observed an enhancement in the thermal stability of NMC especially at higher temperatures up to  $55^\circ\text{C}$ , where the discharge capacities were measured as  $141\text{-}189 \text{ mAhg}^{-1}$ . Tan *et al.*, [107] synthesized NMC via the solid-state method using  $\alpha\text{-MnO}_2$  nanorods as a precursor. They could produce the powders with a particle size ranging from 150 to 200 nm. They measured the initial discharge capacities up to  $141.3 \text{ mAhg}^{-1}$ . Although there are some studies using solid-state reactions, this synthesis method is

not favorable as other methods, discussed above, especially for layered cathode materials. This is because of the possibility of impurities in this technique which might result in inferior electrochemical properties [108]. Additionally, precursors used in this synthesis method have relatively higher cost [109].

Spray drying is an alternative synthesis method which recently has been taken attention. Liu *et al.*, [110] synthesized NMC cathode materials with aspherical morphology via spray drying. However, the phase purity was not sufficient, where the  $\text{Li}_2\text{CO}_3$  formation was observed upon drying. In a similar study, Lin *et al.*, [111], studied Zr-doped NMC synthesized via spray drying with the same morphology. They measured  $160.2 \text{ mAhg}^{-1}$  as the first discharge capacity with a capacity retention of 92.4%.

Microwave synthesis can be also used for the NMC synthesis. Microwave irradiation generally results in a rapid heating, thus the production time is often very short [117]. Lee *et al.*, [65] synthesized  $\text{LiNi}_{0.4}\text{Mn}_{0.4}\text{Co}_{0.2}\text{O}_2$  compound via microwave synthesis method and the cathode performed an initial discharge capacity of  $156 \text{ mAhg}^{-1}$ . Although there are some efforts to use microwave synthesis for NMC cathode materials, the crystallinity and homogeneity of the final powders typically are not sufficient, particularly in the case of multi-elements [118–121].

Spray pyrolysis is also an attractive method since it provides better control on the particle size and morphology [114]. It also allows the synthesis of a wide variety of complex compositions, thus there is increasing interest in the spray pyrolysis method [10,122–126]. Since the interest of this thesis is spray pyrolysis as a production method, it is described in a greater detail in the following section.

### 2.3.1 Powder Synthesis via Spray Pyrolysis

Spray pyrolysis is an aqueous solution-based method to produce typically spherical, hollow and porous structure by the reaction of the precursors at high temperatures [103]. It is very similar to combustion methods due to the production of gases and oxidation of the aqueous precursors during the process [127,128].

Spray pyrolysis system is typically composed of a reservoir for precursor solution, atomizer (droplet generator), a reactor and collection unit. Droplets are created using a nebulizer and then carried by a gas, typically O<sub>2</sub>. This is followed by evaporation and separation of droplets into solid particles at the reactor. Nucleation and growth processes take place in the reactor. The solid particles synthesized are collected by the electrostatic precipitator at the exit of the reactor. The formation of the solid hollow particles through the process is described in Figure 13.

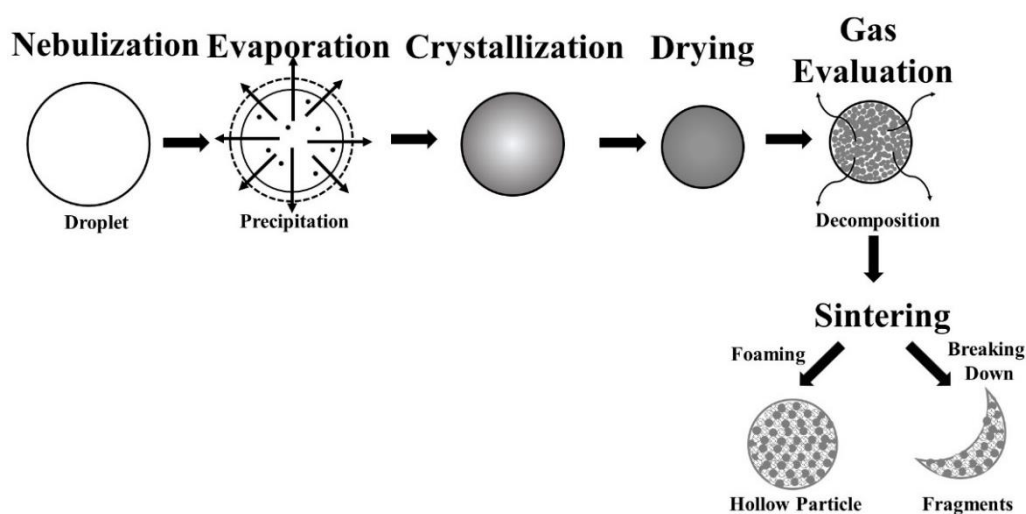


**Figure 13.** Schematic representation of the droplet-to-solid particle conversion route during spray pyrolysis process (adapted from [129,130]).

The droplets produced have generally uniform size and the average particle size can be predicted from the Lang equation given below;

$$D = 0.34 \left( \frac{8\pi\gamma}{\rho f^2} \right)^{1/3} \quad (3)$$

where  $D$  is the diameter of the droplet,  $\gamma$  is the surface tension of the liquid,  $\rho$  is the density of the liquid and  $f$  is the frequency of ultrasonic irradiation.

Spray pyrolysis method has taken attention due to its capability of homogeneous mixing of precursors, having short residence time, yielding high purity and diversity in compositions with ease as compared to conventional processes [131]. Additionally, spray pyrolysis allows single step production at relatively lower temperatures at a lower cost [132]. Thus, spray pyrolysis has become a well-known method which is simple, continuous, and suitable for scale-up production [126,129].

The solvents and additives affect the droplets formation and also morphology of the final particles. Similarly, the selection criteria of raw materials are also important due to the variable solubility, weight, and decomposition temperature [127,133]. The solubility of the precursors is important because of the formation of different precipitates at different saturation concentrations, resulting in the non-uniform composition of the particles. Additives are used to modify the solution, so as to prevent agglomeration. A carrier gas, i.e. oxygen in this study, is important because it was used also as a reactive gas to obtain the oxide of cathode material. The time spent in the furnace of the droplet has an effect on the particle size and hence the dependence of this ratio must be taken into account. Similarly, the reaction temperature has the same importance due to its effect on particle size and crystallinity. Spray pyrolysis enables to control these parameters to allow the formation of the spherical, hollow and porous structure during the production of cathode materials.



## CHAPTER 3

### EXPERIMENTAL PROCEDURE

#### 3.1 Synthesis of $\text{Li}(\text{Ni}_x\text{Mn}_y\text{Co}_{1-x-y})\text{O}_2$

NMC cathode materials with various Ni:Mn:Co mole ratio, 1:1:1 (NMC-111), 2:2:6 (NMC-226), 2:6:2 (NMC-262), 6:2:2 (NMC-622) and their W, Mo, Ag and Cu doped equivalents were synthesized via spray pyrolysis. A schematic representation of spray pyrolysis apparatus used in the current study is given in Figure 14. Spray pyrolysis system comprises a reservoir for precursor solution, an atomizer, a reactor and a collection unit.

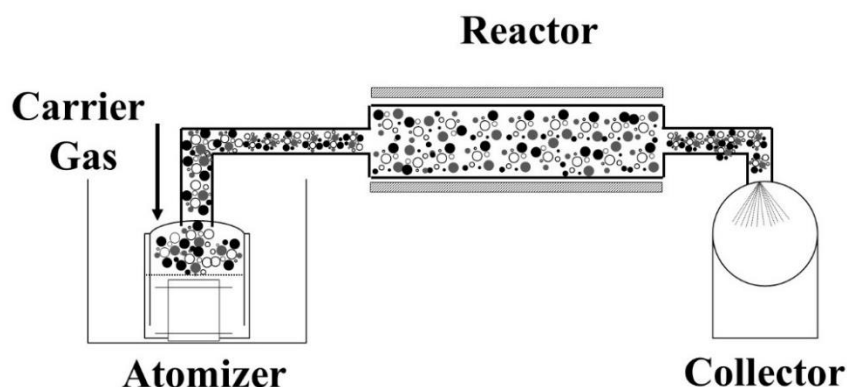


**Figure 14.** Schematic of spray pyrolysis system.

In a typical synthesis, precursor powders were produced via nebulizing the aqueous solution of the dissolved salts using an ultrasonic nebulizer operating at 1.7 MHz frequency. Droplets were then carried into the quartz tube reactor of 7 cm diameter which placed in a three-zone tube furnace by a carrier gas, i.e. argon, air or oxygen.

The salts used were the nitrates and acetates of the respective elements. Citric acid (CA) and ethylene glycol (EG) were also added into the solutions. CA was used as a chelating agent and EG was used as a dispersant. Moreover, oxalic acid, and N,N Dimethylformamide (DMF) were also added into the solution to modify the morphology of the particles. The total concentration of the solution was in the range of 0.3-0.5 M with additives of CA and EG. The flow rate of carrier gas was used in the range of 4-10 l/min. The reactor temperature during synthesis was ranging from 500 to 800 °C. The powders were collected at the end of the reactor by an electrostatic precipitator. The powders produced were then subjected to further heat-treatment. All NMC active materials were produced using this procedure. The parameters studied are summarized in Table 2.

**Table 2.** Parameters tried to be optimized during preliminary experiments. ‘A’ and ‘N’ are used to abbreviate acetate and nitrate salts of Li, Ni, Mn, and Co, respectively.

<b>Production Parameters</b>	<b>Cathode Material Li(Ni<sub>1/3</sub>Mn<sub>1/3</sub>Co<sub>1/3</sub>)O<sub>2</sub></b>
<b>Raw materials</b>	ANAA – NNNN – ANAA
<b>Ethylene Glycol (EG) (M)</b>	0 – 0.3
<b>Citric Acid (CA) (M)</b>	0 – 0.3
<b>Oxalic Acid and DMF (M)</b>	0.1 and 0.1-1
<b>Carrier Gas</b>	Argon, Air, Oxygen
<b>Flow Rate (lt/min)</b>	4, 8, 10
<b>Reaction Temperature (°C)</b>	500, 600,800
<b>Post Heat-Treatment - Temperature (°C)</b>	800, 900,1000
<b>Post Heat-Treatment - Duration (h)</b>	2, 4, 8, 12, 20

### 3.2 Electrode fabrication and cell configuration

For cathode preparation, powders were mixed with polyvinylidene difluoride (PVDF) and carbon black with a respective ratio of 86:7:7. PVDF was used as a solution after dissolved in N-methyl pyrrolidinone (NMP). This solution was then mixed with Li(Ni<sub>x</sub>Mn<sub>y</sub>Co<sub>1-x-y</sub>)O<sub>2</sub> and carbon black which resulted in a slurry. This slurry was stirred vigorously in order to get a uniform distribution of active materials.

The slurry was then coated on an aluminum foil and dried under vacuum at 120 °C for 12h. 18 mm diameter discs were cut from this electrode sheets, which were kept in the glove box until assembly of the cell. The content of the active materials,  $6 \pm 0.05 \text{ mgcm}^{-2}$ , was kept constant in all cathode materials. A glass fiber sheet with a density of  $52 \text{ gm}^{-2}$  was used as a separator in the cell assembly. The electrolyte (battery grade LP40, Merck) of 1 M  $\text{LiPF}_6$  in a 50: 50 ethylene carbonate:diethylene carbonate (EC:DEC) solution was used in all cells. The cells were assembled in a gas-tight structure in the glove box before the measurements.

### 3.3 Structural Characterization

The crystal structure of cathode materials was analyzed by an X-Ray Diffractometer (XRD, Bruker D8 Advance) using Bragg-Brentano geometry with  $\text{Cu-K}\alpha$  radiation. The XRD patterns were collected with a scan rate of  $2^\circ/\text{min}$ . Lattice parameters and oxygen positions of cathode materials were determined using a Rietveld analysis software (MAUD ver. 2.79) [134]. In this manner, Li-gap, shown schematically in Figure 15, was calculated by given equation below using z oxygen parameter and c lattice parameter refined [135,136].

$$Li - gap = \left(\frac{2}{3} - (2xz)\right)xc \quad (4)$$

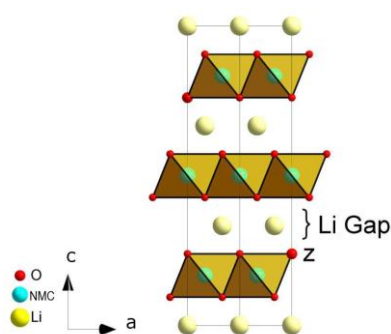


**Figure 15.** Schematic illustration of Li-gap in NMC structure.

Morphology of cathode materials was investigated by a scanning electron microscopy (SEM, Nova NanoSEM 430) using 20 kV accelerating voltage. Atomic structure of the cathode materials was investigated by a high-resolution transmission electron microscopy (HRTEM, Jeol JEM-2100F UHR/HRP Transmission Electron Microscope) in bright field (BF) imaging mode at 200 kV. Selected area electron diffraction (SAED) patterns of cathode materials were collected with the same parameters.

Particle size measurements of the active materials were performed using a laser diffraction particle size analyzer (Mastersizer 2000), where the powders were dispersed in ethanol.

Physical adsorption studies were mainly carried out to obtain a sample surface area, and pore size using Autosorb-6.

### **3.4 Chemical Characterization**

Energy Dispersive Spectroscopy (EDS) was performed as the first step for the chemical analyses. EDS is an easy and convenient method to qualify and quantify the chemical ingredients of the produced powders. However, it can detect elements that have a higher atomic number than 10. Therefore, inductively coupled plasma mass spectroscopy (ICP-MS) was used so as to have more accurate results in the produced powder, particularly for lithium content. ICP measurements in the study were performed via ICP-MS, Perkin Elmer DRC II.

Surface chemistry and the oxidation states of the cathode materials were analyzed by an X-ray photoelectron spectroscopy (XPS, PHI 5000 VersaProbe) using a monochromatic Al  $K_{\alpha}$  radiation at 1486.6 eV. The spot area was used as 200  $\mu\text{m}$  and 100  $\mu\text{m}$  in the respective orders for survey and tight scans. The analyzer positioned at an angle of 45 ° to the surface of the sample. Survey spectra of the samples were

scanned at a pass energy of 187.85 eV, while the tight scans of the elements were collected at a pass energy of 58.70 eV. XPS spectra of the samples were normalized using the C1s binding energy of 284.8 eV. C, O, Li, Ni, Co, Mn, Mo, W, Ag and Cu elements in the active materials were scanned in a binding energy range of 275-300, 520-540, 50-70, 540-900, 630-670 and 75-100, 760-820, 220-240, 30-45, 360-380 and 530-660 eV, respectively.

### 3.5 Electrochemical Characterization

Open-circuit voltage (OCV), charge-discharge behavior, discharge capacity and cycle life were measured using a potentiostat/galvanostat (Bio-Logic Instruments VMP-300). The electrochemical cells were cycled at 0.1C and 0.3C rate ( $1C=170 \text{ mAhg}^{-1}$ ) within 2.7-4.5 V and 2.7-4.2 V potential windows for undoped and doped NMC cathode materials, respectively.

Electrical impedance spectroscopy (EIS) measurements were performed in the frequency range from 300 kHz to 3 mHz with a 10 mV amplitude. The deconvolution of the typical EIS spectra proposed by Barsoukov *et al.*, [137] for particularly intercalated cathode materials, is given in Figure 16.

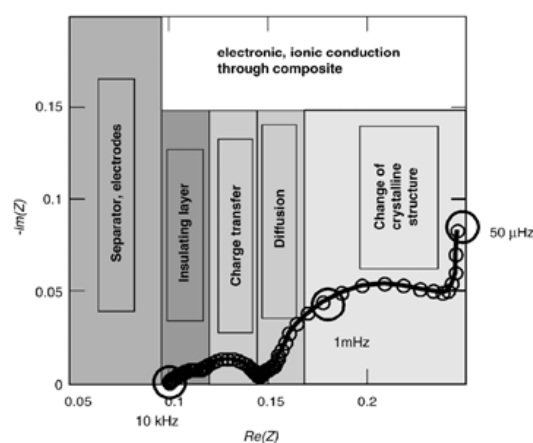


**Figure 16.** Deconvolution of EIS spectra proposed by Barsoukov *et al.*, [137].

Here, there are several steps depending on the presence of electrochemical reactions in intercalated cathode materials. These are ionic charge conduction through the electrolyte, lithium ion diffusion through the surface of the insulating layer, electron charge transfers at the interface of active materials, lithium ion diffusion in the solid phase and the capacitive behavior that is related to the occupation of lithium ions. The reactions were given in the respective order with Figure 16 from high frequency to low frequency.

The fittings for EIS spectra was performed using Randles circuit, shown in Figure 17. Finite Space Warburg element was used to define the boundary conditions for the diffusion of lithium ions as a Warburg-type element. The brief description of this model based on `blocking` outer interface is given below.

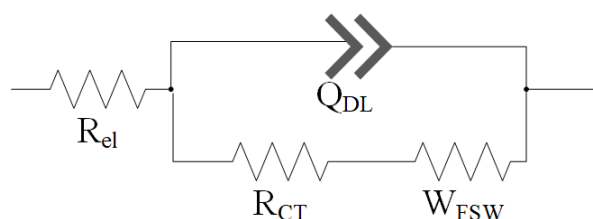


**Figure 17.** Equivalent circuit models used in the study, where  $R_{el}$  is electrolyte resistance,  $R_{CT}$  is charge transfer resistance. Eventually,  $Q_{DL}$  represents the constant phase element for the double layer and  $W_{FSW}$  the finite space Warburg element for Li-ion diffusion.

Here, it is important to define boundary conditions in the explanation of Warburg-type element. The interface between electrode and electrolyte, where the current flux of lithium is zero, can be defined as a first boundary condition. The second boundary condition depends on type of the diffusion. When the secondary boundary condition is infinite, it describes a semi-infinite diffusion which yields the same impedance as in the case of constant phase element. On the other hand, when no flux is allowed at the second diffusion boundary, diffusion can be defined as finite diffusion where the element is described as Finite Space Warburg (FSW). For the active material of Li-

ion cells, this is comparable to the particle center where no flux of species is possible. Applying this boundary condition, the impedance of FSW has the following function;

$$Z_{FSW}(\omega) = \frac{RT}{nFC_0D} \cdot \frac{\coth\left[\frac{\delta}{\sqrt{D}}(j\omega)\right]}{\frac{\delta}{\sqrt{D}}(j\omega)} \quad (5)$$

where,  $\delta$  is the diffusion length,  $D$  is the diffusion coefficient and  $C_0$  is the concentration of the diffusing species. Square of the  $\delta/\sqrt{D}$  ratio is the characteristic time constant of the diffusion process. This impedance function assuming one-dimensional diffusion path and it has characteristic 45° slope for high and pore capacitive behavior for low frequencies [138].



## CHAPTER 4

### RESULTS AND DISCUSSION

#### 4.1 Processing Preliminary Parameters

In this study, it was aimed to produce NMC layered oxides as loose aggregates of spherical particles, thus a series of optimization experiments were carried out in spray pyrolysis approach. The optimized process variables are given Table 3.

**Table 3.** Spray pyrolysis parameters optimized.

<b>Production Parameters</b>	<b>Cathode Material Li(Ni<sub>1/3</sub>Mn<sub>1/3</sub>Co<sub>1/3</sub>)O<sub>2</sub></b>
<b>Raw materials</b>	NNNN
<b>EG (M)</b>	0.1
<b>CA (M)</b>	0.05
<b>Oxalic Acid and DMF (M)</b>	None
<b>Carrier Gas</b>	Oxygen
<b>Flow Rate (lt/min)</b>	8
<b>Reaction Temperature (°C)</b>	600
<b>Post Heat-Treatment - Temperature (°C)</b>	800
<b>Post Heat-Treatment - Duration (h)</b>	20

The details for preliminary studies for the optimization of parameters are explained in the following sections.

### 4.1.1 Selection of Precursors

Precursor selection is quite important since it could directly affect the properties of the final product. In the selection criteria, properties such as molecular weight, solubility and decomposition temperature should be taken into consideration. In the study, both nitrate and acetate salts of the respective metals were examined so as to synthesize  $\text{Li}(\text{Ni}_x\text{Mn}_y\text{Co}_{1-x-y})\text{O}_2$ .

The precursors were firstly examined due to their effect on resulting crystal structure in the active materials. The analyses of the active materials produced using acetate and nitrate salts showed that the crystallinity and the hexagonal ordering in powders were almost the same, Figure 18.

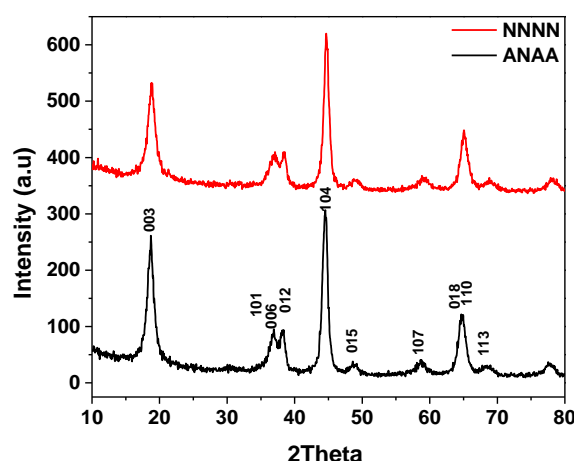


**Figure 18.** XRD spectra of NMC-111 cathode materials produced using acetates and nitrate salts.

Here, the solubility of the precursors is particularly critical, since it can lead to the formation of different concentrations which might affect the particle morphology in resulting powders. Additionally, using different concentrations also affects the nebulization behavior of the solutions. Of the salts used in the study, the solubility of the acetate salts is generally lower, e.g. solubility of lithium acetate is ~45 mg/100ml

whereas solubility lithium nitrate is 90 mg/100ml, as compared to nitrate salts of the respective metals. Here, it should be mentioned that the solutions prepared using acetate salts had resulted in lower yield even nebulization process required longer times. One can, therefore, expect the resulting particle morphology to be affected from this. The active materials synthesized were investigated according to their particle morphology. SEM images of typical particle morphology obtained using acetate and nitrate salts of the respective metals is given in Figure 19. The particle morphology of the active material synthesized by acetate salts resulted in the collapsed morphology where synthesis with nitrate salts resulted in homogeneous particle morphology.

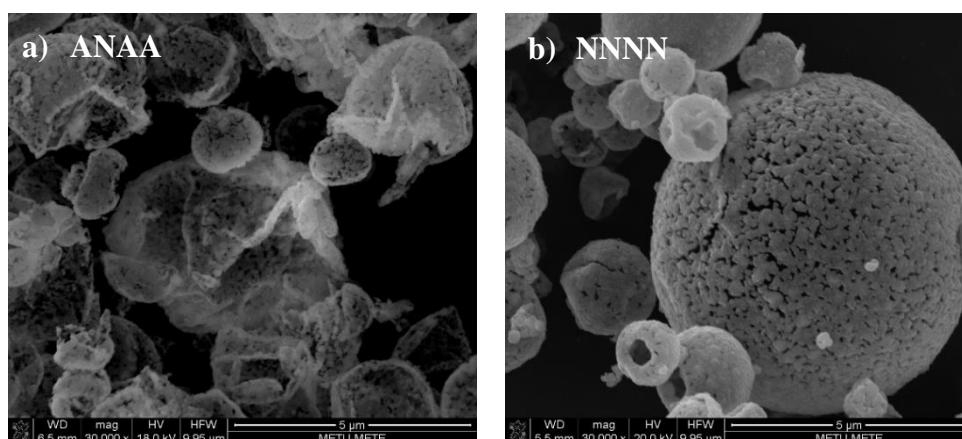


**Figure 19.** SEM images of NMC-111 cathode materials produced by a) ANAA, and b) NNNN. Here, “A” represents the acetate salt as a precursor for the respective metal, where “N” stands for nitrate salts.

In this respect, the nitrate salts of the respective metals were chosen for further experiments according to their higher yield and resulting particle morphology. Nebulization of acetate solution was found to be more difficult than nitrate salts where the binding of acetate ( $\text{CH}_3\text{COO}^-$ ) ions is stronger than nitrate ( $\text{NO}_3^-$ ) ions, so as to lead higher viscosity [139]. In addition, the surface area of the materials synthesized by the acetates had a surface area of about half that of the materials synthesized via the nitrate salts.

#### 4.1.2 Determination of Additives

In principle, additives are used to control physical properties of particles synthesized. Thus, different additives with different ratios were tried in this study. CA was used as a chelating agent so as to obtain spherical powders and EG was used to control the morphology. In addition to them, oxalic acid and DMF were used to control the agglomeration and the particle growth.

The powders were synthesized using a different amount of CA and EG ranging from 0 to 0.3 M at 600°C. The typical SEM images for the powder synthesized are given in Figure 20. It was observed that increase in the additive amount made easier to obtain spherical powders. As seen, the spherical morphology could not be obtained without using additives. The formation of spherical particle morphology started to be observed with the use of 0.1 M CA and EG. It was observed that 0.3 M CA and EG resulted in larger primary particles affecting the active surface area. Thus, 0.1 M for both CA and EG yielding spherical morphology was chosen for further studies.

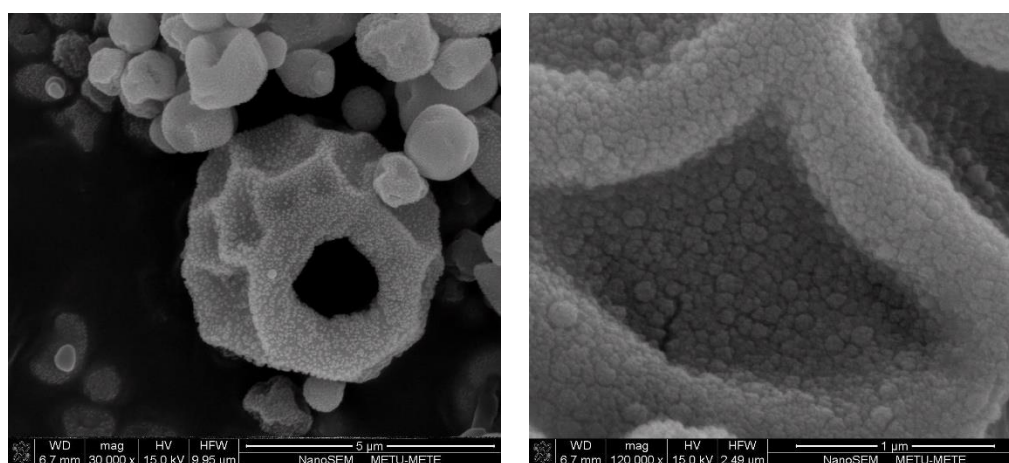


**Figure 20.** SEM images of NMC cathode materials produced at 600°C with a) no additive, with b) both 0.1M CA and EG, and with c) both 0.3M EG and CA.

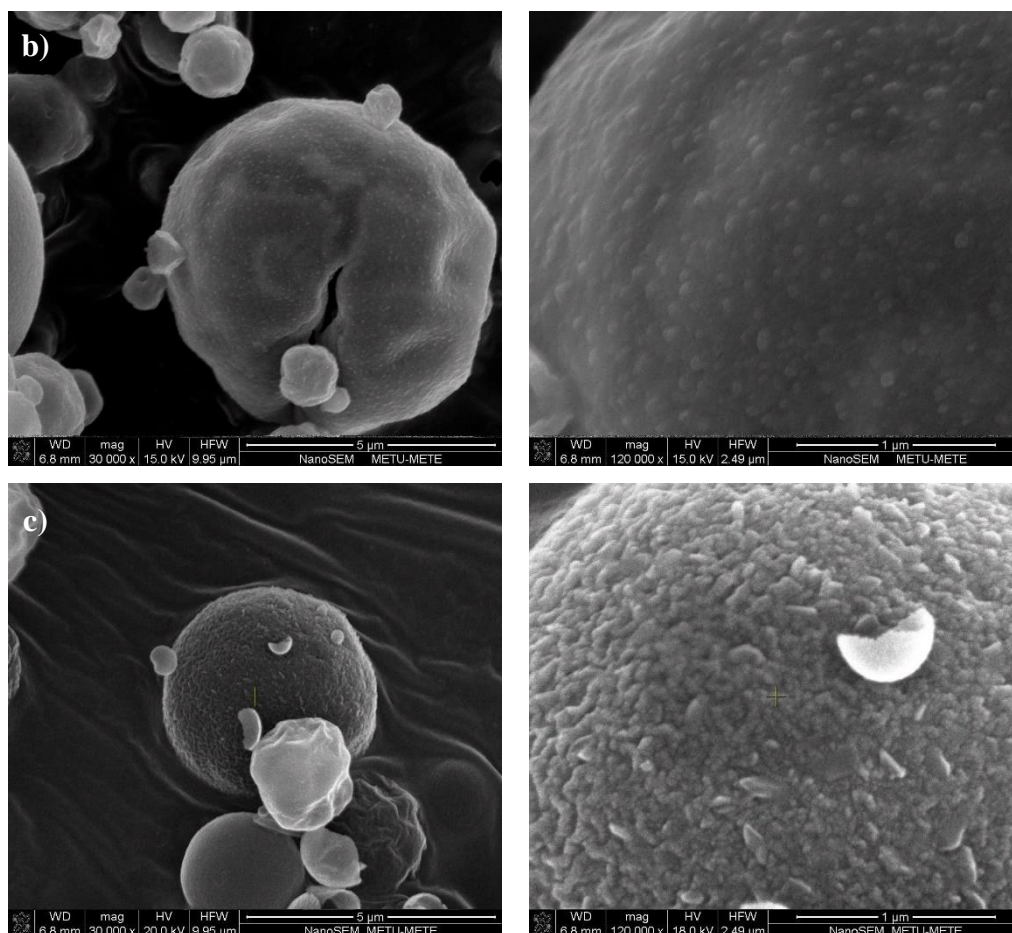


**Figure 20.** Cont' d

The co-use of CA and EG with different variation was also examined for fine tuning of resulting particle morphology. The representing SEM images are given in Figure 21. The desired loose aggregate morphology discussed above was obtained with the use of 0.05 M CA and 0.1 M EG.

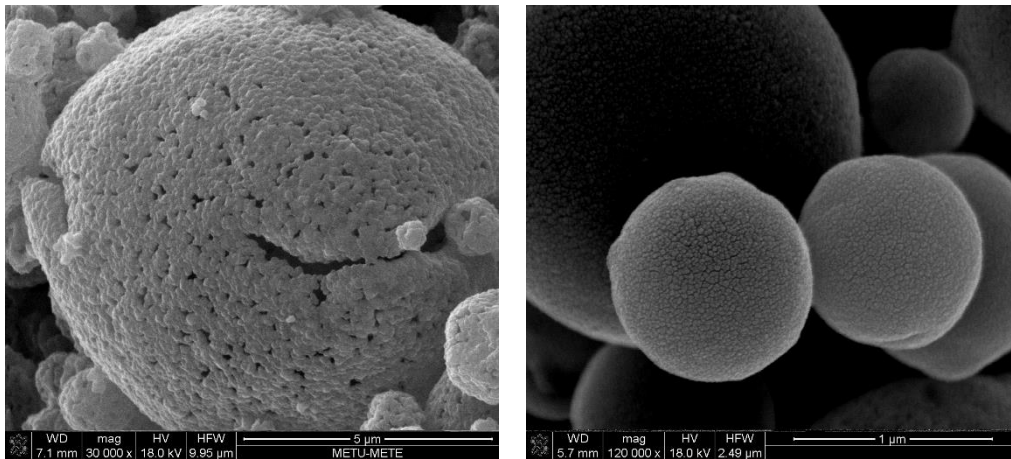


**Figure 21.** SEM images of NMC cathode materials synthesized with an addition of 0.1 M EG and 0.05 M CA at 600°C.

The effect of oxalic acid and DMF on the particle morphology was also investigated. SEM images of cathode material NMC-11,1 which were produced with the addition of 0.1M oxalic acid, 0.1 M DMF, 0.3 M DMF and 1 M DMF, were given in Figure 22, respectively. The use of oxalic acid and DMF particularly affected the size of primary particles in the spherical aggregates. Besides, they affected the pores within the primary particles, where the addition of these additives resulted in dense aggregates. Since the use of oxalic acid and DMF resulted in a denser morphology, they were not considered for further experiments.

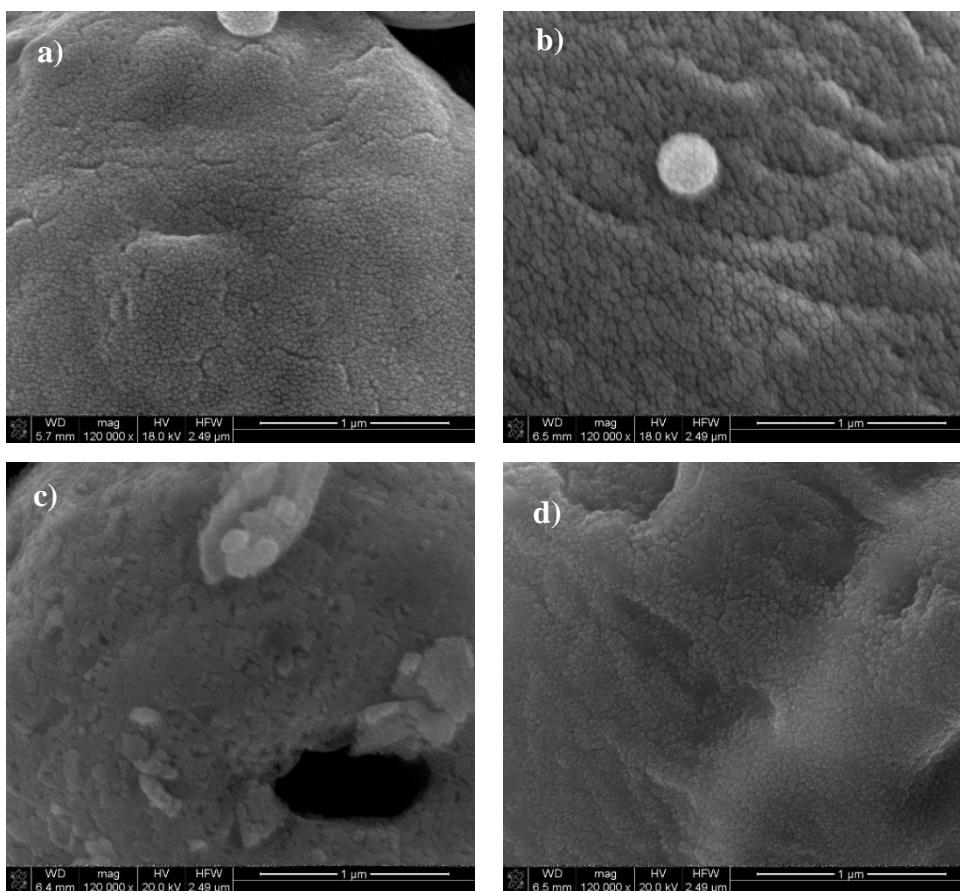


**Figure 22.** SEM images of NMC cathode materials produced with an additive of a) 0.1M oxalic acid, b) 0.1 M DMF c) 0.3 M DMF and d) 1 M DMF.

#### 4.1.3 Carrier Gas

The effect of carrier gases, i.e. argon, air, and oxygen, were examined in the study. Argon as a carrier gas resulted in a compound which couldn't be identified. XRD pattern of this compound is given in Figure 23.a.

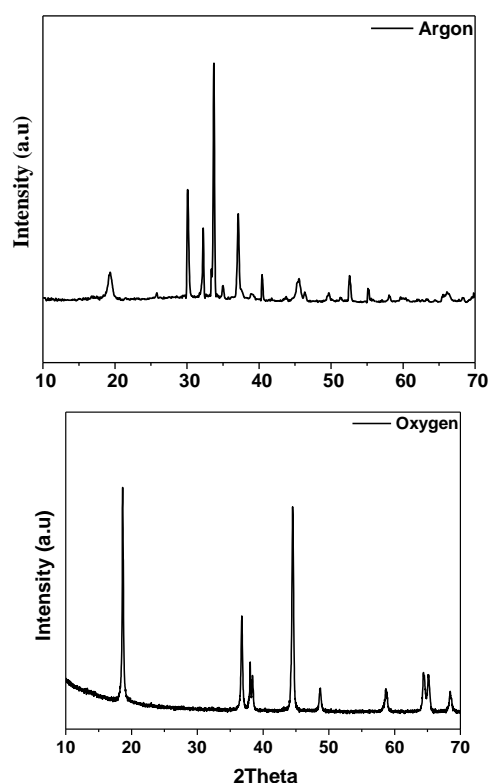


**Figure 23.** XRD spectrum of NMC cathode synthesized under a) argon, and b) oxygen atmosphere.

Air as a carrier gas was efficient to allow oxidation process resulting in the oxide phase. However, pure oxygen was also studied to ensure the oxidation and the avoid the oxygen-deficient structure. Typical XRD pattern of NMC-111 synthesized with oxygen carrier gas is given in Figure 23.b.

The flow rate was also examined to check whether there is any effect on the synthesis of the active materials. The flow rate of 4, 8 and 10 l/min were studied. Here, it should be noted that when the flow rate is high, the duration of stay in the reactor would be shorter which causes the decrease in particle size and the reacted fraction of the precursors in the reactor. Thus, it is important to allow enough time for the droplets of precursors for the complete reaction. In this respect, 8 l/min was selected as an optimum flow rate, where the all fraction of the droplets was reacted.

#### 4.1.4 Reaction Temperature and Post-Heat-treatment

The effect of reaction temperature, i.e. 500, 600 and 800 °C, on the crystal structure of resulting powder was investigated. XRD patterns of NMC cathode materials as-synthesized at 500°C, 600°C, and 800°C are given in Figure 24. XRD pattern of NMC cathode synthesized at 500°C showed the formation of some impurity phases, while NMC cathode materials were synthesized at 600°C and 800°C without any impurity phase. However, the splitting of (006)/(102) and (108)/(110) peaks, which is an indicator for good hexagonal ordering and layered structure, was not sufficient. Thus, all active materials required to be heat treated so as to obtain desired structure ordering. Since the post heat-treatment was inevitable, the reaction temperature was chosen at a lower temperature to avoid grain growth. In this respect, the reaction temperature was determined to be 600 °C, where no impurity phases were observed among the lower temperatures.

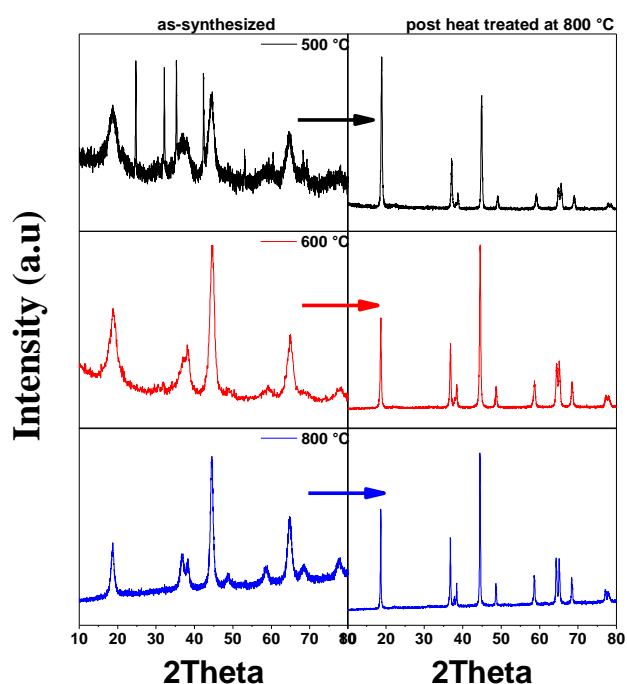


**Figure 24.** XRD patterns of the NMC cathode materials as-synthesized at 500°C, 600°C, and 800°C and post heat-treated at 800°C.

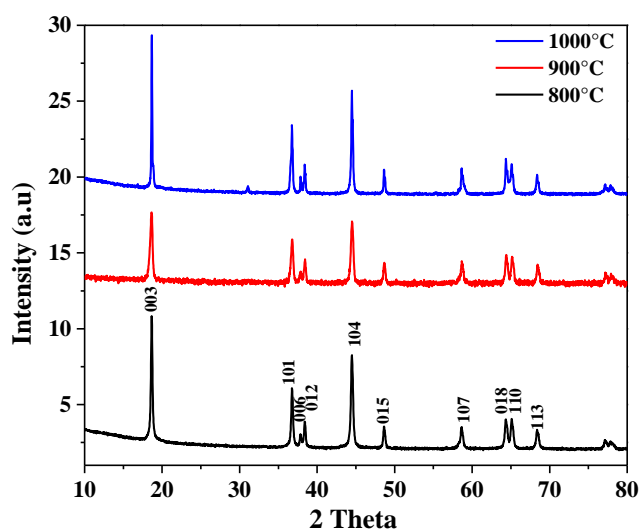


**Figure 25.** XRD patterns of layered NMC-111 cathode materials produced by spray pyrolysis and then post heat-treated at 800 °C, 900 °C, and 1000 °C.

Various temperatures ranging from 800 to 1000 °C were investigated so as to determine the temperature for the post heat-treatment. X-ray diffraction analyses were carried out for all active materials to check their structural properties such as crystallinity and phase purity. It was found that NMC-111 with crystalline structure could be obtained by a post heat-treatment performed between 800-1000 °C, Figure 25.

Different durations such as 2h, 4h, and 8h for each post heat-treatment temperature were also studied so as to reveal the effect on the particle size and morphology. SEM images for NMC-111 cathode materials for each duration is given in Figure 26.

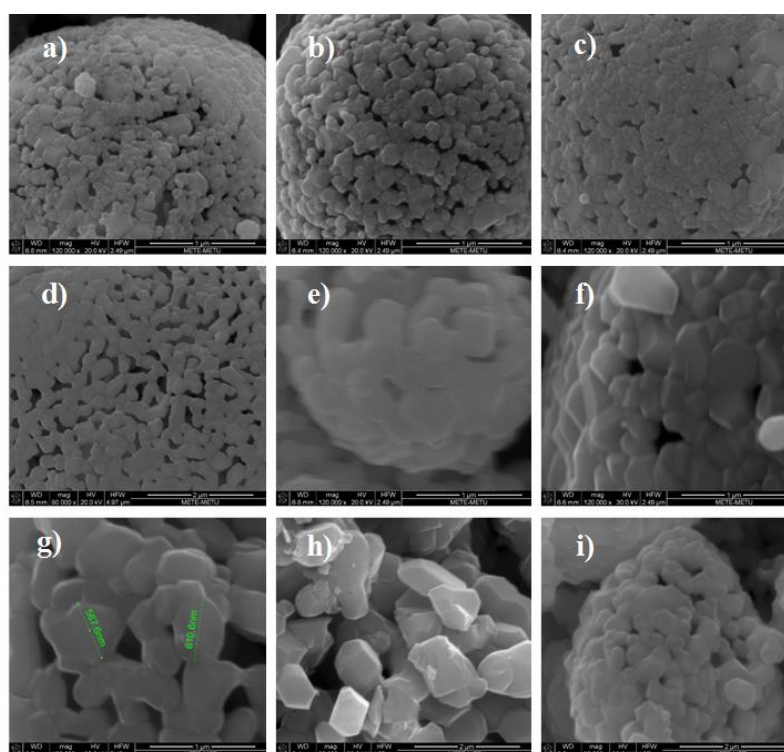


**Figure 26.** SEM images of NMC-111 cathode materials heat-treated at a) 800 °C for 2h, b) 800 °C for 4h, c) 800 °C for 8h, d) 900 °C for 2h, e) 900 °C for 4h, f) 900 °C for 8h, g) 1000 °C for 2h, h) 1000 °C for 4h and i) 1000 °C for 8h.

The powders preserved their spherical morphology when they heat-treated at 800 °C and 900 °C for all durations. There was also some degree of particle growth with increasing amount of treatment. However, heat-treatment at 1000 °C resulted in destruction in this morphology. Besides, the primary particles were coarsened too much. The optimum post heat-treatment parameters were selected so as to obtain the highest crystallinity with the lowest average particle size. Thus, heat-treatment at 800 °C was selected, where a good hexagonal ordering with a high crystallinity could be obtained. In terms of the duration, a comprehensive study was carried out including electrochemical measurements and determination of structural parameters for active materials.

It should be noted that lithium is a volatile element and there might be losses depending on the temperature and particularly for longer duration in the post heat-treatment. This often resulted in Li deficiency causing secondary phases [140]. Additionally, excess Li is suggested in many studies to improve the electrochemical properties in layered oxides [141]. For this reason, both to improve electrochemical performance and to avoid any structural problems in structure, active materials with excess lithium (5%) was also included the studies.

The cathode materials with stoichiometric Li and excess Li were heat-treated with durations of 2, 4, 8, 12 and 20h. Here, the main reason to increase the duration for heat-treatment was to increase the ratio of the peak intensities in  $I_{[003]}/I_{[104]}$  which is an important parameter indicating ordering characteristics of cathode materials. In the case of  $I_{[003]}/I_{[104]}$  is higher than 1.2, the cation mixing is small, whereas the ratio lower than 1.2 indicates a considerable extent of cation mixing. Besides, a separated (006)/(102) and (108)/(110) doublets indicate the good hexagonal ordering in the layered structure.

The cathode materials in stoichiometric amount is labeled as 800-t (t=2,4,8,12 and 20), and Li-excess equivalents are labeled as 800-5Li-t(t=2,4,8,12 and 20). XRD patterns of respective cathode materials are given in Figure 27 and Figure 28.

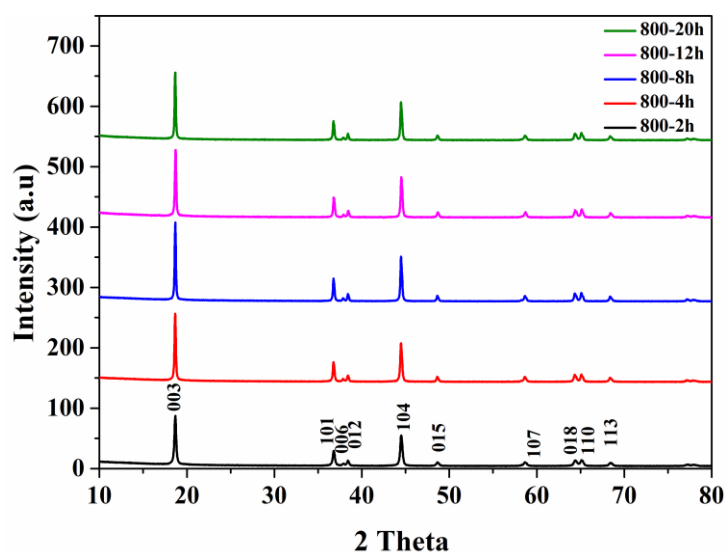


**Figure 27.** X-ray pattern of cathode materials heat-treated at 800°C for 2, 4, 8, 12 and 20h.

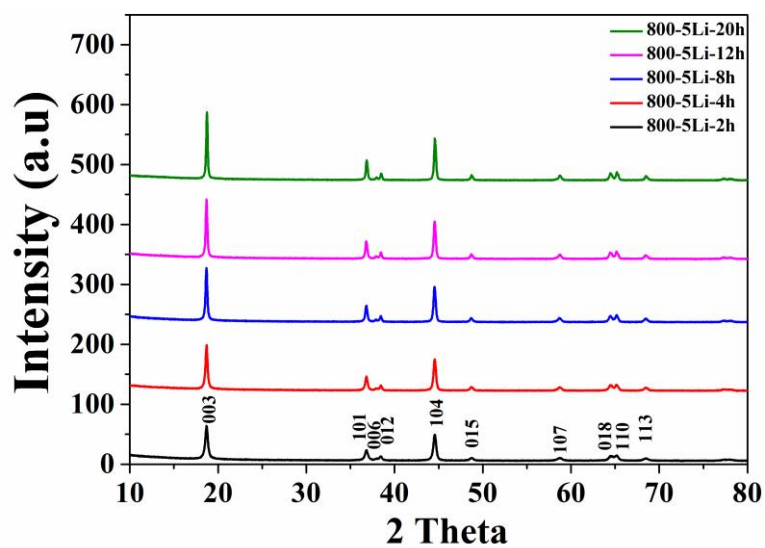


**Figure 28.** X-ray pattern of cathode materials with 5% excess Li heat-treated at 800°C for 2, 4, 8, 12 and 20h.

XRD patterns were also processed with Rietveld analysis to determine the lattice parameters  $a$ ,  $c$  and oxygen position,  $z$ , summarized in Table 4.

**Table 4.** The lattice parameters, oxygen positions and Li-gap size of all synthesized cathode materials.

Name	a (Å)	c (Å)	c/a	% Rw	$I_{[003]}/I_{[104]}$	Oxygen Parameter (z)	Li-gap Size
<b>800-2h</b>	2.863	14.245	4.975	9.525	1.396	0.2586	2.1290
<b>800-4h</b>	2.864	14.247	4.975	9.217	1.400	0.2597	2.0981
<b>800-8h</b>	2.865	14.249	4.974	9.344	1.436	0.2588	2.1240
<b>800-12h</b>	2.865	14.251	4.973	5.475	1.463	0.2586	2.1203
<b>800-20h</b>	2.865	14.247	4.973	8.066	1.449	0.2586	2.1258
<b>800-5Li-2h</b>	2.862	14.196	4.961	5.389	1.301	0.2584	2.1275
<b>800-5Li-4h</b>	2.861	14.200	4.963	5.059	1.406	0.2583	2.1298
<b>800-5Li-8h</b>	2.862	14.209	4.965	5.548	1.495	0.2588	2.1160
<b>800-5Li-12h</b>	2.862	14.202	4.963	5.627	1.527	0.2587	2.1172
<b>800-5Li-20h</b>	2.864	14.241	4.972	5.592	1.624	0.2587	2.1257

The highest  $I_{[003]}/I_{[104]}$  ratio was measured as 1.463 for the 12h treated stoichiometric compound, while for the Li-excess compounds, the highest  $I_{[003]}/I_{[104]}$  ratio, 1.624, was obtained for the 20h treated sample.

The cathode materials were also investigated by SEM to compare their morphology. SEM images for stoichiometric and Li-excess active materials are given in Figure 29 and Figure 30, respectively. An increase in the presence of porosity in spherical aggregates was observed with increasing duration of heat-treatment. This was valid for both stoichiometric and Li-excess cathode materials. Thus, 20h was promising due to its resulting morphology of loose spherical aggregates with slightly larger primary particles. Here, it should be mentioned that the primary particles with a larger size as possible while maintaining the spherical morphology is desirable. This is caused by the higher active surface area could increase the tendency of non-irreversible reactions with the electrolyte causing the higher impedance [142].

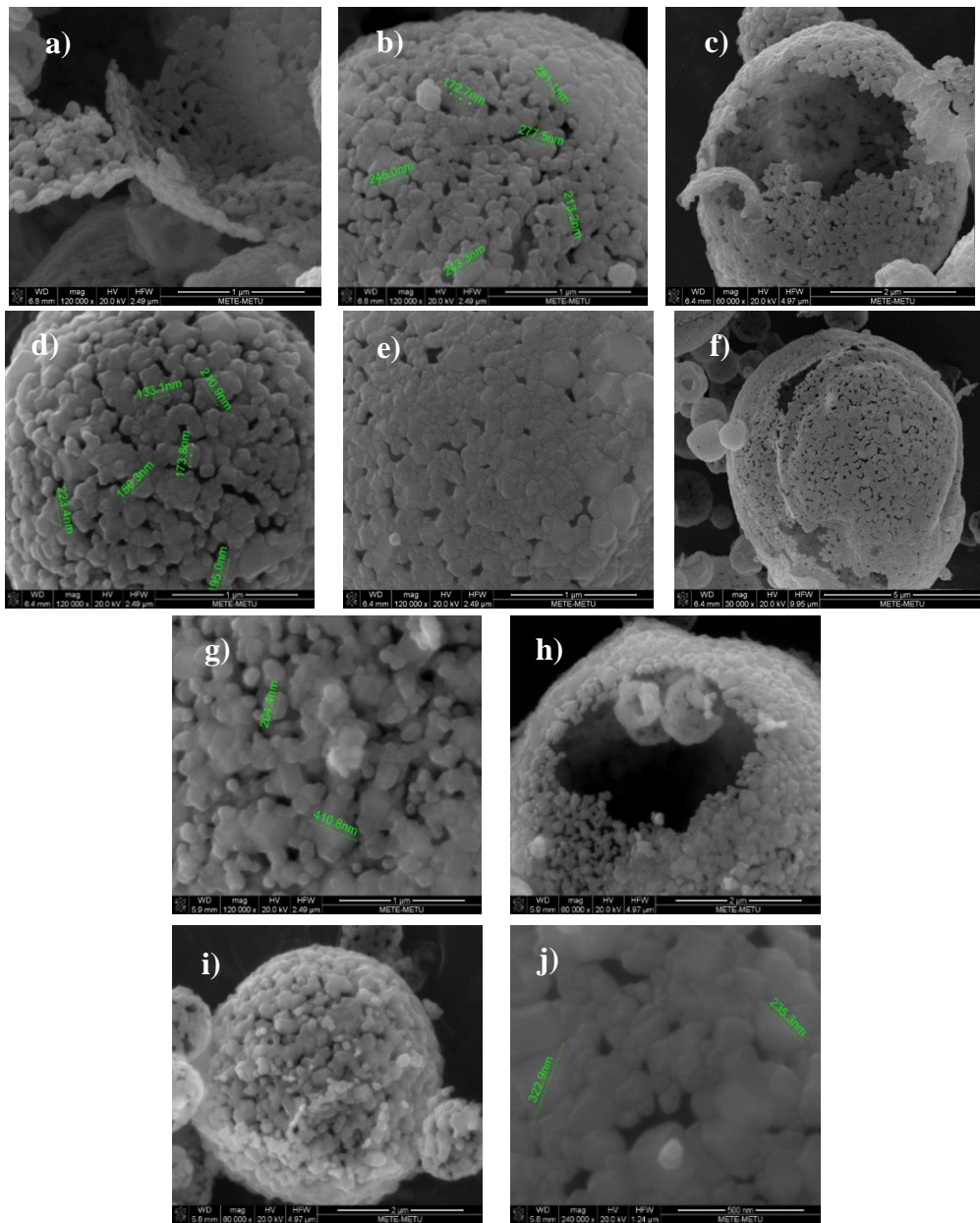


**Figure 29.** SEM images of cathode materials heat-treated at 800°C for 2h (a,b), 4h (c,d), 8h (e,f), 12h (g,h) and 20h (i, j).

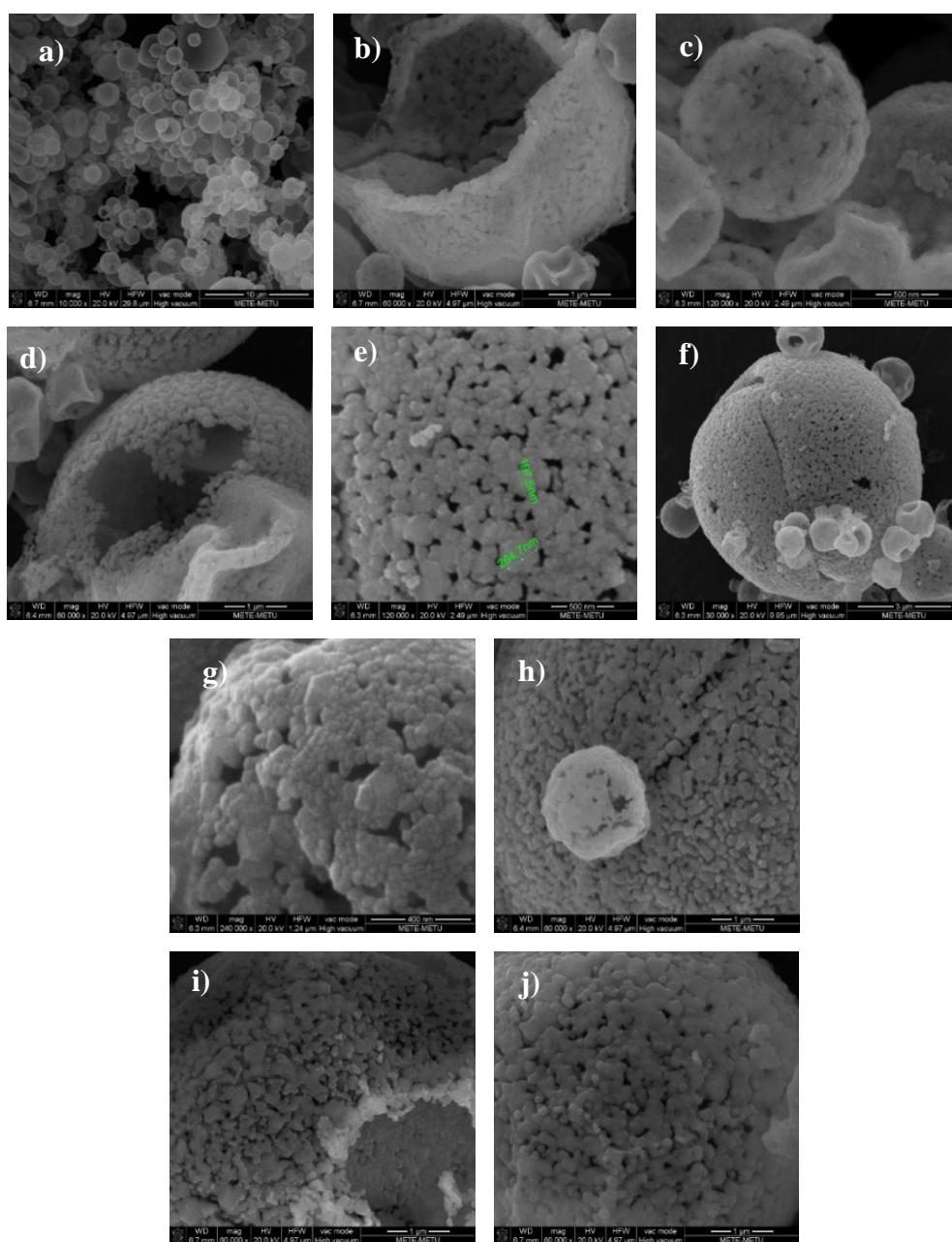


**Figure 30.** SEM images of synthesized cathode materials heat-treated using excess amount of Li at 800°C for 2h (a,b), 4h (c,d), 8h (e,f), 12h (g,h) and 20h (i, j).

The active materials were also investigated with respect to their particle size. Thus, particle size measurements for all cathode materials heat-treated for various duration was performed. Interestingly, the measurements resulted in the very similar curve for

their particle size distribution, Figure 31 and Figure 32. The average particle size of cathode materials was determined as about 10  $\mu\text{m}$ . It should be noted that this value should represent the size aggregates considering the SEM studies, where the primary particles were ranging from 100 nm to 300 nm. The prolonged treatment caused particle coarsening/coalescence and a tail in the particle size distribution above 100  $\mu\text{m}$  started to appear.

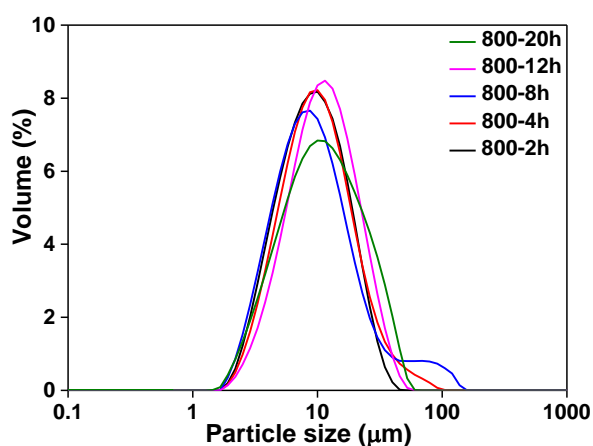


**Figure 31.** Particle size distribution of NMC-111 heat-treated at 800 °C for 2, 4, 8, 12 and 20h.

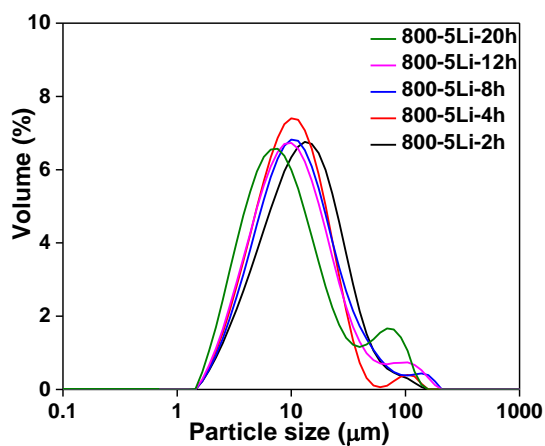


**Figure 32.** Particle size distribution of NMC-111 prepared using an excess amount of Li, heat-treated at 800 °C for 2, 4, 8, 12 and 20h.

The electrochemical measurements were also carried out so as to determine the ideal duration in heat-treatment. For this purpose, the electrochemical cells prepared were cycled at different rates 0.07C, 0.1C, and 0.2C ( $1C=170 \text{ mAhg}^{-1}$ ) within the potential window of 2.75–4.5 V. The electrochemical behaviors of cathode materials heat-treated at various duration is given in Figure 33-36. First discharge capacities are also shown in Table 5.

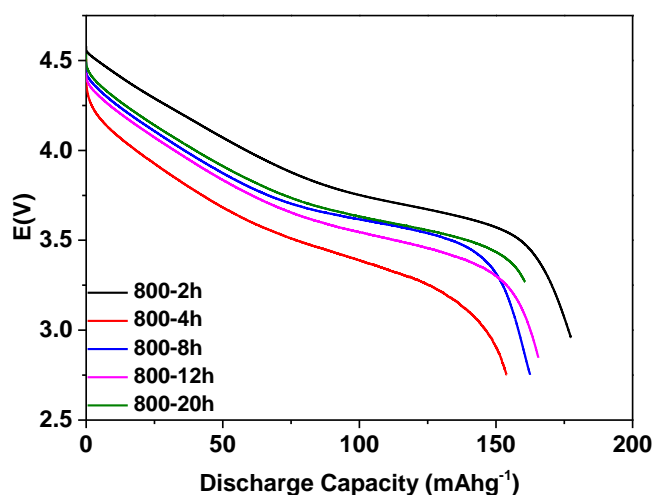


**Figure 33.** Voltage profiles of all samples, charged and discharged at 0.1C.

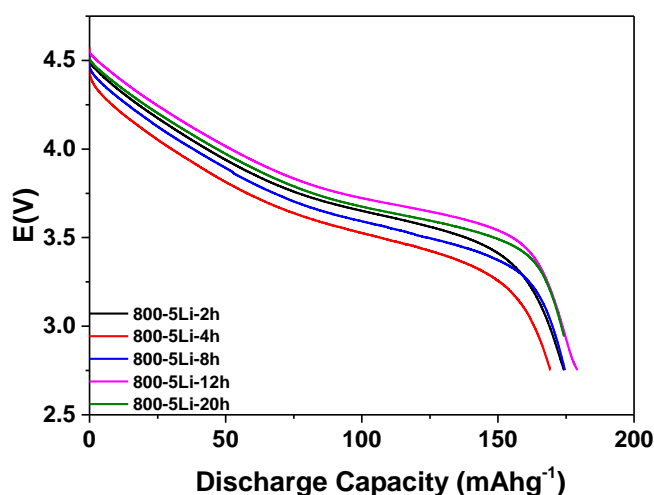


**Figure 34.** Voltage profiles of all excess amount of Li samples, charged and discharged at 0.1C.

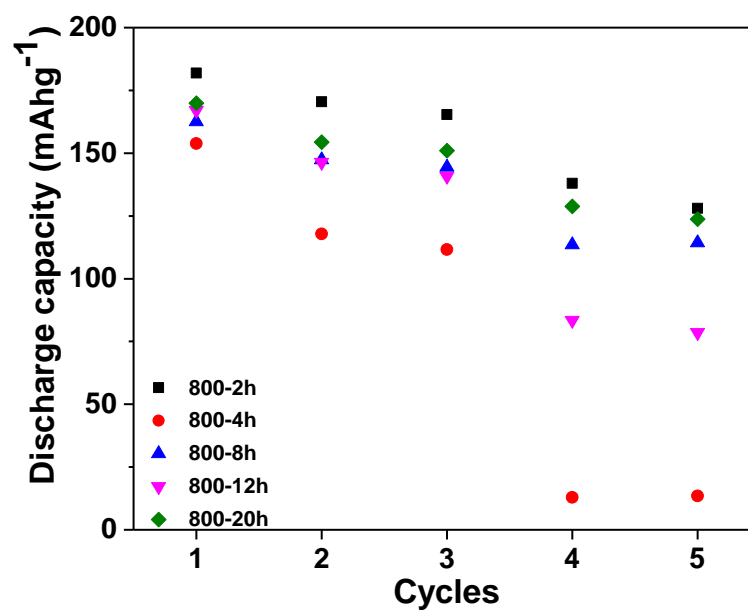


**Figure 35.** Comparison of charge-discharge tests of NMC-111 heat-treated at 800°C for 2, 4, 8, 12 and 20h.

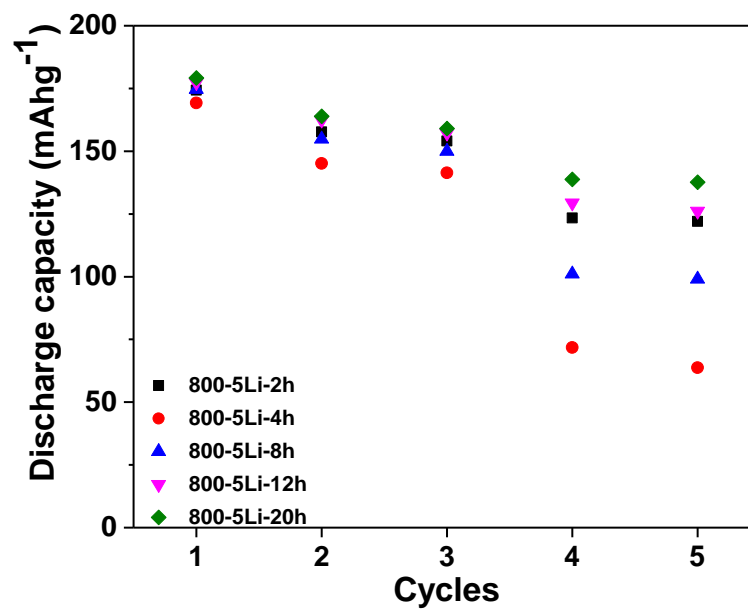


**Figure 36.** Comparison of charge-discharge tests of NMC-111 heat-treated using an excess amount of Li at 800°C for 2, 4, 8, 12 and 20h.

It was observed that Li-excess performed better electrochemical properties, particularly in terms of capacity retention. NMC-111 prepared using excess Li and heat-treated for 20h exhibited comparable capacity of  $177.35 \text{ mAhg}^{-1}$  among other samples with better capacity retention. Although, the stoichiometric cathode which heat-treated for 20h exhibited higher discharge capacity compared to Li-excess cathode, the capacity retention of this cathode was relatively smaller. The stoichiometric and Li-excess cathode materials heat-treated for 4h showed a sharp decrease in their discharge capacities. The cause of this decline was not fully specified but it might be due to the electrochemically active lithium loss. This loss of lithium was thought to originate from the undetectable NiO phase, which causes a partially deactivated  $\text{Li}_2\text{MnO}_3$  phase. Besides, Li-excess cathode materials performed better rate capability with respect to stoichiometric cathode materials with increasing discharge rates. Moreover, usage of lithium as excess in NMC cathode materials is a strategy to achieve the exact stoichiometry during heat-treatment and minimize the cation mixing [143]. It was also stated that excess lithium on surface layer of NMC cathode materials may react with dopants to form conductive lithium layers. Therefore, considering these approaches and the first results obtained so as to determine the process parameters, Li-excess cathode materials were chosen for further studies and 20h was selected for the post heat-treatment procedure.

**Table 5.** First discharge capacities of synthesized cathode materials.

	<b>First Discharge Capacity (<math>\text{mAhg}^{-1}</math>)</b>	<b>Capacity Retention after 5 cycle (%)</b>		<b>First Discharge Capacity (<math>\text{mAhg}^{-1}</math>)</b>	<b>Capacity Retention after 5 cycle (%)</b>
<b>2h</b>	181.89	70.4	<b>5Li-2h</b>	174.32	69.9
<b>4h</b>	153.87	8.8	<b>5Li-4h</b>	169.25	37.7
<b>8h</b>	162.51	70.3	<b>5Li-8h</b>	174.61	56.7
<b>12h</b>	167.04	47.0	<b>5Li-12h</b>	179.22	71.0
<b>20h</b>	187.61	72.8	<b>5Li-20h</b>	177.35	76.8

#### 4.1.5 Determination of Doping Replacement

In this study, undoped NMC cathode materials, as well as their doped equivalents, were studied. Doping elements, Table 6, were added in 2 wt.% for all compounds. The doping elements were particularly selected according to their ionic radius, Table 7, which are suitable for the NMC structure. In the preliminary experiments, doping elements were used aiming to replace only Co in NMC. However, this approach failed since the formation of secondary phases could not be avoided. This supports the effect of Co element in the structural stability of layered oxides. The doping elements were then used as a replacement for all transition metals equally in NMC, i.e. Ni, Mn, and Co. The radii of elements used in this study which was calculated by Shannon [144,145] for different oxidation states of elements were given depending on different oxidation states, in Table 7.

**Table 6.** The precursor of dopants using experiments.

	<b>Molecular Formula</b>	<b>Name</b>
<b>V</b>	$\text{NH}_4\text{VO}_3$	Ammonium vanadium oxide (Ammonium metavanadate)
<b>Cu</b>	$\text{Cu}(\text{NO}_3)_2 \cdot 5\text{H}_2\text{O}$	Copper (II) nitrate hemi(pentahydrate)
<b>Fe</b>	$\text{FeSO}_4 \cdot 7\text{H}_2\text{O}$	Iron (II) sulfate heptahydrate
<b>Cr</b>	$(\text{NH}_4)_2 \cdot \text{CrO}_4$	Ammonium chromate
<b>Y</b>	$\text{Y}(\text{NO}_3)_3 \cdot 6\text{H}_2\text{O}$	Yttrium(III) nitrate hexahydrate
<b>W</b>	$(\text{NH}_4)_6 \cdot \text{W}_{12}\text{O}_{39} \cdot x\text{H}_2\text{O}$	Ammonium tungsten oxide hydrate (Ammonium metatungstate hydrate)
<b>Ag</b>	$\text{AgNO}_3$	Silver nitrate
<b>Mo</b>	$(\text{NH}_4)_6\text{MO}_7 \cdot \text{O}_{24}4\text{H}_2\text{O}$	Ammonium molybdate tetrahydrate

**Table 7.** Ionic radii of elements used in the current study, in an octahedrally coordinated oxygen environment.

<b>Ion</b>	<b>Charge</b>	<b>Ionic Radius (Å)</b>	<b>Ion</b>	<b>Charge</b>	<b>Ionic Radius (Å)</b>
<b>Li</b>	1	0.76		1	1.15
<b>Ni</b>	2	0.69	<b>Ag</b>	2	0.94
	3	0.6		3	0.75
<b>Mn</b>	2	0.83	<b>Cu</b>	1	0.77
	3	0.645		2	0.73
	4	0.53	<b>Y</b>	3	0.9
	7	0.46		2	0.79
<b>Co</b>	2	0.745	<b>V</b>	3	0.64
	3	0.61		4	0.58
	4	0.53		5	0.54
<b>Mo</b>	3	0.69	<b>Fe</b>	2	0.78
	4	0.65		3	0.645
	5	0.61		4	0.585
	6	0.59		2	0.8
<b>W</b>	4	0.66	<b>Cr</b>	3	0.615
	5	0.62		5	0.49
	6	0.6		6	0.44

Here, half of the doping elements could not be used in the study since they caused a secondary phase formation when doped to NMC cathode produced via spray pyrolysis. W, Mo, Ag, and Cu were successfully doped into NMC cathode materials. XRD patterns of doped NMC are given in Figure 37.

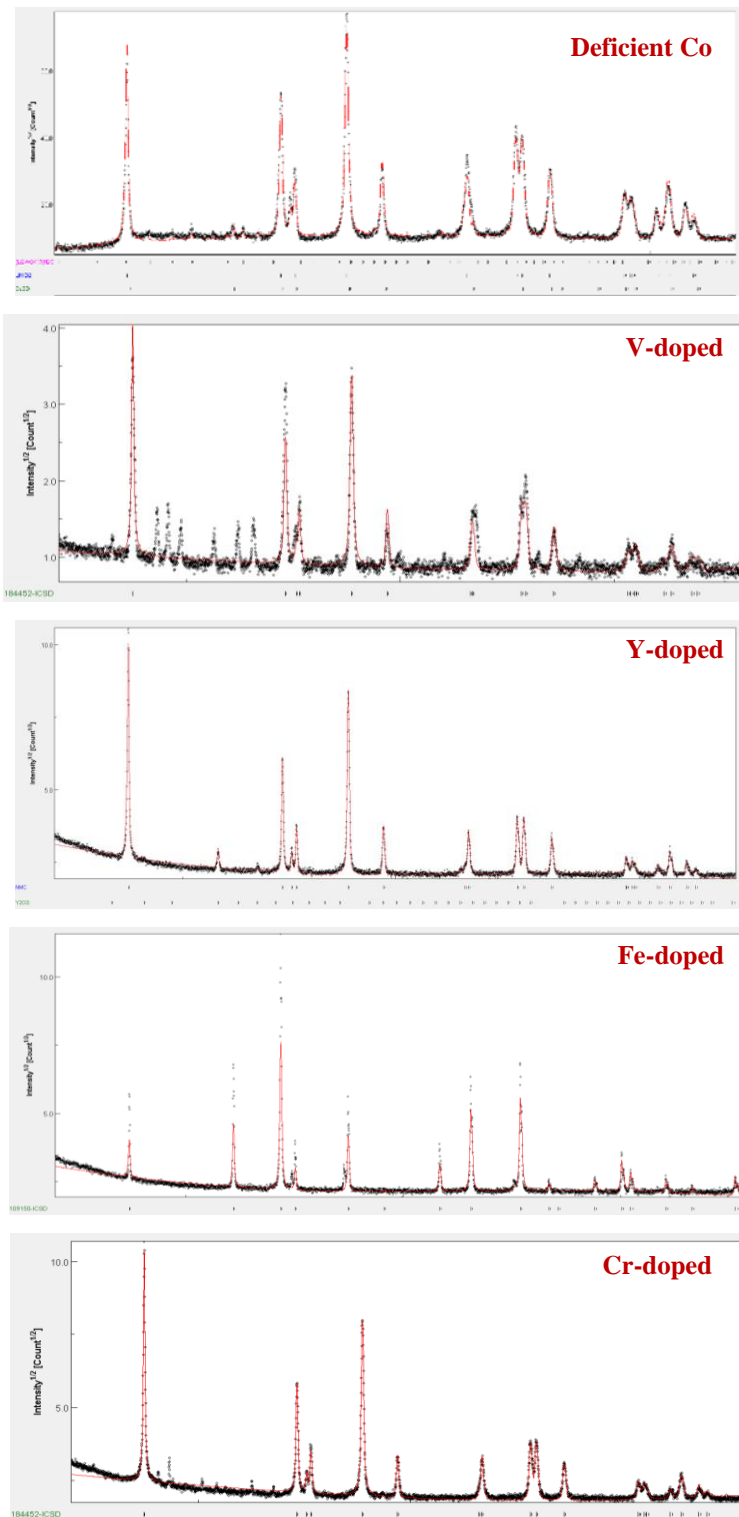


**Figure 37.** XRD pattern of NMC-111 doped with selected elements yielding secondary phases.

## 4.2 Structural Characterization Results

### 4.2.1 NMC Cathode materials

X-Ray diffraction patterns of NMC-111, NMC-622, NMC-226 and NMC-262 materials, after the post heat-treatment at 800 °C for 20h, are shown in Figure 38. Here, undoped NMC compositions exhibited well-defined splitting of (006)/(102) and (108)/(110) indicating layered structure and a good hexagonal ordering. The desired layer structure was obtained in all compositions, except NMC-262 which also comprised  $\text{Li}_{1.32}\text{Mn}_{1.68}\text{O}_4$  and  $\text{Li}_2\text{MnO}_3$  phases, Figure 38 d. The weight fraction of the layered phase in this composition was calculated as  $\sim 0.5$ . Therefore, NMC-262 was not used for further studies because of the difficulties and instability problems encountered during production via spray pyrolysis. Thus, NMC-111, NMC-622 and NMC-226 and doped NMC active materials were selected for further studies.

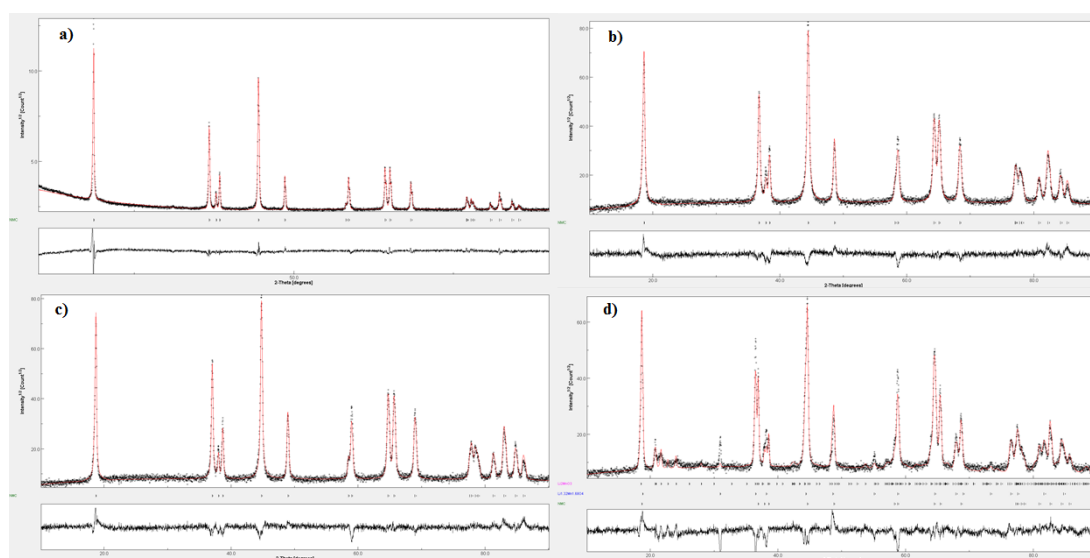


**Figure 38.** XRD patterns refined of a) NMC-111, b) NMC-622, c) NMC-226 and d) NMC-262.

The structure parameters and oxygen positions refined for undoped NMC cathode materials were summarized in Table 8. It should be noted that the better electrochemical performance was generally attributed to larger  $c$  lattice parameter for layered structures in literature. However, from lithium ion diffusion point of view, the size of the gap between the transition metal and oxygen layers is another important parameter so as to attain a good electrochemical performance [17]. The determined gap sizes are 2.1402 Å, 2.2998 Å, 2.2574 Å and 2.2257 Å for NMC-111, NMC-622, NMC-226 and NMC-262 active materials, respectively.

**Table 8.** Lattice parameters and oxygen positions refined of NMC cathode materials.

Sample	a (Å)	c (Å)	c/a	%R <sub>w</sub>	I <sub>[003]</sub> /I <sub>[104]</sub>	Oxygen Parameter (z)	Li-Gap (Å)
<b>111</b>	2.865	14.262	4.978	7.586	1.7984	0.2583	2.1402
<b>622</b>	2.864	14.262	4.980	14.827	0.6339	0.2527	2.2998
<b>226</b>	2.842	14.192	4.993	15.647	0.7373	0.2538	2.2574
<b>262</b>	2.852	14.243	4.994	21.371	0.7848	0.2552	2.2257

The morphology of each active material was examined via SEM and the representative images are given in Figure 39. Here, the typical morphology was in the form of spherical aggregates consisting of primary small particles. The average size of primary particles in undoped NMC was ranging from 0.2 μm to 0.6 μm.

TEM studies were carried for detailed structural analysis and the typical images for NMC-111, NMC-622, and NMC-226, respectively are given in Figure 40-42. The average particle size in NMC active materials was observed as ~200 nm. High resolution images for the active materials indicated the formation of the layered crystal structure. This was also confirmed by selected area diffraction patterns (SAED), Figure 40-42.

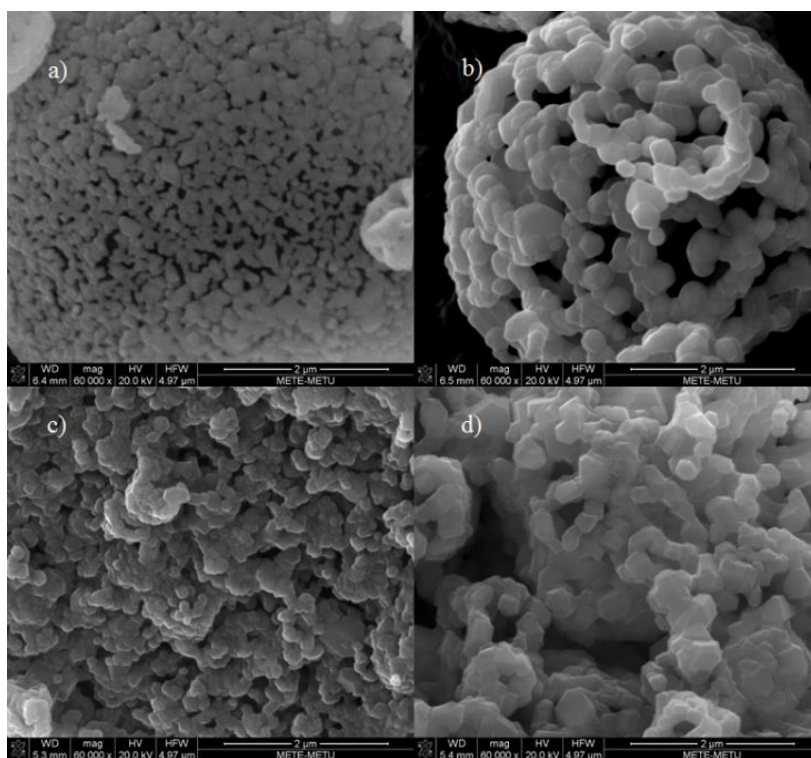


**Figure 39.** SEM images of a) NMC-111, b) NMC-622, c) NMC-226 and d) NMC-262 active materials.

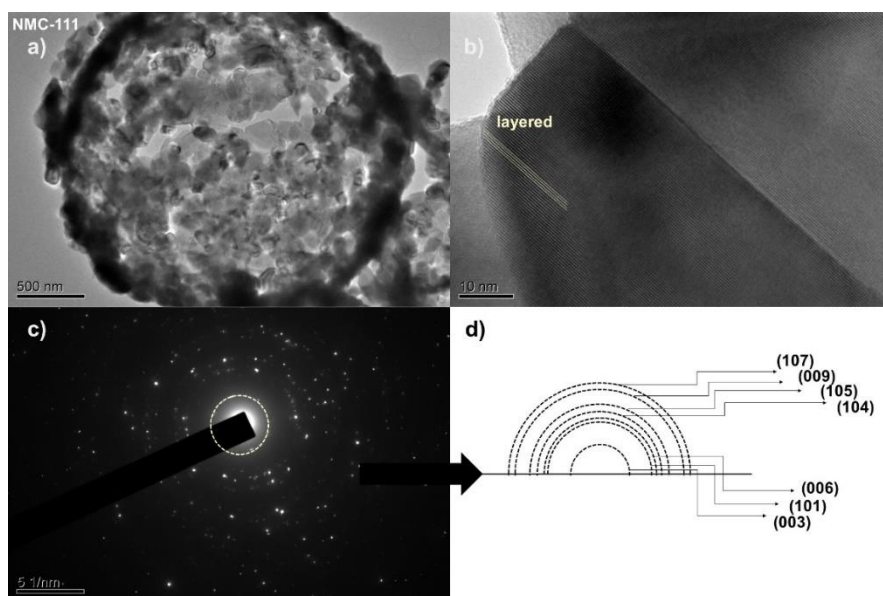


**Figure 40.** a) BF and b) HR images of NMC-111 cathode. c) SAED pattern of NMC-111, d) which was successfully indexed to  $R\bar{3}m$ .

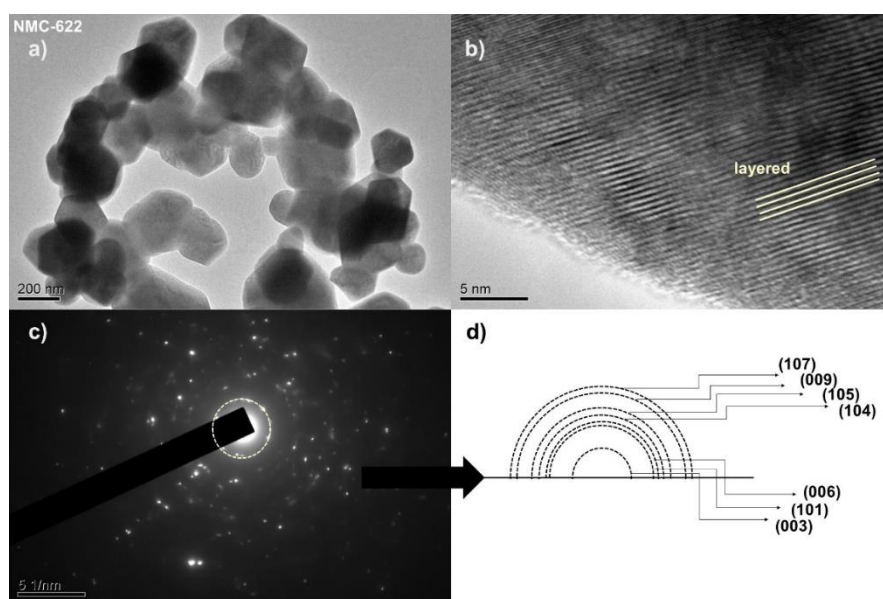


**Figure 41.** a) BF and b) HR images of NMC-622 cathode. c) SAED pattern of NMC-111, d) which was successfully indexed to  $R\bar{3}m$ .

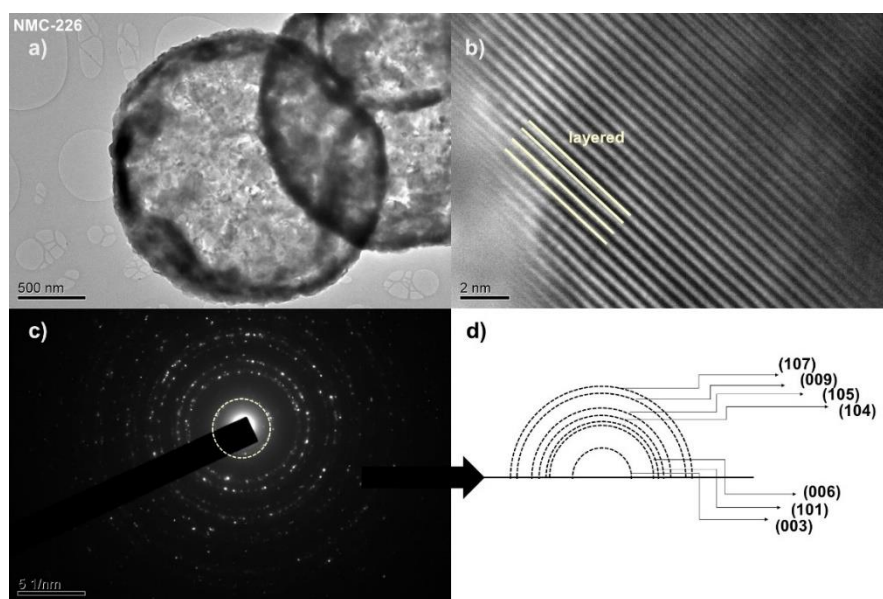


**Figure 42.** a) BF and b) HR images of NMC-226 cathode. c) SAED pattern of NMC-111, d) which was successfully indexed to  $R\bar{3}m$ .

#### 4.2.2 Doped NMC cathode materials

X-Ray diffraction patterns of Mo-W-Ag and Cu-doped NMC-111, NMC-226 and NMC-622 cathode materials, after the post heat-treatment at 800 °C for 20h, are given Figure 43-46. It was observed that the doped NMC active materials were phase-pure and exhibited a high crystallinity following 20h of heat treatment.

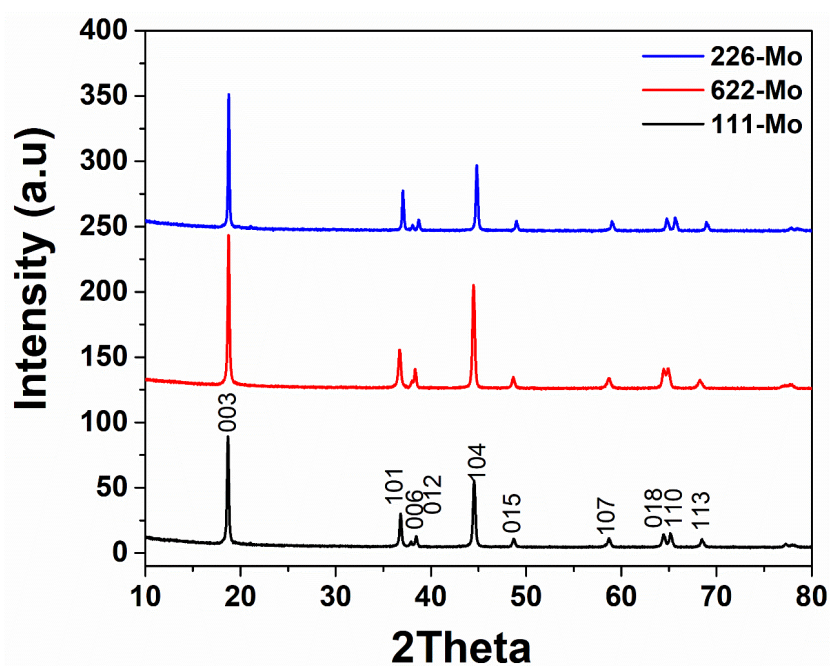


**Figure 43.** XRD patterns of Mo-doped NMC-111, NMC-226, and NMC-622 heat-treated at 800 °C for 20h.

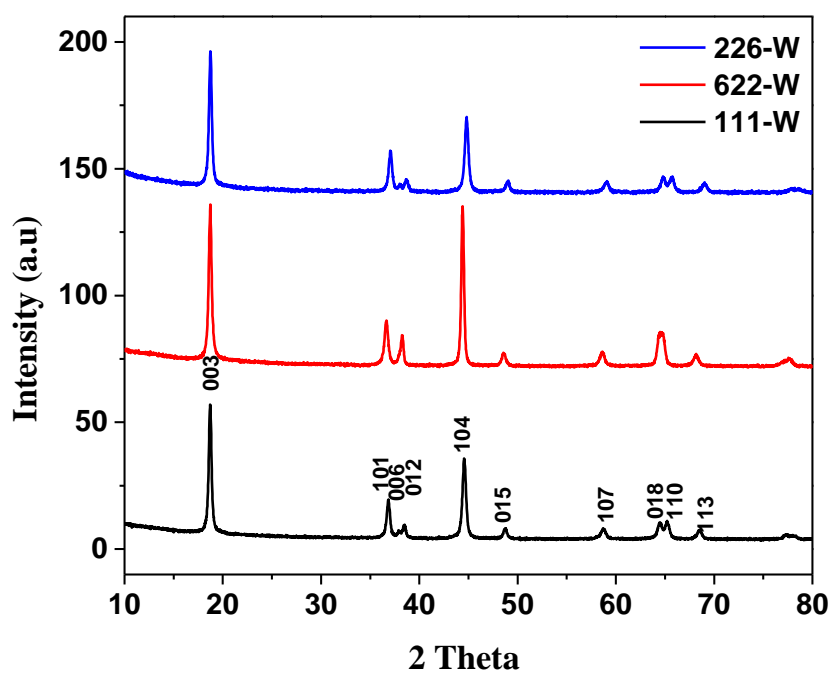


**Figure 44.** XRD patterns of W-doped NMC-111, NMC-226, and NMC-622 heat-treated at 800 °C for 20h.

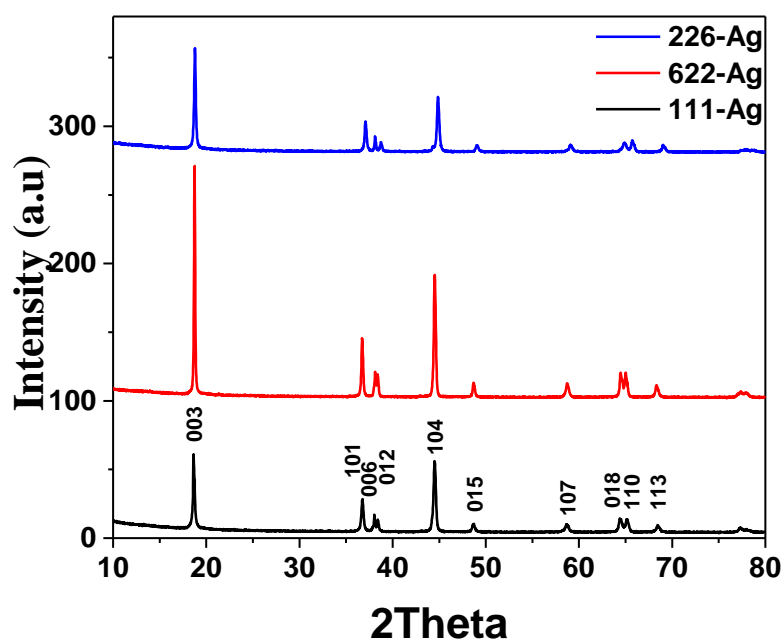


**Figure 45.** XRD patterns of Ag-doped NMC-111, NMC-226, and NMC-622 heat-treated at 800 °C for 20h.

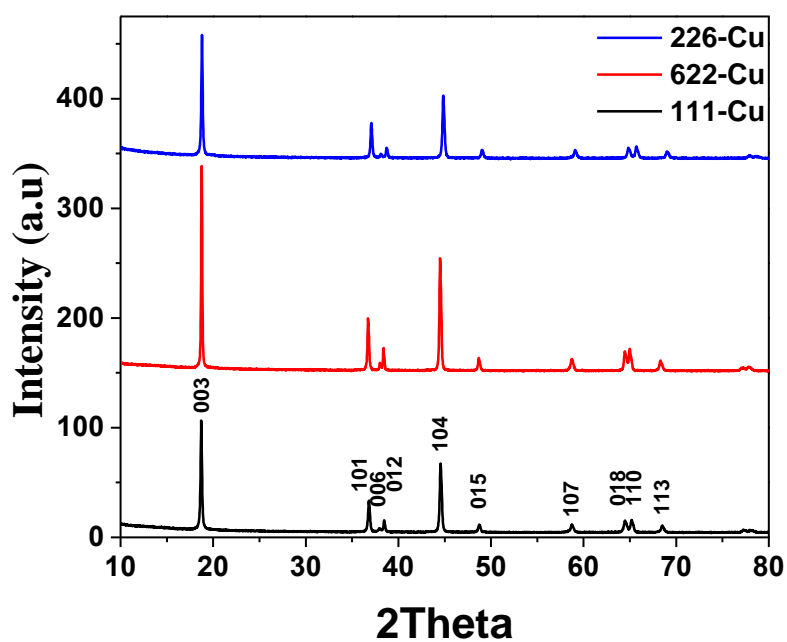


**Figure 46.** XRD patterns of Cu-doped NMC-111, NMC-226, and NMC-622 heat-treated at 800 °C for 20h.

The oxygen position and structural parameters refined by Rietveld analysis are summarized in Table 9. Here, many of the active materials, following the heat-treatment at 800 °C for 20h, exhibited  $I_{[003]}/I_{[104]}$  ratio higher than 1.2, indicating a good structure ordering and negligible cation mixing [98]. However, this was not achieved in the case of 622-W, 111-Ag, and 111-W cathode materials.

**Table 9.** Refined lattice parameters and oxygen positions of doped NMC layered cathode materials.

<b>Notation (NMC)</b>	<b>a (Å)</b>	<b>c (Å)</b>	<b>c/a</b>	<b>% R<sub>w</sub></b>	<b>I<sub>[003]</sub>/I<sub>[104]</sub></b>	<b>Oxygen Parameter (z)</b>	<b>Li- Gap (Å)</b>
<b>111-Mo</b>	2.864	14.246	4.975	7.027	1.608	0.2610	2.0609
<b>622-Mo</b>	2.875	14.228	4.948	5.874	1.460	0.2585	2.1302
<b>226-Mo</b>	2.844	14.187	4.988	5.673	1.417	0.2602	2.0748
<b>111-W</b>	2.865	14.253	4.975	5.743	1.197	0.2691	1.8301
<b>622-W</b>	2.876	14.188	4.953	6.781	1.011	0.2594	2.0954
<b>226-W</b>	2.844	14.188	4.989	4.503	1.690	0.2874	1.3042
<b>111-Ag</b>	2.862	14.226	4.970	8.249	1.014	0.2779	1.5772
<b>622-Ag</b>	2.870	14.211	4.951	9.082	1.833	0.2582	2.1358
<b>226-Ag</b>	2.844	14.172	4.983	6.489	1.762	0.2597	2.0872
<b>111-Cu</b>	2.864	14.235	4.971	6.975	1.578	0.2578	2.1504
<b>622-Cu</b>	2.872	14.220	4.952	8.013	1.777	0.2578	2.1482
<b>226-Cu</b>	2.843	14.172	4.9858	5.859	1.852	0.2589	2.1105

Doped cathode materials were also investigated via SEM and the respective images are given in Figure 47-50. Similar to undoped equivalents, the typical morphology in NMC cathode materials was in the form of spherical aggregates consisting of equiaxed primary particles.

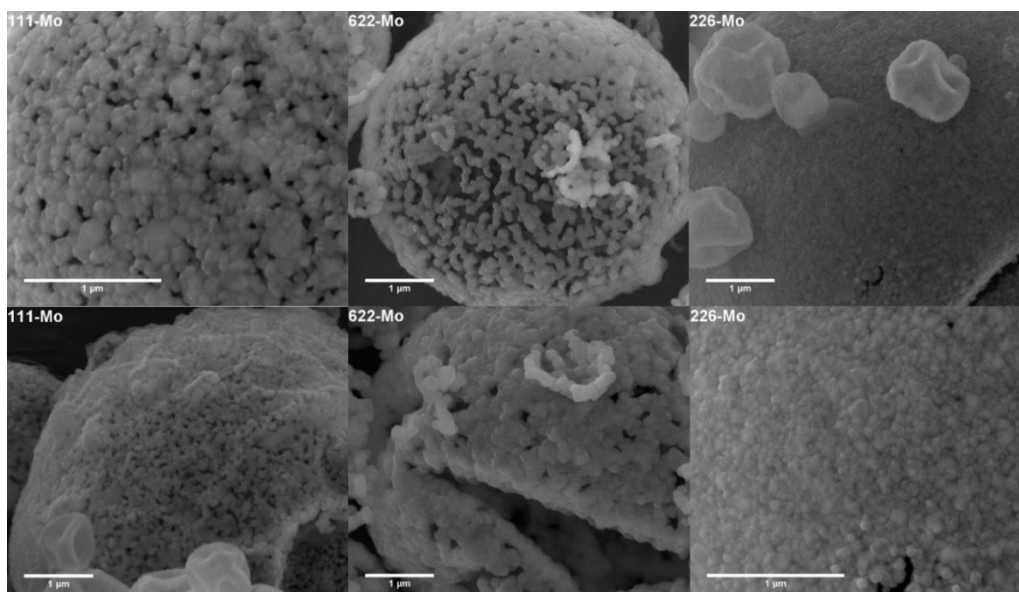


**Figure 47.** SEM images of Mo-doped NMC-111, NMC-622, and NMC-226 cathode materials.

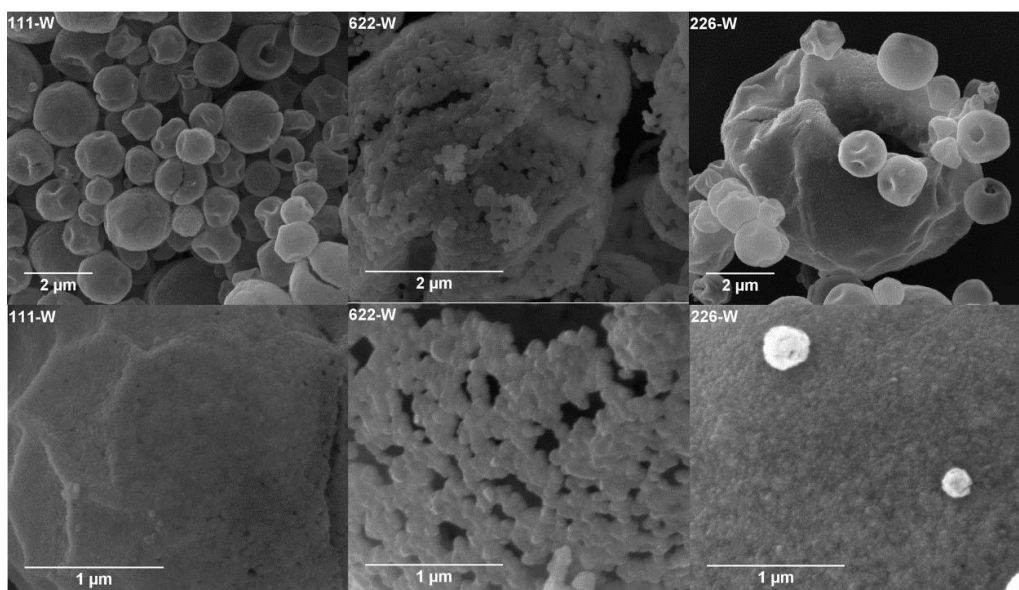


**Figure 48.** SEM images of W-doped NMC-111, NMC-622, and NMC-226 cathode materials.

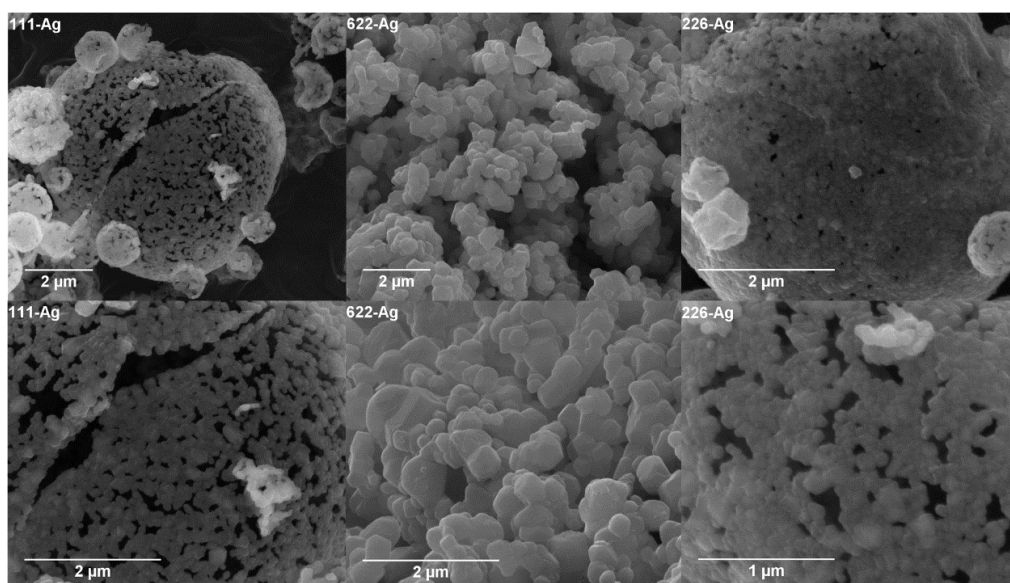


**Figure 49.** SEM images of Ag-doped NMC-111, NMC-622, and NMC-226 cathode materials.

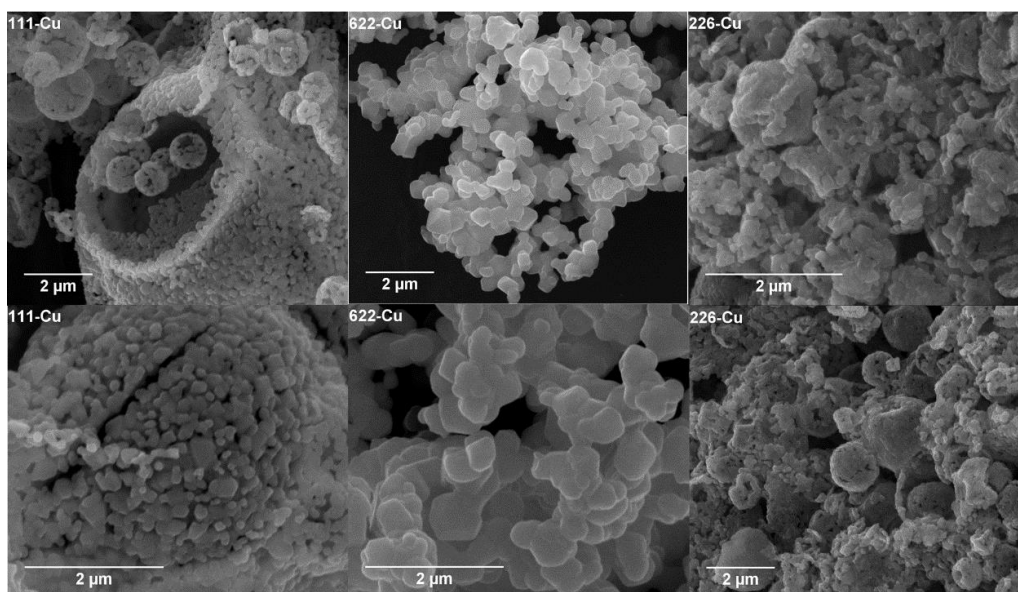


**Figure 50.** SEM images of Cu-doped NMC-111, NMC-622, and NMC-226 cathode materials.

Doped NMC cathode materials were further investigated by TEM. Typical images and the SAED patterns for doped NMC cathode materials are given in Figure 51-62. SAED patterns were in a good agreement with the XRD patterns indicating the presence of layered structure for all doped cathode materials.

BF images of doped NMC cathode materials have shown that the content of transition metals had a greater effect on the particle morphology as compared to doping elements. NMC-111 cathode materials exhibited a morphology which was typically in the form of spherical aggregates consisting of small primary particles. This was valid for all doping elements in NMC-111. NMC-226 cathode materials showed a similar morphology with NMC-111 cathode materials and it was also independent of the doping elements. There were only slight deviations with respect to the size of the primary particles and the porosity of the aggregates between NMC-111 and NMC-226 cathode materials. On the other hand, NMC-622 cathode materials exhibited very different morphology as compared the other cathode materials having different content of transition metals. Although NMC-622 cathode materials also comprised spherical aggregates, they had also some fragmented particles which were smaller in size. This different type of particle formation was observed in all NMC cathode materials independent from doping elements and even in undoped compositions. Thus, this could be attributed to the effect of higher Ni content in the structure.

TEM studies also revealed that there were different atomic arrangements at the surface of the cathode materials, especially in Ni-rich NMC compounds. It is known that surface of NMC cathode materials are metastable and have a tendency to form surface reconstruction layers (SRL). These layers can be defined as loose atomic layers [63,146,147], and primarily occurs along the Li-ion diffusion direction [148]. The reconstruction of layers often results in the formation of disordered structure or a structural transformation from  $R\bar{3}m$  layered structure to  $Fm\bar{3}m$  rock-salt or

$Fd\bar{3}m$  spinel structure. The transformation takes place when the cathode interacts with the electrolyte, particularly at high-voltage cycling. This leads to capacity fading and impedance build-up in the structure [63,146].

It should be mentioned that pristine Ni could also segregate on the surface (PNS), which is very similar to the formation of SRL. Therefore, it is not easy to distinguish the difference between them [148]. The formation of surface reconstruction layers in Ni-rich compounds in the study might be also attributed to Ni segregation.

Interestingly, the similar surface reconstruction layer was observed in cathode materials before the charge/discharge cycles, Figure 53 b. The surface reconstruction observed in this cathode materials was in the form of surface disordering instead of a structural transformation, Figure 53 d. This could be attributed to the disordered occupation of transition metal atoms into the atomic sites.

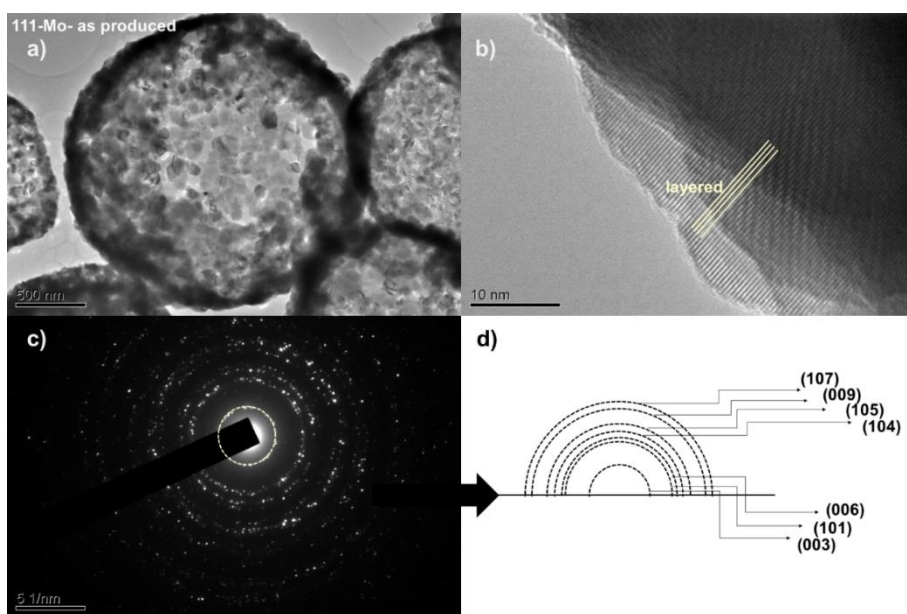


**Figure 51.** a) BF and b) HR images of the Mo-doped NMC-111 cathode. c) Respective SAED pattern, d) which was successfully indexed to  $R\bar{3}m$ .

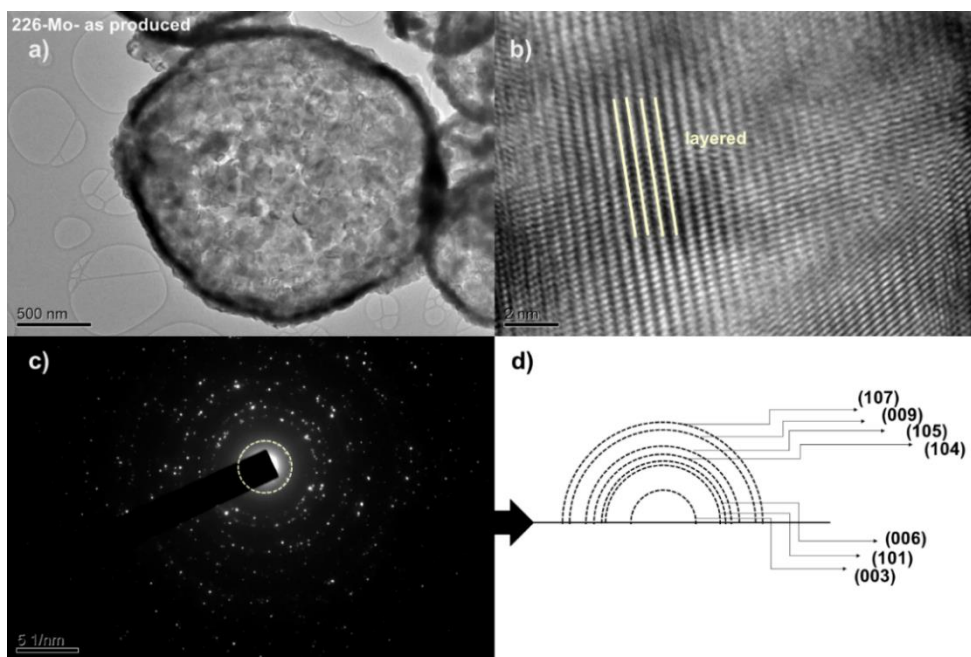


**Figure 52.** a) BF and b) HR images of the Mo-doped NMC-226 cathode. c) Respective SAED pattern, d) which was successfully indexed to  $R\bar{3}m$ .

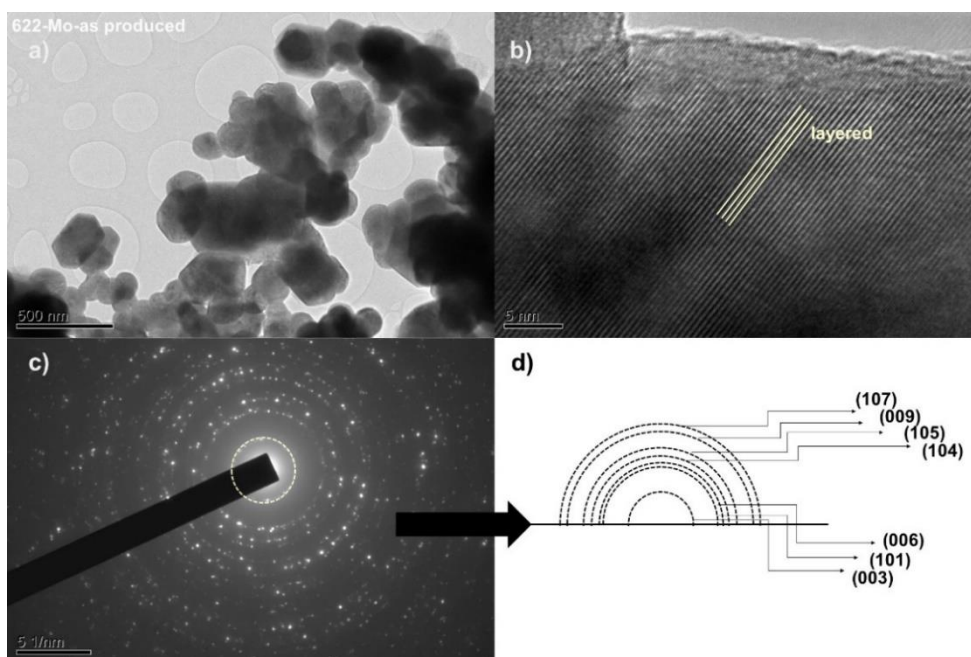


**Figure 53.** a) BF and b) HR images of the Mo-doped NMC-622 cathode. c) Respective SAED pattern, d) which was successfully indexed to  $R\bar{3}m$ .

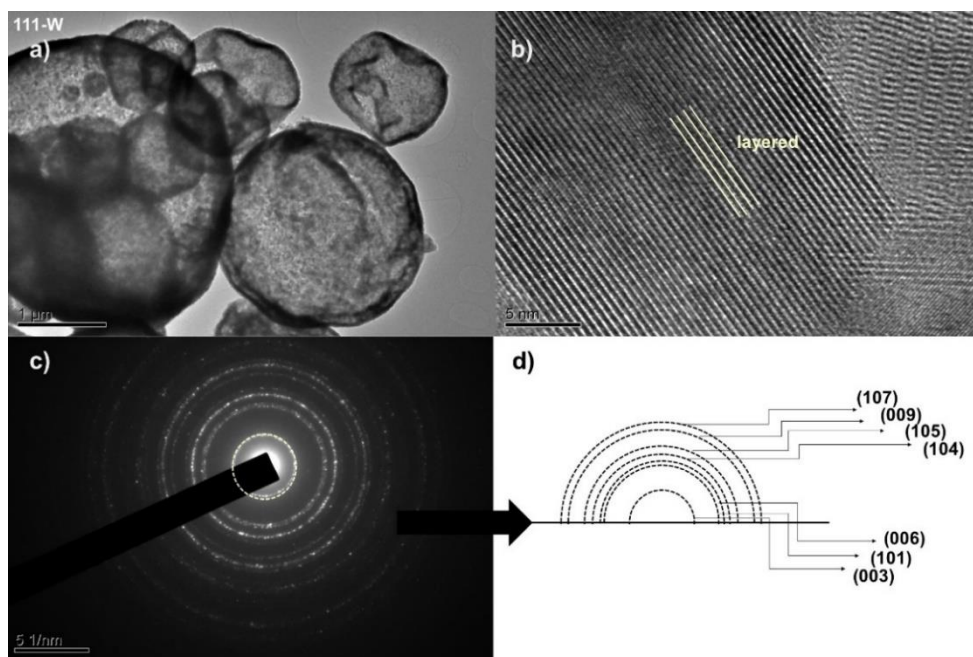


**Figure 54.** a) BF and b) HR images of the W-doped NMC-111 cathode. c) Respective SAED pattern, d) which was successfully indexed to  $R\bar{3}m$ .

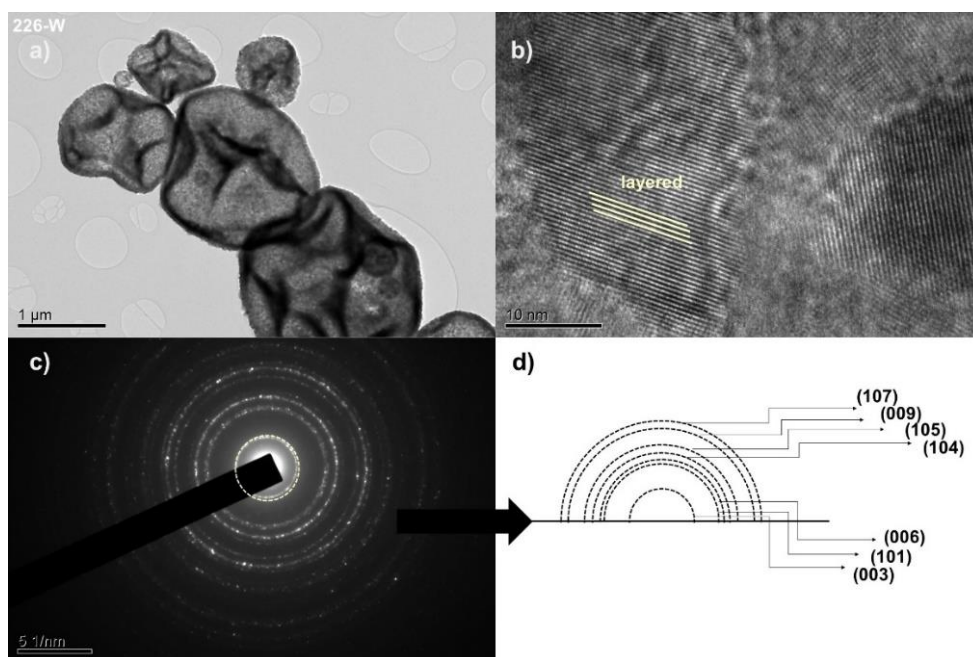


**Figure 55.** a) BF and b) HR images of W-doped NMC-226 cathode. c) Respective SAED pattern, d) which was successfully indexed to  $R\bar{3}m$ .

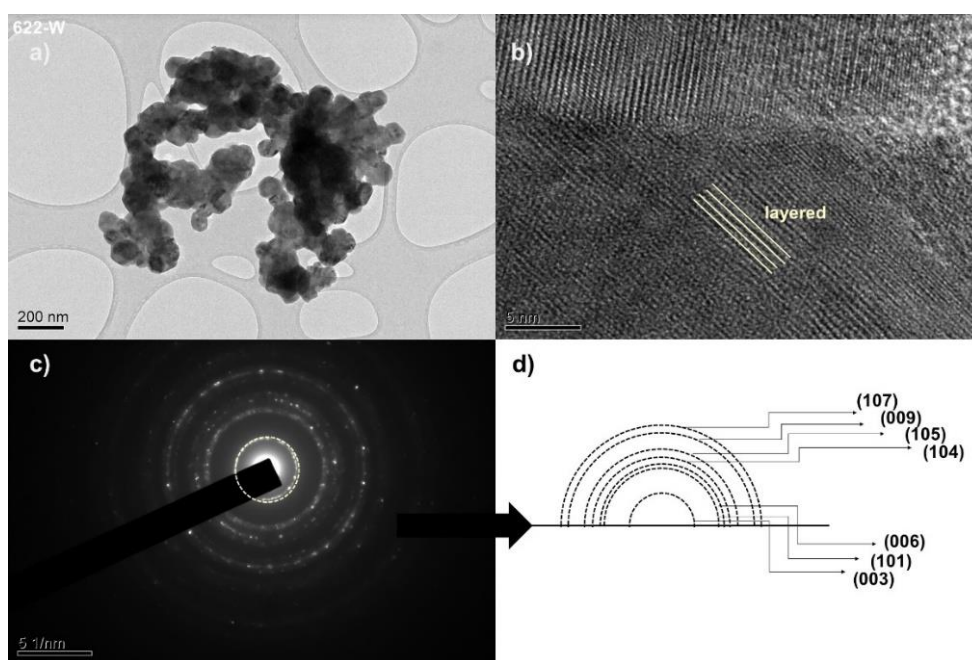


**Figure 56.** a) BF and b) HR images of the W-doped NMC-622 cathode. c) Respective SAED pattern, d) which was successfully indexed to  $R\bar{3}m$ .

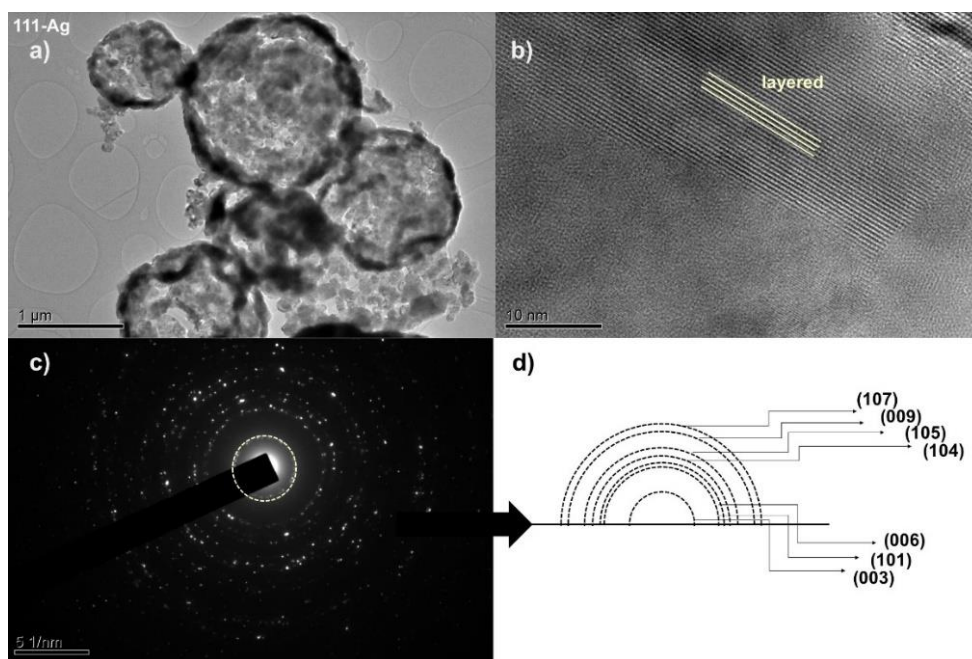


**Figure 57.** a) BF and b) HR images of the Ag-doped NMC-111 cathode. c) Respective SAED pattern, d) which was successfully indexed to  $R\bar{3}m$ .

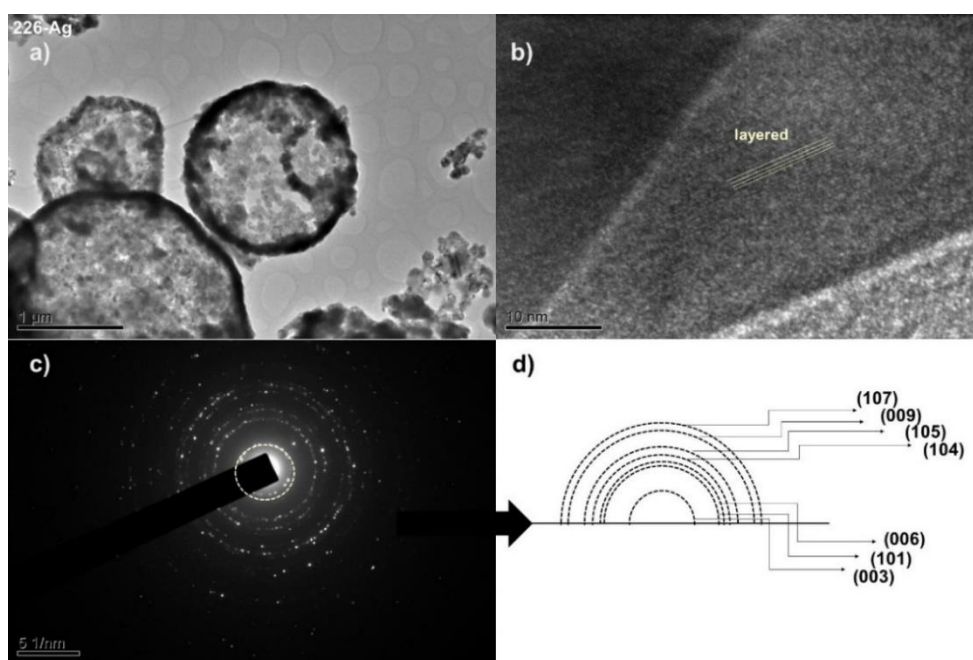


**Figure 58.** a) BF and b) HR images of the Ag-doped NMC-226 cathode. c) SAED pattern of NMC-111, d) which was successfully indexed to  $R\bar{3}m$ .

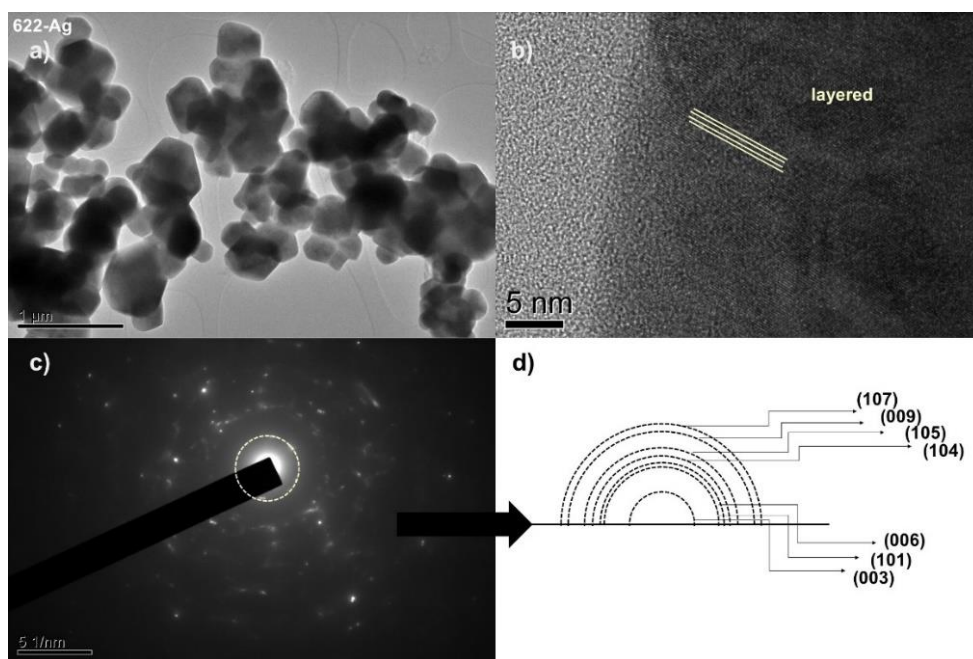


**Figure 59.** a) BF and b) HR images of the W-doped NMC-622 cathode. c) Respective SAED pattern, d) which was successfully indexed to  $R\bar{3}m$ .

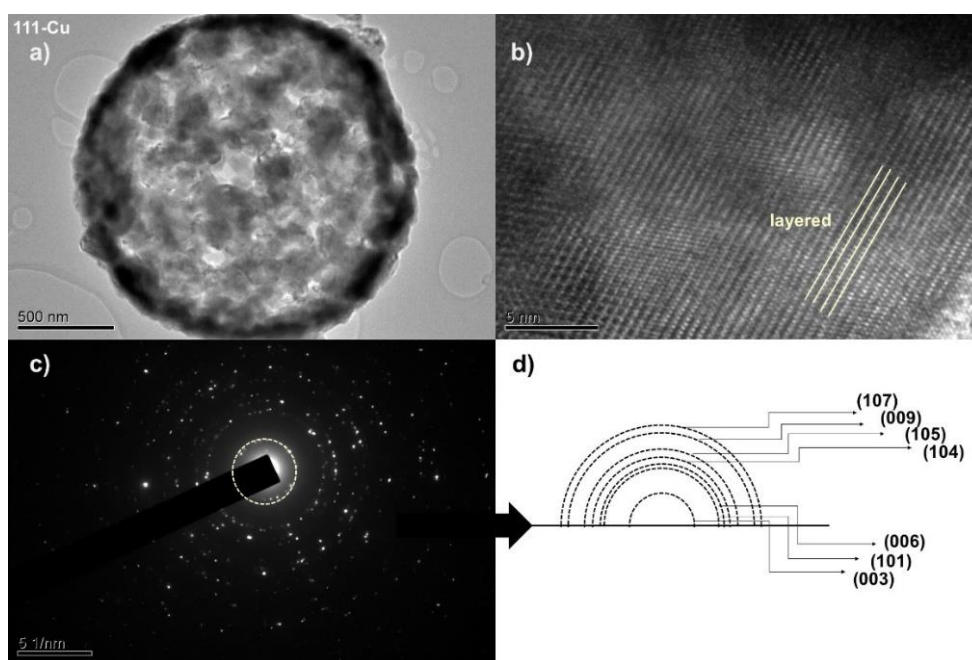


**Figure 60.** a) BF and b) HR images of the Cu-doped NMC-111 cathode. c) Respective SAED pattern, d) which was successfully indexed to  $R\bar{3}m$ .

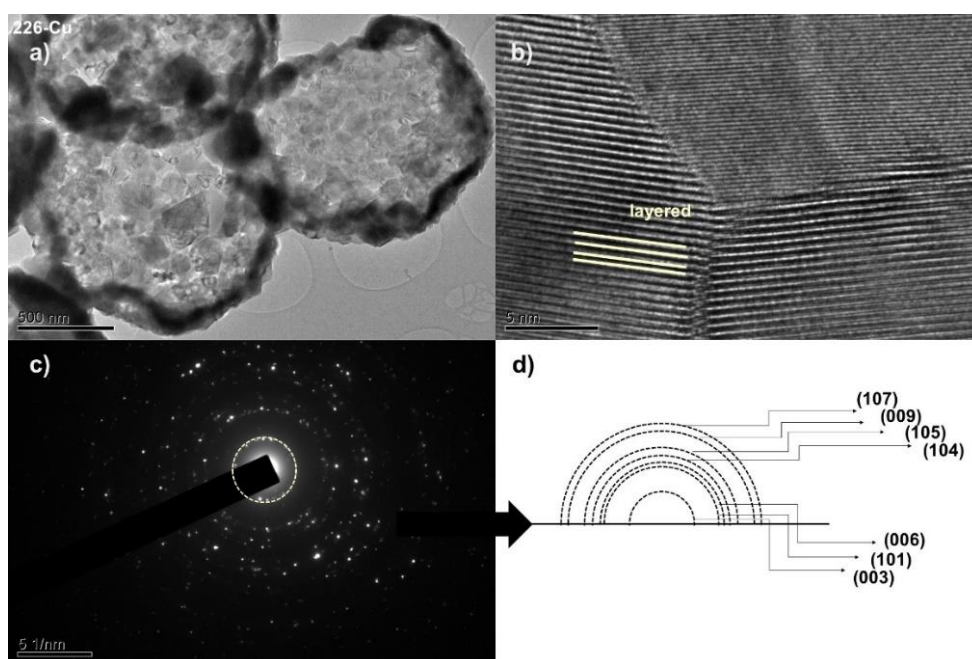


**Figure 61.** a) BF and b) HR images of the Cu-doped NMC-226 cathode. c) Respective SAED pattern, d) which was successfully indexed to  $R\bar{3}m$ .

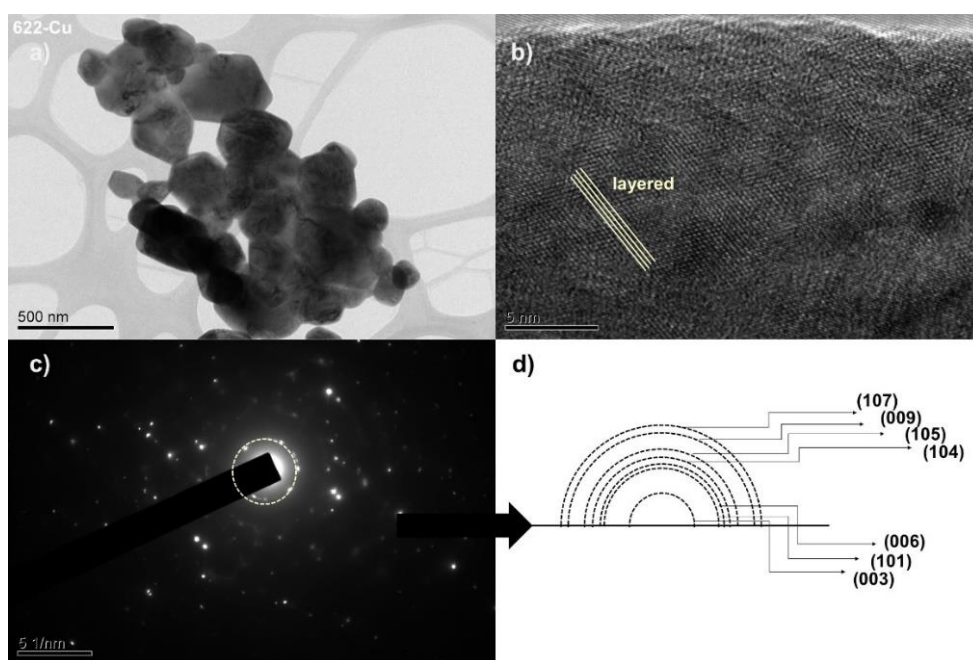


**Figure 62.** a) BF and b) HR images of the Cu-doped NMC-622 cathode. c) Respective SAED pattern, d) which was successfully indexed to  $R\bar{3}m$ .

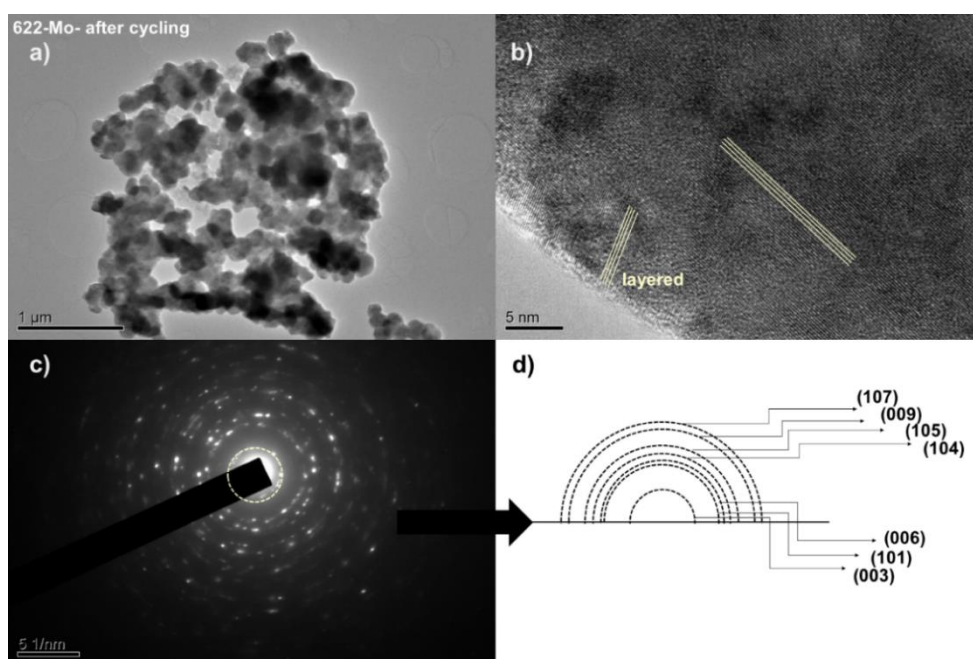


**Figure 63.** a) BF and b) HR images of Mo-doped NMC-622 cathode after cycling. c) Respective SAED pattern, d) which was successfully indexed to  $R\bar{3}m$ .

Following the charge/discharge cycles, cathode materials were also investigated via TEM. As an example, TEM images and SAED pattern of Mo-doped NMC-622 after 20 charge/discharge cycles are given in Figure 63. It was observed that Mo-doped NMC-622 preserved its layered structure without formation of a secondary phase after 20 charge/discharge cycles. Thus, it can be deduced that Mo doping was successful to stabilize NMC structure and to prevent irreversible phase transformation during cycling. This might be due to the hindering of Ni<sup>2+</sup> ions migration in the presence of Mo doping, where the ion migration is critical for structural transformation [99].

### 4.3 Chemical Characterization Results

#### 4.3.1 NMC Cathode materials

The compositions of the undoped active materials were determined using both EDS and ICP-MS and compared with the targeted compositions. EDS was employed so as to determine the content of the transition metals in the cathode materials. The location of the compositions with respect to their transition metals content on the ternary diagram is given Figure 64.

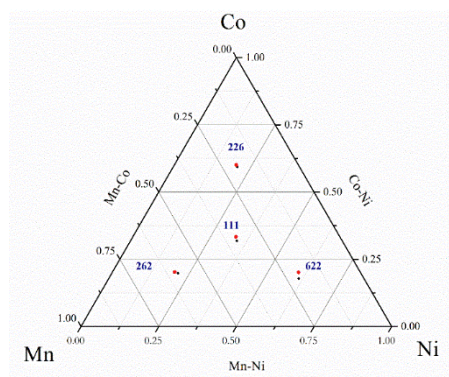


**Figure 64.** Comparison of the transition metals content determined by EDS (black marks) and the values targeted (red marks) for NMC-111, NMC-622, NMC-226, and NMC-262.

The compositions determined with the accuracy of EDS,  $\pm 2\%$ , were very similar to the values targeted. The active materials were also analyzed by ICP-MS in order to determine the Li content and to ensure the transition metals content in the cathode materials.

XPS was employed so as to determine the oxidation states of transition metals and Li in the cathode materials. XPS spectrum of Li1s, Ni2p, Mn2p, Mn3s and Co2p, O1s and C1s for 111, 622 and 226 NMC cathode materials are given in Figure 65. Here, the signals at  $\sim 283$  eV and  $\sim 287$  eV in C1s indicated the presence of impurities on the surface of active materials. These are commonly associated with C—O and O—C=O, respectively [149]. O1s spectrum indicated the presence of metal oxides for all NMC cathode materials. However, the signal at  $\sim 529$  eV indicated that the formation of metal carbonates, probably  $\text{Li}_2\text{CO}_3$  [150], in 622 and 226 NMC cathode materials. In Li1s spectra, the peak at 52 eV indicated  $\text{Li}^{+1}$  which was the same for all cathode materials. Here, the peaks at 59 eV and 66 eV coincided with that of Co3p and Ni3p, respectively [151]. Mn3s spectra were scanned to direct identification of Mn oxidation state in all active cathode materials, Figure 65. Here, Mn3s peaks had two multiplet split components in all cathode materials. It is known that the magnitude of splitting,  $\Delta E$ , in Mn3s spectrum can be used to determine the oxidation state of Mn [152]. In all compositions,  $\Delta E$  was measured  $\sim 6.00$  eV indicating the presence of  $\text{Mn}^{2+}$  [152,153]. The position of Co2p $_{3/2}$ , Co2p $_{1/2}$  at 793 eV and 778 eV, respectively indicated the presence of  $\text{Co}^{3+}$ , while Ni2p $_{3/2}$ , Ni2p $_{1/2}$  peaks observed at 870 eV and 853 eV, respectively indicated the presence of and  $\text{Ni}^{2+}$  in all active materials. [153,154].

### Undoped NMC cathode materials

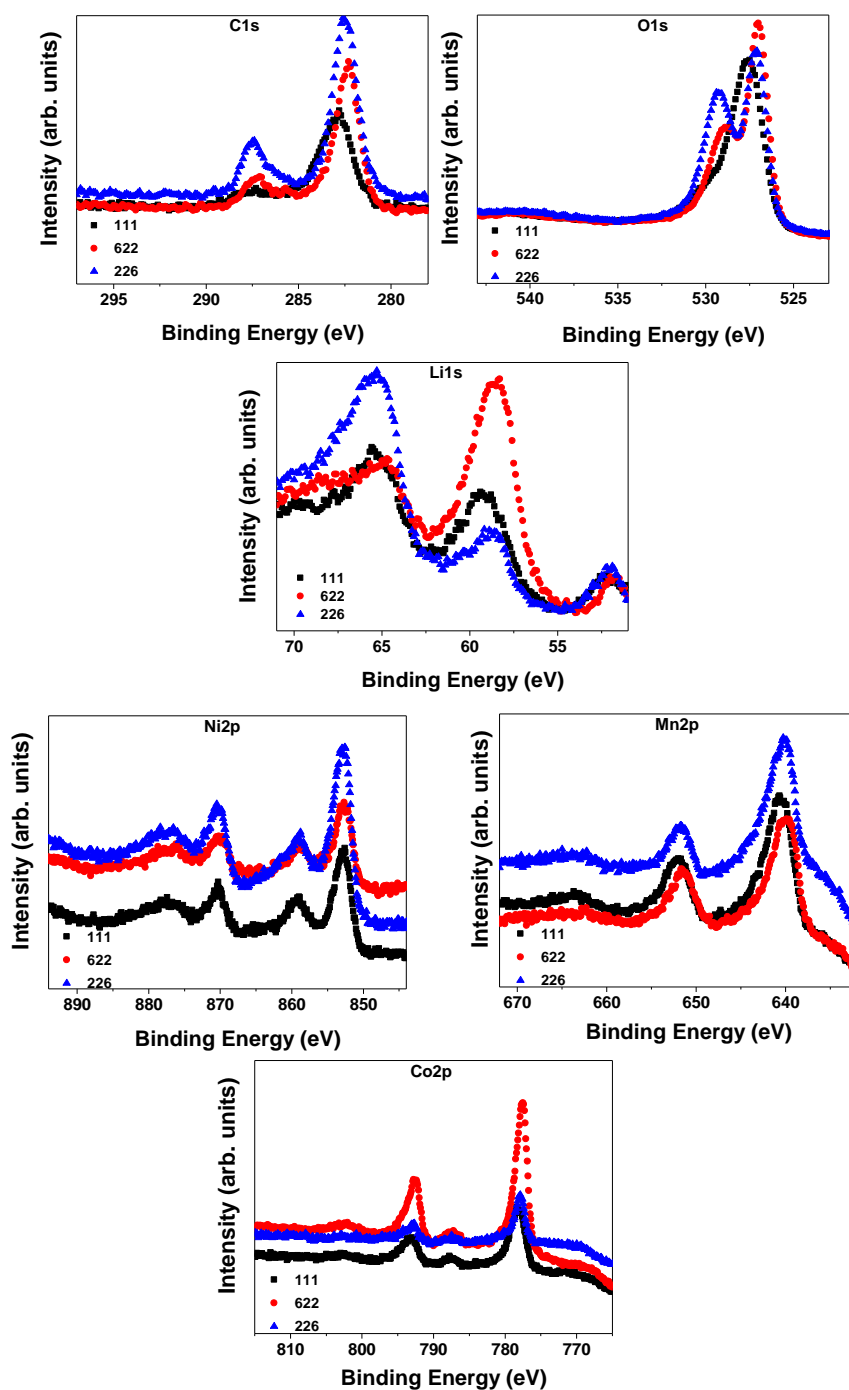


**Figure 65.** XPS tight-scans of C1s, O1s, Li1s, Ni2p, Mn2p, Mn3s and Co2 for undoped 111, 622, and 226 NMC cathode materials.

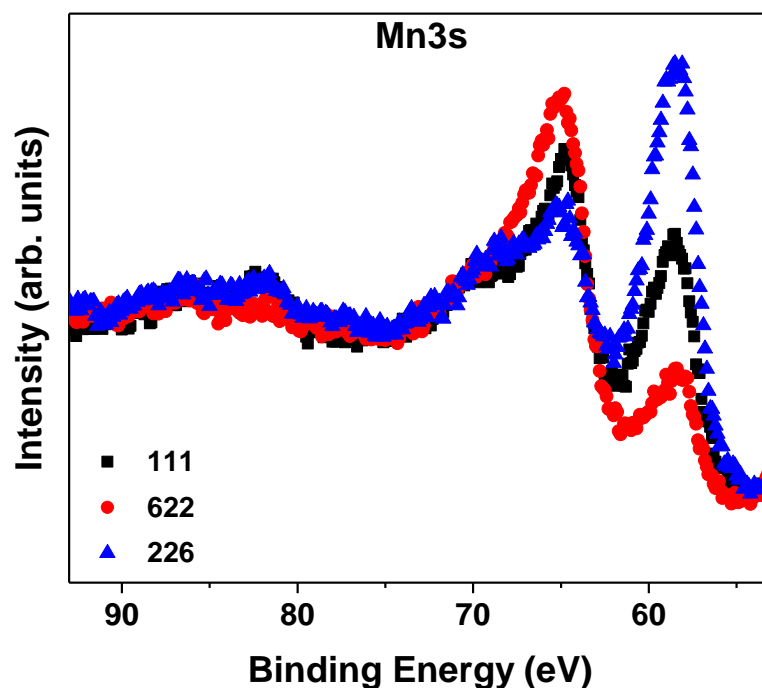


**Figure 65.** Cont' d

### 4.3.2 Doped NMC

The compositions of doped NMC cathode materials were determined using weight percentages of elements measured with ICP-MS, Table 10. The measurements showed a good agreement between the intended and the determined compositions.

Oxidation states were also determined for doped NMC cathode materials. XPS spectrum of O1s, C1s, Li1s, Ni2p, Mn2p, Mn3s, Co2p, Mo3d, W4f, Ag3d and CuLMM for all doped active materials, i.e. NMC-111, NMC-622, and NMC-226 are given in Figure 66-68. In C1s spectra, similar to undoped cathode materials, the peaks at ~283 eV and ~287 eV were associated with C–O and O–C=O, respectively [149]. O1s spectrum indicated the presence of metal oxide and metal carbonate, probably Li<sub>2</sub>CO<sub>3</sub>, which was between 527-529 eV [150]. The peak around 529-530 eV was generally associated with C–O. For Li1s spectra, the peaks at around 59 eV and 64

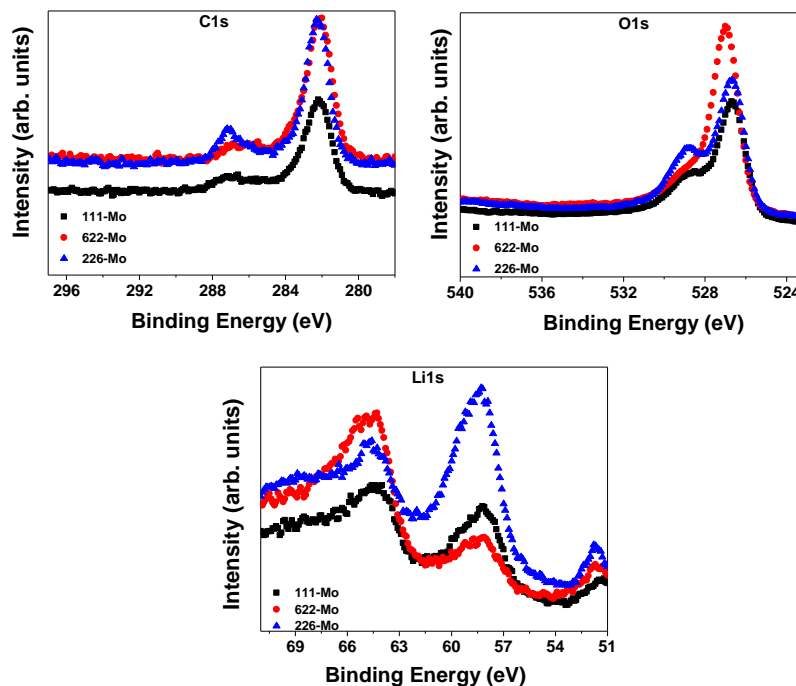
eV coincides with that of Co3p and Ni3p, respectively, where the peak around 52 eV belonged to standard Li1s peak for all samples [151].

Figure 67 shows the position of Co2p3/2, Co2p1/2, and Ni2p3/2, Ni2p1/2 peaks at ~792.4 eV, 777.3 eV and 869 eV, 852 eV, respectively. This implied the presence of Co<sup>3+</sup> and Ni<sup>2+</sup> [153,154] in all doped samples. Mn3s peaks were also used to identify of Mn oxidation state. Here, ΔE was measured as ~6.00 indicating the presence of Mn<sup>2+</sup> [152,153] for all doped active materials.

**Table 10.** Compositions of doped NMC layered cathode materials.

Notation (NMC)	Sample	Calculated formula
<b>111-Mo</b>	Li <sub>1.05</sub> (Ni <sub>0.323</sub> Mn <sub>0.323</sub> Co <sub>0.323</sub> Mo <sub>0.02</sub> )O <sub>2</sub>	Li <sub>0.984</sub> (Ni <sub>0.318</sub> Mn <sub>0.340</sub> Co <sub>0.337</sub> Mo <sub>0.019</sub> )O <sub>2±δ</sub>
<b>622-Mo</b>	Li <sub>1.05</sub> (Ni <sub>0.593</sub> Mn <sub>0.193</sub> Co <sub>0.193</sub> Mo <sub>0.02</sub> )O <sub>2</sub>	Li <sub>0.975</sub> (Ni <sub>0.606</sub> Mn <sub>0.199</sub> Co <sub>0.200</sub> Mo <sub>0.020</sub> )O <sub>2±δ</sub>
<b>226-Mo</b>	Li <sub>1.05</sub> (Ni <sub>0.193</sub> Mn <sub>0.193</sub> Co <sub>0.593</sub> Mo <sub>0.02</sub> )O <sub>2</sub>	Li <sub>0.974</sub> (Ni <sub>0.200</sub> Mn <sub>0.200</sub> Co <sub>0.625</sub> Mo <sub>0.019</sub> )O <sub>2±δ</sub>
<b>111-W</b>	Li <sub>1.05</sub> (Ni <sub>0.323</sub> Mn <sub>0.323</sub> Co <sub>0.323</sub> W <sub>0.02</sub> )O <sub>2</sub>	Li <sub>0.980</sub> (Ni <sub>0.328</sub> Mn <sub>0.328</sub> Co <sub>0.342</sub> W <sub>0.021</sub> )O <sub>2±δ</sub>
<b>622-W</b>	Li <sub>1.05</sub> (Ni <sub>0.593</sub> Mn <sub>0.193</sub> Co <sub>0.193</sub> W <sub>0.02</sub> )O <sub>2</sub>	Li <sub>0.948</sub> (Ni <sub>0.601</sub> Mn <sub>0.228</sub> Co <sub>0.202</sub> W <sub>0.019</sub> )O <sub>2±δ</sub>
<b>226-W</b>	Li <sub>1.05</sub> (Ni <sub>0.193</sub> Mn <sub>0.193</sub> Co <sub>0.593</sub> W <sub>0.02</sub> )O <sub>2</sub>	Li <sub>1.013</sub> (Ni <sub>0.194</sub> Mn <sub>0.194</sub> Co <sub>0.597</sub> W <sub>0.018</sub> )O <sub>2±δ</sub>
<b>111-Ag</b>	Li <sub>1.05</sub> (Ni <sub>0.323</sub> Mn <sub>0.323</sub> Co <sub>0.323</sub> Ag <sub>0.02</sub> )O <sub>2</sub>	Li <sub>0.972</sub> (Ni <sub>0.327</sub> Mn <sub>0.355</sub> Co <sub>0.336</sub> Ag <sub>0.009</sub> )O <sub>2±δ</sub>
<b>622-Ag</b>	Li <sub>1.05</sub> (Ni <sub>0.593</sub> Mn <sub>0.193</sub> Co <sub>0.193</sub> Ag <sub>0.02</sub> )O <sub>2</sub>	Li <sub>0.966</sub> (Ni <sub>0.616</sub> Mn <sub>0.206</sub> Co <sub>0.204</sub> Ag <sub>0.007</sub> )O <sub>2±δ</sub>
<b>226-Ag</b>	Li <sub>1.05</sub> (Ni <sub>0.193</sub> Mn <sub>0.193</sub> Co <sub>0.593</sub> Ag <sub>0.02</sub> )O <sub>2</sub>	Li <sub>0.965</sub> (Ni <sub>0.199</sub> Mn <sub>0.202</sub> Co <sub>0.623</sub> Ag <sub>0.01</sub> )O <sub>2±δ</sub>
<b>111-Cu</b>	Li <sub>1.05</sub> (Ni <sub>0.323</sub> Mn <sub>0.323</sub> Co <sub>0.323</sub> Cu <sub>0.02</sub> )O <sub>2</sub>	Li <sub>0.968</sub> (Ni <sub>0.337</sub> Mn <sub>0.337</sub> Co <sub>0.338</sub> Cu <sub>0.02</sub> )O <sub>2±δ</sub>
<b>622-Cu</b>	Li <sub>1.05</sub> (Ni <sub>0.593</sub> Mn <sub>0.193</sub> Co <sub>0.193</sub> Cu <sub>0.02</sub> )O <sub>2</sub>	Li <sub>0.932</sub> (Ni <sub>0.623</sub> Mn <sub>0.212</sub> Co <sub>0.211</sub> Cu <sub>0.022</sub> )O <sub>2±δ</sub>
<b>226-Cu</b>	Li <sub>1.05</sub> (Ni <sub>0.193</sub> Mn <sub>0.193</sub> Co <sub>0.593</sub> Cu <sub>0.02</sub> )O <sub>2</sub>	Li <sub>0.993</sub> (Ni <sub>0.192</sub> Mn <sub>0.194</sub> Co <sub>0.600</sub> Cu <sub>0.021</sub> )O <sub>2±δ</sub>

### Mo-doped NMC



### W-doped NMC

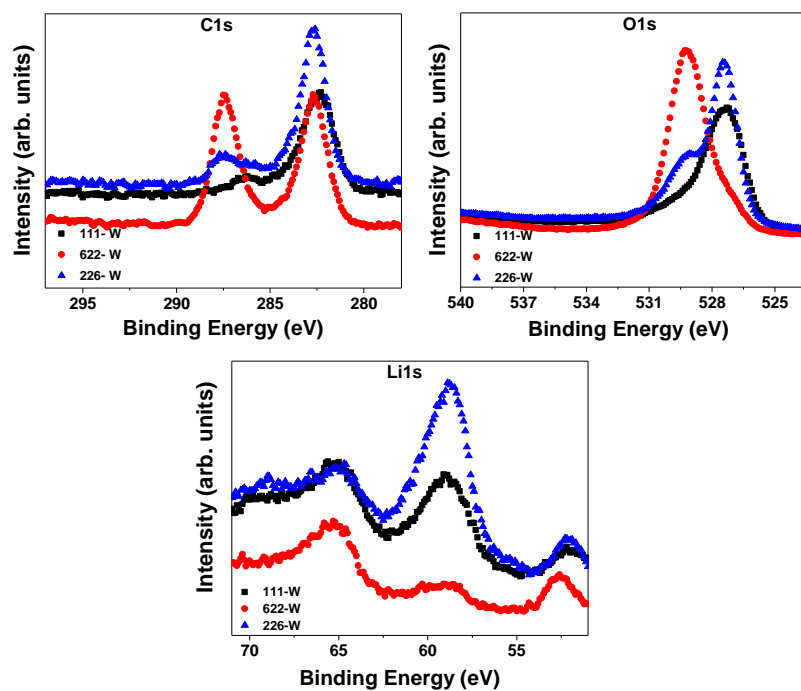
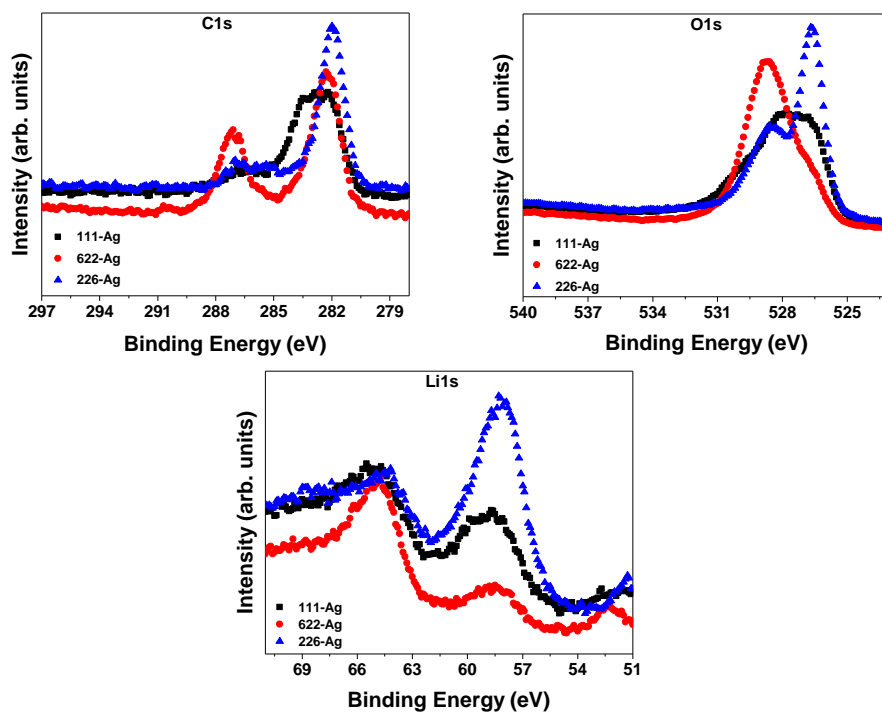


**Figure 66.** C1s, O1s, and Li1s XPS profiles for doped NMC-111, NMC-622, and NMC-226 cathode materials.

### Ag-doped NMC



### Cu-doped NMC

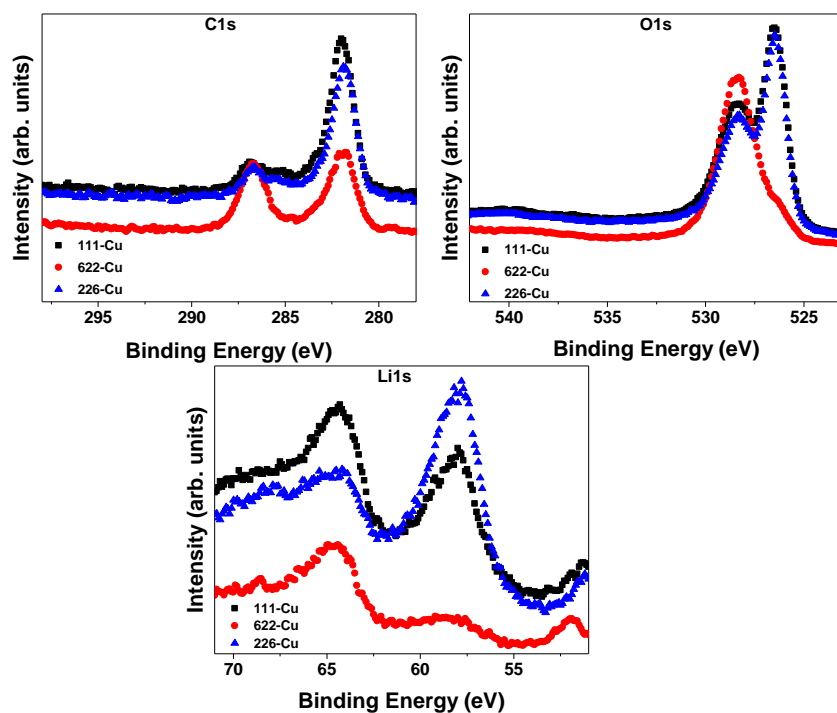
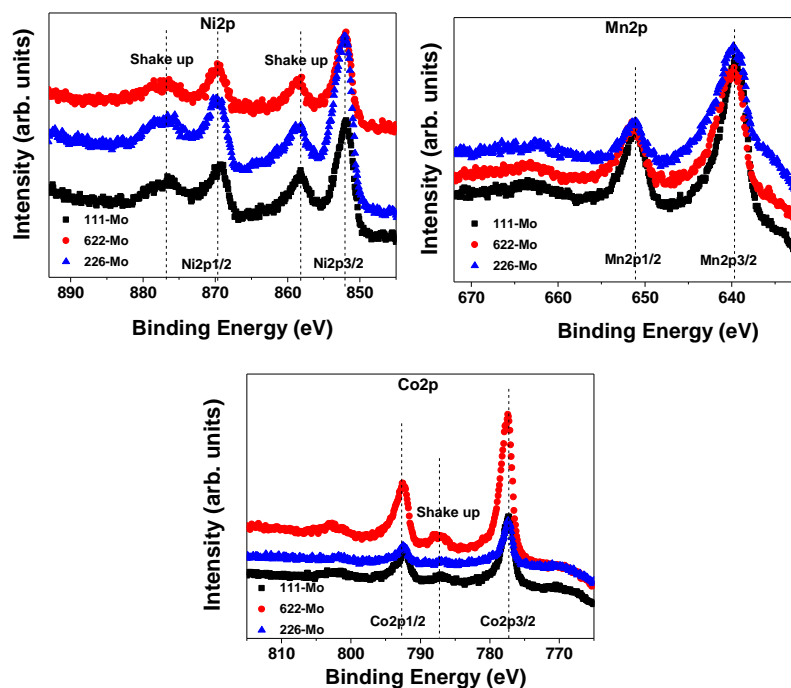
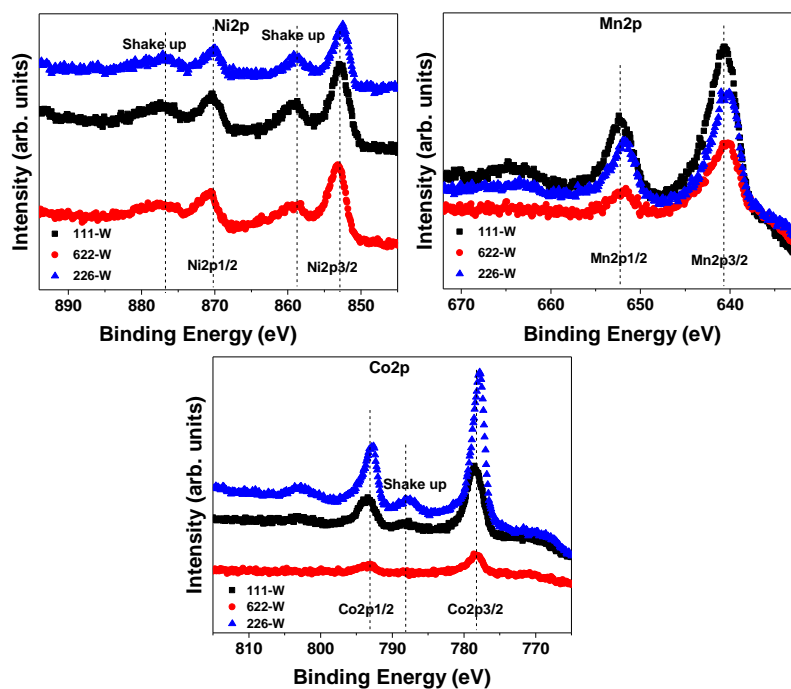


Figure 66. Cont' d

### Mo-doped NMC

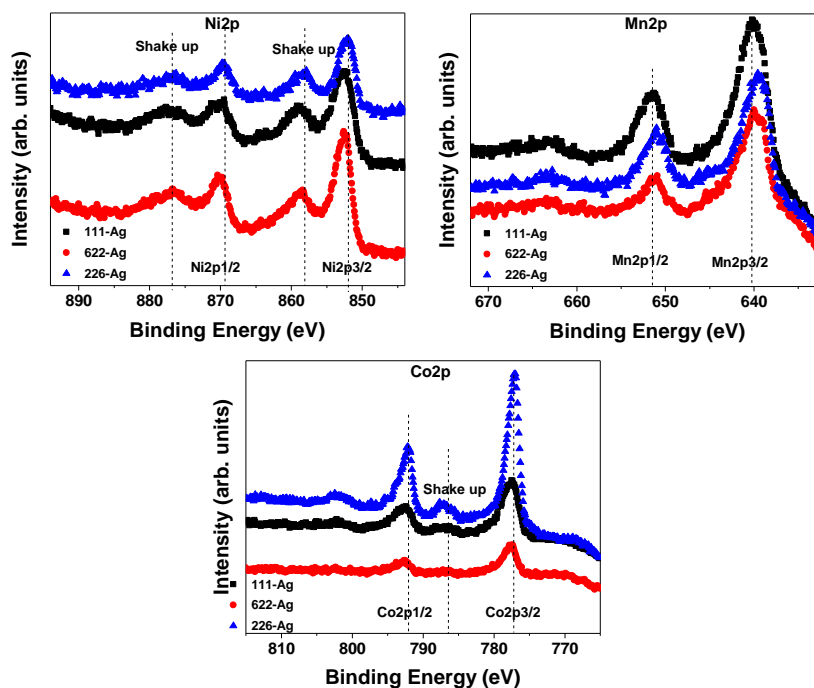


### W-doped NMC



**Figure 67.** XPS profile of doped 111, 622 and 226 NMC cathode materials for Ni2p, Mn2p, and Co2p peaks.

### Ag-doped NMC



### Cu-doped NMC

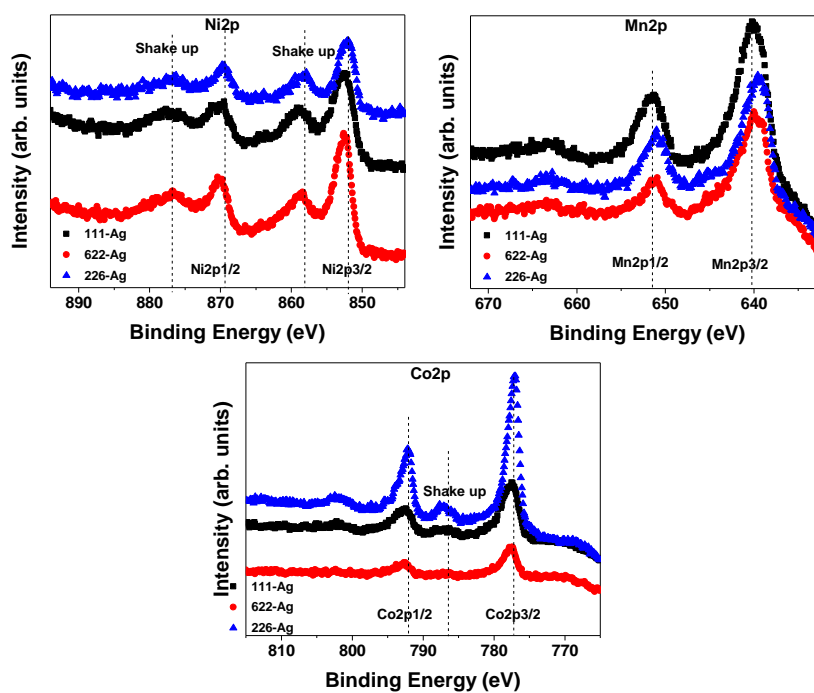
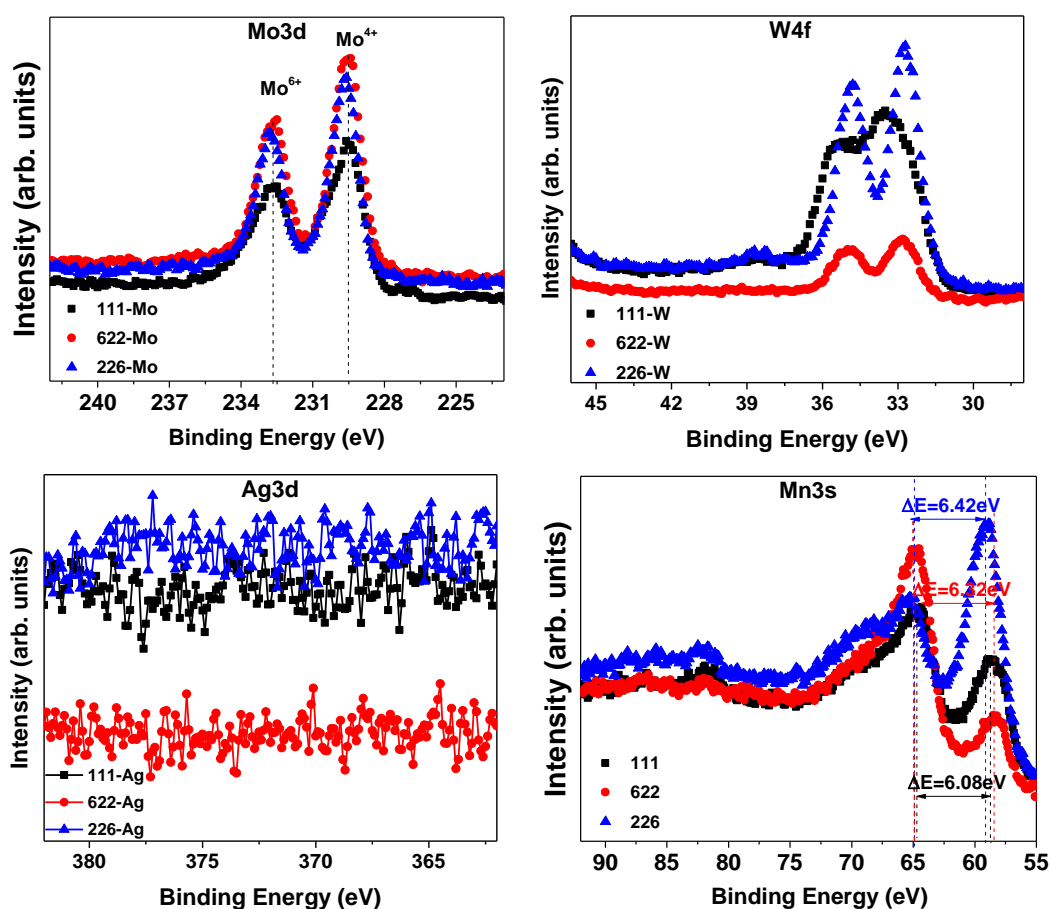


Figure 67. Cont' d

XPS analyses of doping elements are shown in Figure 68. Mo3d peaks were measured for each cathode as 232.7 and 229.6 eV indicating the Mo oxidation state of Mo<sup>6+</sup> and Mo<sup>4+</sup>, respectively [155]. W4f peaks in each sample were measured as 34.9 eV and 32.7 eV which pointed out that W had an oxidation state of W<sup>6+</sup> [156]. Ag could not be detected in any XPS analysis of the respective cathode materials. The similar findings were also obtained in ICP-MS analyses, where very limited Ag (70% less than the intended value) could be measured in Ag-doped cathode materials. Thus, it can be deduced that complete replacement of transition metals with Ag could not be achieved. However, Ag might still be present in the core part of the structure with a limited amount. Cu2p was measured as ~970 eV, while CuLMM was scanned as 935 eV and 942 eV in the region of Auger kinetic energy. This might refer to Cu<sup>2+</sup> oxidation state [157,158].

Here, it should be mentioned that neither Ni<sup>3+</sup> nor Co<sup>4+</sup> oxidation states were observed in XPS analyses. This is important since these ions could lead structural instability in the layered cathode materials. This was also in good agreement with TEM studies, where pure layered structure was observed without formation of a secondary phase.



**Figure 68.** Representative Mn3s XPS profile, spectra of each related doped element of 111, 622 and 226 NMC cathode materials.

## 4.4 Electrochemical Characterization Results

### 4.4.1 NMC Cathode materials

In electrochemical characterizations, charge-discharge behavior, discharge capacity and cycle life of the active materials were measured using a potentiostat/galvanostat. The electrochemical cells prepared with undoped NMC cathode materials were cycled at different rates, i.e. 0.1C, 0.3C and 1C (1C=170 mAhg<sup>-1</sup>) within 2.7-4.5 V potential interval. The discharge capacity of NMC cathode materials as a function of cycles and voltage profiles are given in Figure 69 and Figure 70, respectively.

Of the cathode materials, NMC-111 cathode performed the highest capacity of 180.5 mAhg<sup>-1</sup>, which is higher than that of commercial LiCoO<sub>2</sub>, 140 mAhg<sup>-1</sup>. This could be attributed to high I<sub>[003]</sub>/I<sub>[104]</sub> ratio indicating the good hexagonal ordering and the limited cation mixing in the structure. NMC-226 exhibited also a high capacity with a value of 161.1 mAhg<sup>-1</sup>, while NMC-262 performed a capacity of 106.5 mAhg<sup>-1</sup>. On the other hand, NMC-622 cathode exhibited the lowest capacity with a value of 81.7 mAhg<sup>-1</sup>. The cation mixing in the structure, where I<sub>[003]</sub>/I<sub>[104]</sub> ratio, 0.6339, was much lower than the critical value of 1.2, could be responsible for such a low capacity. Additionally, side reactions occurred during cycling could be another reason since the Ni-rich cathode materials are known as having high tendency to form Ni-F compounds and a passive surface film with the interaction of electrolyte.

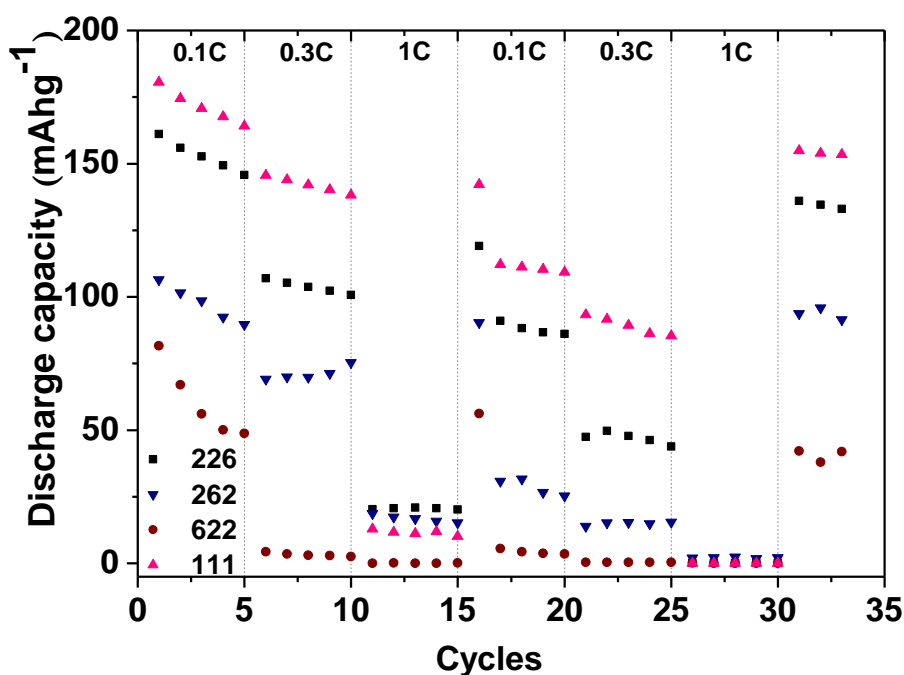


**Figure 69.** Comparison of the discharge capacity of NMC-111, NMC-622, NMC-226, and NMC-262.

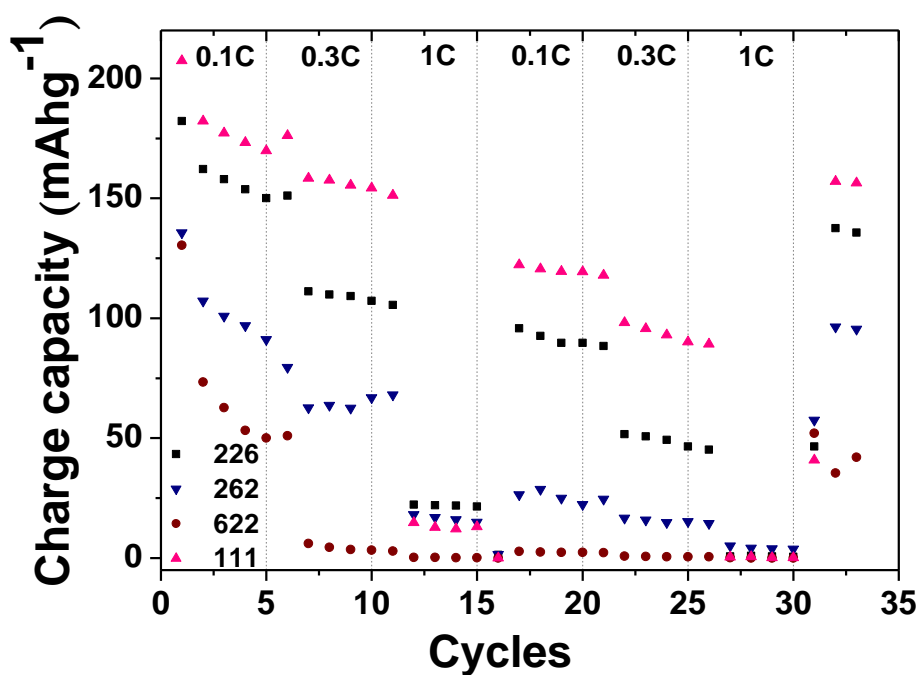


**Figure 69.** Cont' d

Capacity retention of the cathode materials after 31 cycles was determined as 84.4%, 88.0%, 51.6% and 85.8% for NMC-226, NMC-262, NMC-622 and NMC-111 cathode materials, respectively. The electrochemical performance of the cathode materials is summarized in Table 11.

**Table 11.** Electrochemical Properties of the layered NMC cathode materials.

Sample	First Discharge Capacity (mAhg <sup>-1</sup> )	Capacity Retention at Cycle 31 (%)	Capacity Retention at Cycle 32(%)
226	161.1	84.4	83.5
262	106.5	88.0	90.0
622	81.7	51.6	46.4
111	180.5	85.8	85.3

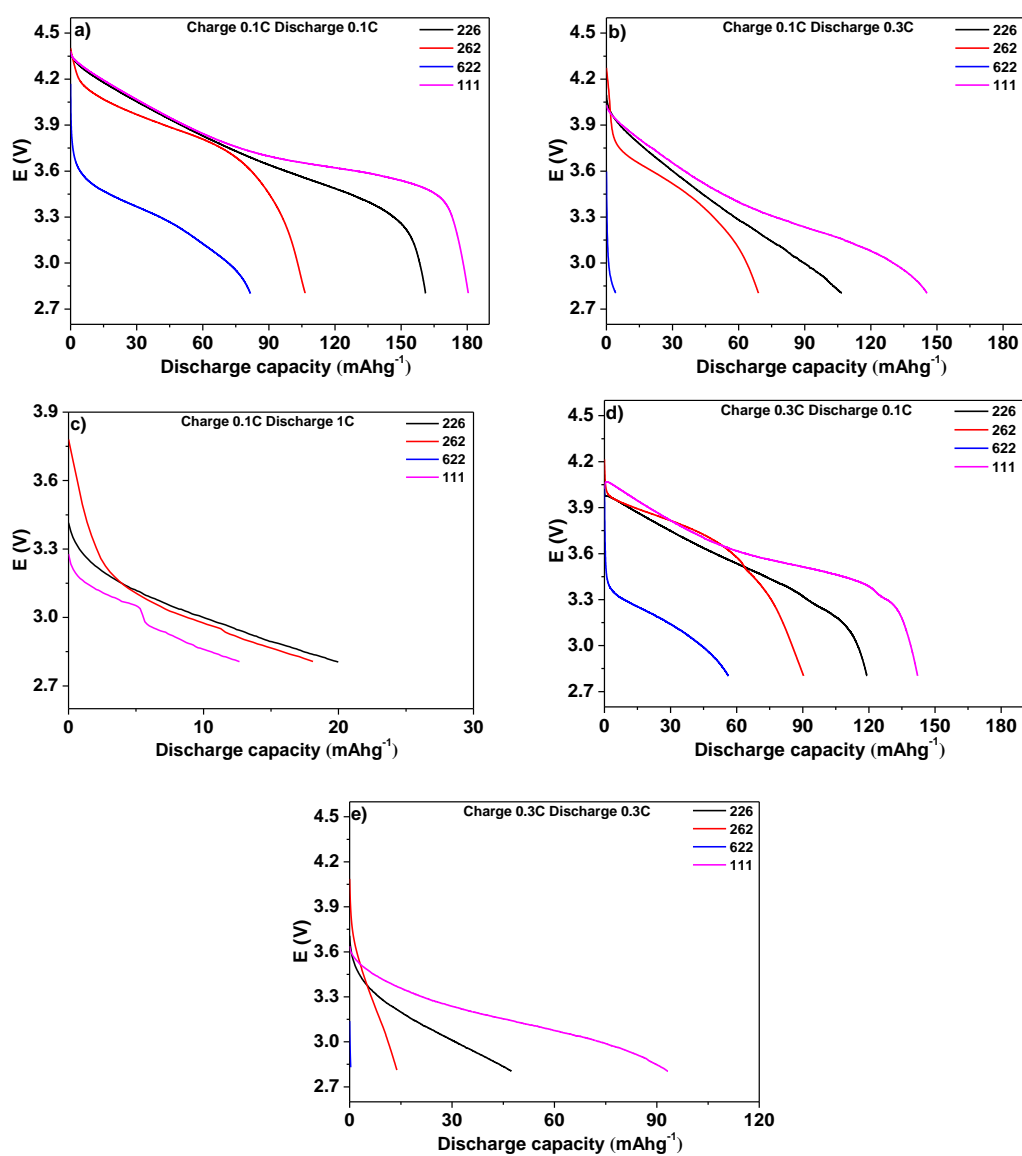


**Figure 70.** Voltage profiles of undoped NMC cathode materials, a) charged at 0.1C and discharged at 0.1C b) charged at 0.1C and discharged at 0.3C c) charged at 0.1C and discharged at 1C d) charged at 0.3C and discharged at 0.1C e) charged at 0.3C and discharged at 0.3C.

The undoped NMC cathode materials were also cycled with increasing discharge rate in the potential window of 2.75-4.5 V. Here, there was a clear shift in capacities with increasing discharge rate. Of the cathode materials, NMC-111 was the only one that exhibited two-step discharge profile at 1C discharge rate. This indicated the presence

of a reaction in the cell causing the increase in impedance. Therefore, it resulted in a capacity loss with the following cycles.

It should be mentioned that the electrochemical performance of active materials could be affected by various factors such as particle size and morphology in active materials, Li-ion diffusion pathway in the structure and as well as the ordering of cation sites in the layered structure. The particle size of the active materials in the study was determined very similar to each other. Additionally, the gap size in the respective active materials was similar as well. Thus, it could be deduced that the cation mixing should be more critical than the respective particle size or mass transfer in the structure for the electrochemical performance of the cathode materials. This could also explain the better performance of NMC-111 as compared to other undoped cathode materials. Additionally, the formation of the surface reconstruction layers, which would be related to the structural stability, during intercalation/deintercalation processes could affect the performance. As discussed in Section 4.2, reconstruction layers could result in the formation of a rock-salt phase with a closed-packed structure or formation of a passivation layer [63]. Both scenarios could prevent the Li diffusion and decreases the efficiency causing capacity fading in NMC cathode materials, particularly in NMC-622.

#### **4.4.2 Doped NMC**

In the electrochemical tests, cells made with doped NMC cathode materials were cycled between 2.7-4.2 V at a 0.1C rate ( $1C=170 \text{ mAhg}^{-1}$ ). The discharge capacity and the charge-discharge profiles of the cathode materials are given in Figure 71 and Figure 72, respectively. The first discharge capacity of doped 111, 622 and 226 layered cathode materials and their capacity retention after 21 cycles are summarized in Table 12.

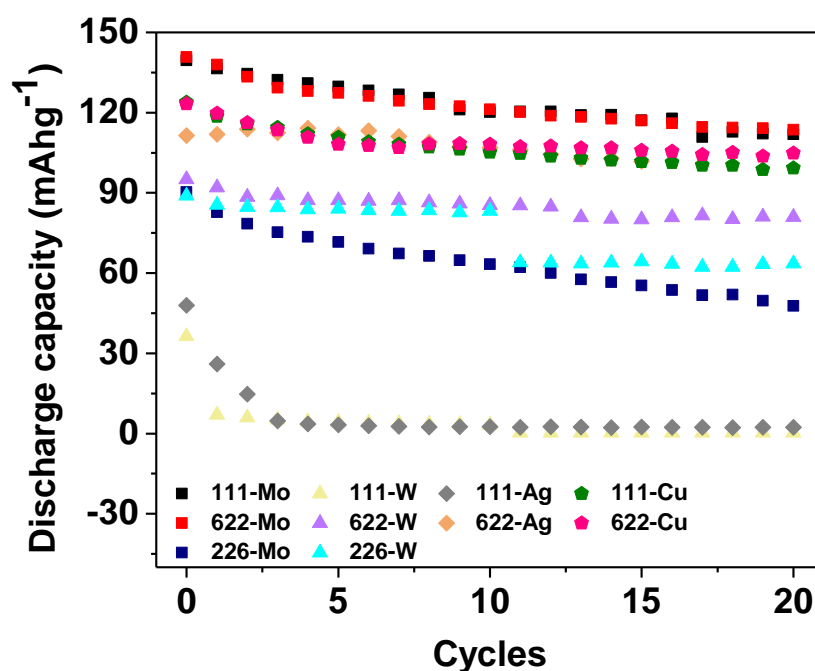


**Figure 71.** The discharge capacity of doped NMC cathode materials as a function of cycles.

Of the doped cathode materials, Mo-doped NMC-111, NMC-622, and NMC-226 exhibited a capacity of  $139.55 \text{ mAhg}^{-1}$ ,  $140.75 \text{ mAhg}^{-1}$  and  $90.30 \text{ mAhg}^{-1}$ , respectively. The measurements revealed that 111-Mo, 622-Mo, and 226-Mo maintained their capacity after 21 charge-discharge cycles at around 80%, 81%, and 53%, respectively. Unlike the doping with Mo, W-doped NMC-111 cathode exhibited a very low first discharge capacity with  $36.32 \text{ mAhg}^{-1}$  and then failed in the fifth cycle. Here, 622-W and 226-W exhibited a capacity of  $95.03 \text{ mAhg}^{-1}$  and  $88.85 \text{ mAhg}^{-1}$ , respectively. The retention in these cathode materials was in the respective order of 83% and 74%. Here, the great portion of the capacity drop in 226-W occurred at the twelfth cycle. In Cu-doped cathode materials, NMC-111 and NMC-622 exhibited very similar first discharge capacity of  $\sim 123 \text{ mAhg}^{-1}$  with an 80% and 85% of capacity retention, respectively. Here, it should be noted that Cu doped NMC-226 cathode failed during the tests. Of the Ag-doped cathode materials, 111-Ag and 622-Ag performed a capacity of  $47.91 \text{ mAhg}^{-1}$  and  $111.40 \text{ mAhg}^{-1}$ , respectively, where 226-Ag failed during the test as in the case of 226-Cu. Capacity

retention of 111-Ag was quite low with a value of 5%, while 622-Ag had a retention of 91%.

**Table 12.** The first discharge capacity of the doped NMC-111, NMC-622 and NMC-226 layered cathode materials and their capacity retention after cycles.

<b>Sample</b>	<b>First Discharge Capacity (mAhg<sup>-1</sup>)</b>	<b>Capacity retention after cycling (%)</b>
<b>111-Mo</b>	139.55	80
<b>622-Mo</b>	140.75	81
<b>226-Mo</b>	90.30	53
<b>111-W</b>	36.32	0
<b>622-W</b>	95.03	83
<b>226-W</b>	88.85	74
<b>111-Ag</b>	47.91	5
<b>622-Ag</b>	111.40	91
<b>111-Cu</b>	123.87	80
<b>622-Cu</b>	123.31	85

Discharge and charge voltage profiles, at the 1<sup>st</sup> cycle, were plotted in Figure 72. The highest capacity in the cathode materials was measured in 622-Mo and 111-Mo with similar values. It was followed by 111-Cu and 622-Cu among the other doped NMC cathode materials. The lowest capacity was observed in 111-Ag and 111-W NMC cathode materials. These cathode materials also could not recover their capacity with the subsequent cycles. This low performance could be attributed to the high cation mixing, i.e.  $I_{[003]}/I_{[104]} < 1.2$  with narrower Li-gap size as compared to the other cathode materials. They also exhibited relatively higher impedance when they were compared to others.

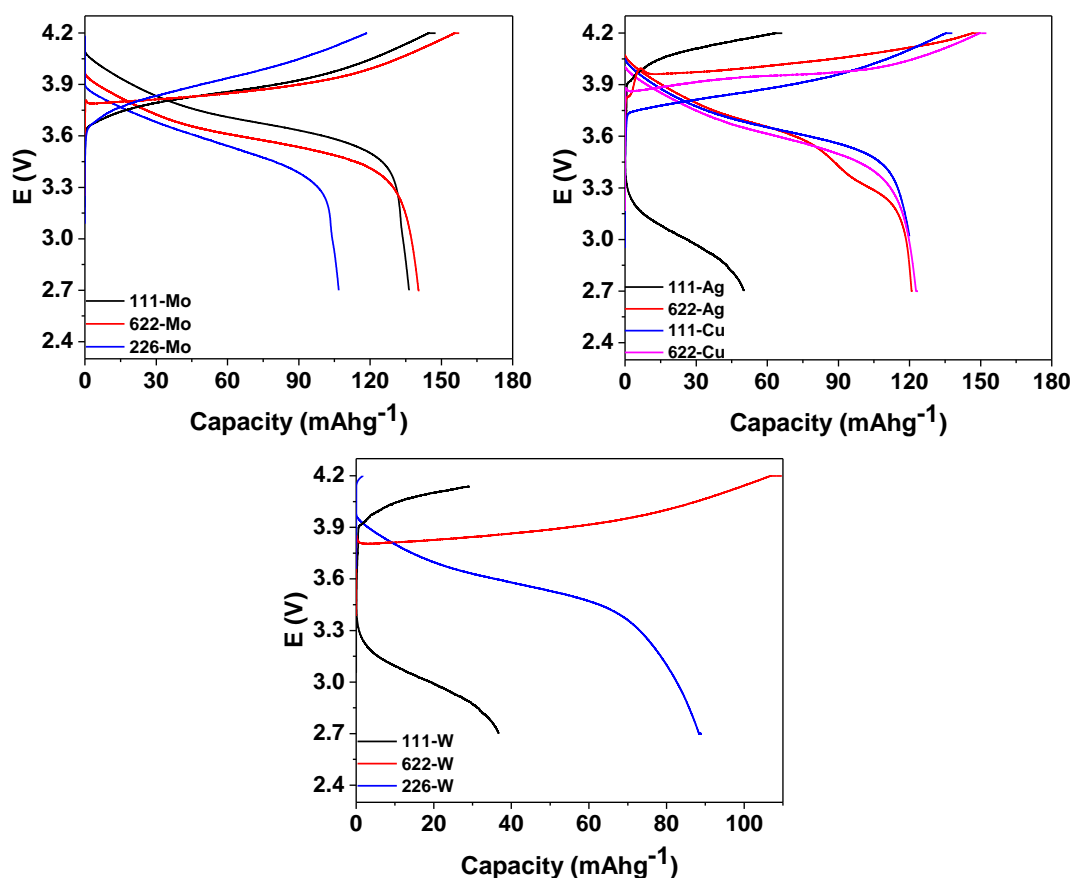


**Figure 72.** Initial charge-discharge profile of NMC cathode materials from 2.7 V to 4.2 V at 0.1C.

Here, there are some of the highlights should be mentioned about the voltage profiles. 622-Ag had a two-step discharge profile indicating a change in the reaction mechanism around 3.3-3.4 V. Here, it should be mentioned that the voltage profiles could indicate the formation of a surface layer between the cathode and electrolyte or a phase transformation from the layered structure causing the capacity fading. These also result in a difference in the amount of Li-ions during charging/discharging and causes a sign in the voltage profiles. Thus, the two-step discharge profiles could be caused by the formation of a surface layer or a phase transformation. Moreover, 622-Ag had IR-drop during charging which might be due to the oxygen migration from the structure causing an increase in the internal resistance [159].

Coulombic efficiency of the cathode materials was calculated and given in Figure 73. Here, Coulombic efficiency (CE) is used to define the ratio of discharge capacity to the charge capacity of a cell. Generally, higher CE indicates a longer cycle life of the battery. In addition to that CE is used to observe the magnitude of the side reactions [160] and also predict its relationship with the capacity fading. General practice in NMC cathode materials particularly concentrates on the side reactions [161]. CE of NMC cathode materials in the range of 2.7 V-4.2 V potential window was determined very close to each other, except 111-W. Here, 111-W exhibited a drastic drop, at the eleventh cycle, in CE indicating the severe capacity loss. Thus, this might be caused by the side reactions, i.e. electrolyte decomposition during cycling. But also, 111-W NMC cathode performed also drastically drop after 5<sup>th</sup> cycle, Figure 71. This abnormal behavior was observed at the first significant capacity loss. Although its discharge and charge capacity were very low but close to each other, it had behaved like recovering itself.

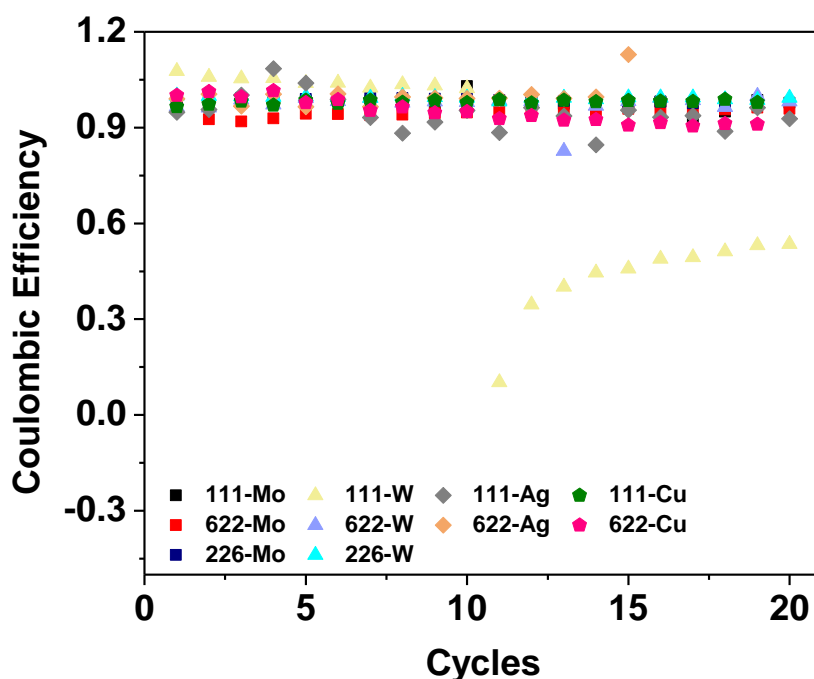


**Figure 73.** Coulombic efficiency of doped NMC cathode materials.

EIS measurements of doped NMC cathode materials were performed in the frequency range from 300 kHz to 3 mHz with a 10 mV AC amplitude. The EIS spectrum of the cathode materials before the first charge at 0% SOC was given in Figure 74-77. Here, EIS intercepts in the range of high-frequency are often contributed to resistance involving from Li-ion transport through the electrolyte. In a typical EIS spectrum, there could be several semi-circles ending with a linear segment representing the Li-ion diffusion. The semi-circles at high and intermediate frequency regions are often associated with the capacitive and resistive behavior caused by the presence of surface films, the formation of a double layer and a charge transfer process [162]. The linear segment at the low-frequency region is generally attributed to Li-ion diffusion in the particles of the active material which could be interpreted by Warburg-type elements. In the EIS interpretation, finite space Warburg element (FSW), due to the nature of the NMC cathode materials, was used instead of infinite Warburg element. In FSW, the center of the particle (the second boundary condition) would shortly assume the zero flux condition and this caused a capacitive effect to be seen in the spectrum. FSW impedance can be calculated by Equation 4 which was defined in Section 3.5.

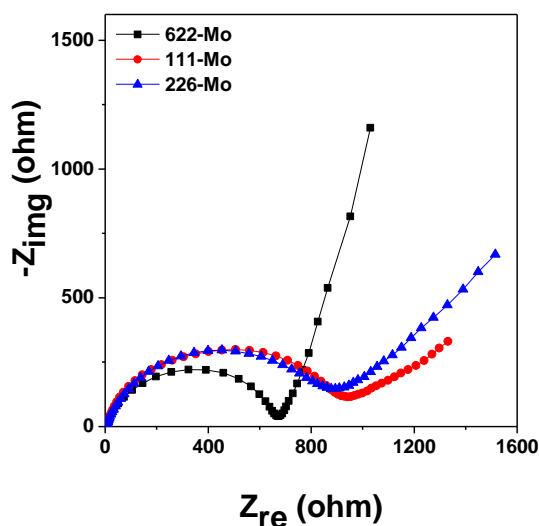


**Figure 74.** EIS spectrum of Mo-doped NMC-111, NMC-622, and NMC-226 layered cathode materials.

The fitted values of the circuit elements are given in Table 13. Here, it should be mentioned that the lower internal impedance in the cathode materials, particularly in NMC-111 and NMC-622, could be related to their particle morphology. The general morphology of the active materials was in the form of loose aggregated with relatively larger particles. However, the size of the primary particles and the porosity in the aggregates varied in each cathode. Particularly, NMC-111 and NMC-622 had a more loose aggregate structure with relatively larger primary particles. Thus, this loose structure could result in a higher contact with the electrolyte causing lower internal impedance. Besides, it could also cause shorter effective diffusion distances which indicate a faster diffusion time,  $\tau$  (s).

Of the EIS measurements, it was observed that Mo-doped cathode materials, particularly 622-Mo, had a lower charge transfer resistance and a lower time constant as compared to most of the other doped cathode materials.

**Table 13.** Equivalent circuit values of impedance fittings for the electrodes ( $\tau$  is the time constant).

<b>Sample</b>	<b>R<sub>CT</sub> (<math>\Omega</math>)</b>	<b><math>\tau</math> (s)</b>	<b><math>\chi^2</math></b>
<b>111-Mo</b>	908	25.5	$4.5 \times 10^{-3}$
<b>226-Mo</b>	816	25.6	$1.8 \times 10^{-3}$
<b>622-Mo</b>	629	15.5	$3.9 \times 10^{-3}$
<b>111-W</b>	6430	-	$9.6 \times 10^{-3}$
<b>226-W</b>	13000	-	$8.5 \times 10^{-3}$
<b>622-W</b>	981	68.3	$3.6 \times 10^{-3}$
<b>111-Ag</b>	580	38.9	$3.12 \times 10^{-3}$
<b>622-Ag</b>	342	6.78	$7.05 \times 10^{-3}$
<b>111-Cu</b>	718	19.1	$3.03 \times 10^{-3}$
<b>622-Cu</b>	592	5.43	$4.5 \times 10^{-3}$

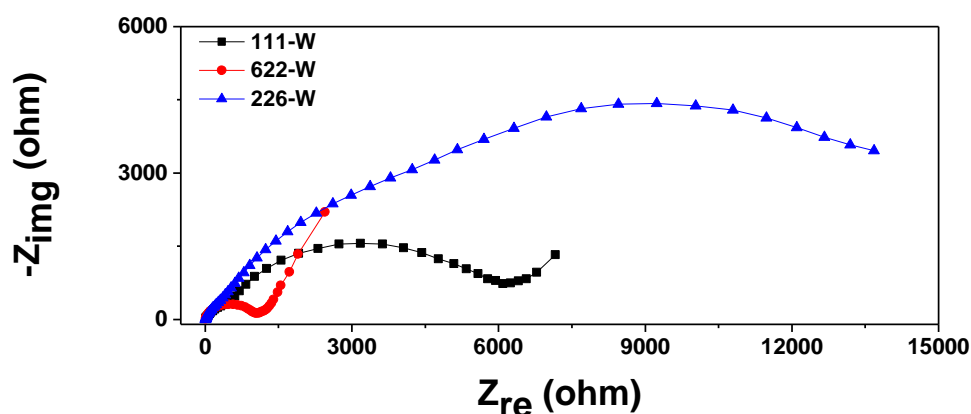


**Figure 75.** EIS spectrum of W-doped NMC-111, NMC-622, and NMC-226 layered cathode materials.

The highest impedance for charge transfer and the diffusion time constant were observed in W doped cathode materials, where the highest impedance was measured in 226-W. EIS spectrum of 111-W and 226-W exhibited a gradual increase in the impedance containing two depressed semicircles. It was followed by a diffusional behavior in the case of 111-W. This high impedance of these cathode materials could be caused by a surface interaction with electrolyte causing the formation of a surface film or a phase transformation during cycling [163–165].

In the case of Ag and Cu doped cathode materials, very similar EIS responses were obtained despite the Ag-doped cathode materials exhibited relatively lower impedance. Of them, doped NMC-622 cathode materials exhibited a lower impedance as compared to NMC-111, while doped NMC-226 cathode materials failed during the test as discussed above. In both 111-Cu and 111-Ag spectra, a bended curve was observed at the initial step of Li-ion diffusion, shown in the insets of the respective figures. The reaction in this frequency range is often associated with the Warburg-type impedance. However, it was observed a slight deviation from the typical Warburg-type element. This deviation is often associated with the presence of inhomogeneous particle size distribution in the active materials. Additionally, this behavior is experienced when the particle morphology in the active materials is in

the form of cylindrical or spherical, where the planar particle morphology exhibits typical Warburg-type impedance [166]. Thus, the spherical particle morphology of the cathode materials in the current study could be responsible for this deviation.

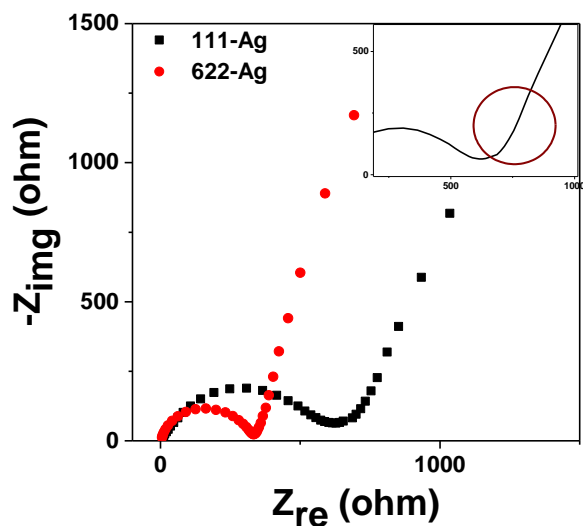


**Figure 76.** EIS spectrum of Ag-doped NMC-111 and NMC-622 layered cathode materials.

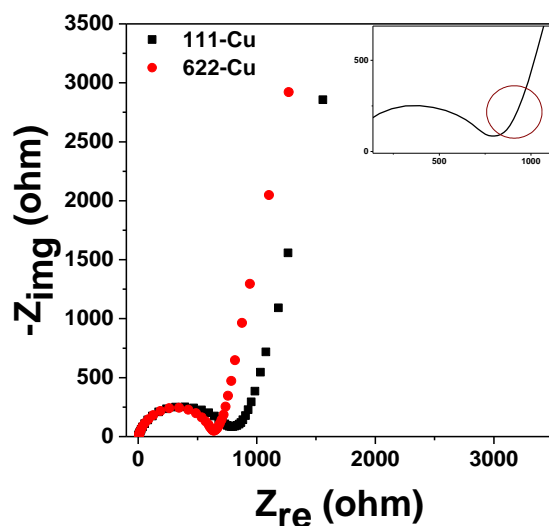


**Figure 77.** EIS spectrum of Cu-doped NMC-111 and NMC-622 layered cathode materials.

As discussed above, electrochemical behavior of the cathode materials, e.g. Li-ion diffusion and charge transfer resistance are affected by the morphology of the particles. In the current study, two different type of morphology in the active materials causing the variation in the electrochemical performances. One is the aggregates which were densely packed with relative smaller primary particles. The second type is the aggregates which were loosely packed with larger primary particles. The loose aggregate morphology was generally observed in NMC-111 and NMC-622 cathode materials, while the others consisted of the densely packed aggregates. The loose aggregate structure often resulted in a higher discharge capacity with a lower internal resistance. This might be due to the fact that large primary particles with more open structure could make the intercalation/deintercalation of lithium ions easier. On the other hand, the densely packed aggregates with smaller primary particles may bring difficulties in electrode-electrolyte interaction causing higher internal resistance. This was also confirmed by physical adsorption studies. Undoped cathode materials had surface area of 9 m<sup>2</sup>/g, 13 m<sup>2</sup>/g, and 7 m<sup>2</sup>/g for NMC-111, NMC-226, and NMC-622, respectively. On the other hand, surface area of the cathode materials increased approximately to 13 m<sup>2</sup>/g, 16 m<sup>2</sup>/g, and 24 m<sup>2</sup>/g for all doped cathode materials of NMC-111, NMC-226, and NMC-622, respectively. Similarly, micro pore area also increased from 12 m<sup>2</sup>/g, 17 m<sup>2</sup>/g, and 10 m<sup>2</sup>/g to approximately 18 m<sup>2</sup>/g, 20 m<sup>2</sup>/g, and 35 m<sup>2</sup>/g in the case of doping of NMC cathode materials. This increase in both the surface area and the microporous area has proven to be a constant contact between the particles by allowing passage through the electrolyte within the particles, especially in the case of doping of NMC-622. Thus, this kind of loose porous structure resulted in shorter diffusion distances and thus, faster diffusion time,  $\tau$  (s).



## CHAPTER 5

### CONCLUSIONS

The aim of this study was to investigate the effects of Ni:Mn:Co mole ratio and doping elements, i.e. Mo, W, Ag and Cu in  $\text{Li}(\text{Ni}_x\text{Mn}_y\text{Co}_{1-x-y-z}\text{M}_z)\text{O}_2$  (NMC) cathode materials for Li-ion batteries.  $\text{Li}(\text{Ni}_{1/3}\text{Mn}_{1/3}\text{Co}_{1/3})\text{O}_2$  (NMC-111),  $\text{Li}(\text{Ni}_{0.2}\text{Mn}_{0.2}\text{Co}_{0.6})\text{O}_2$  (NMC-226),  $\text{Li}(\text{Ni}_{0.6}\text{Mn}_{0.2}\text{Co}_{0.2})\text{O}_2$  (NMC-622),  $\text{Li}(\text{Ni}_{0.2}\text{Mn}_{0.6}\text{Co}_{0.2})\text{O}_2$  (NMC-262) and their doped equivalents with the doping weight ratio of 2% were synthesized via spray pyrolysis. This method was used to have a spherical fine-sized morphology in the powders synthesized. Heat-treatment was performed to provide well-defined splitting of (006)/(102) and (108)/(110) diffraction peaks in XRD patterns as an indicator for a layered structure and a good hexagonal ordering. For this purpose, parameters such as reaction temperature and flow rate of carrier gas etc. in spray pyrolysis were optimized.

The cathode compositions were analyzed via ICP-MS and it was observed that the intended compositions were achieved in cathode materials with the exception of Ag doping. The structural characterization also revealed that the layered structure in many cathode materials was successfully obtained. Of the undoped NMC cathode materials, NMC-111 exhibited relatively lower cation mixing in the structure leading highest discharge capacity. In the doped compositions, Mo-doped cathode materials in all Ni:Mn:Co mole ratio exhibited relatively lower cation mixing together with the wider Li-gap. This was also valid for all 622 compositions independent from the doping elements, except W.

The electrochemical cells prepared with undoped NMC cathode materials were cycled in the range of 2.7 V-4.5 V potential window at 0.1C, 0.3C and 1C rate (1C=170 mAhg<sup>-1</sup>). Capacity retention after 32 cycles was determined as 85.3 % and 90 %, for NMC-111 and NMC-262 cathode materials, respectively. However, the structural stability couldn't be maintained in NMC-262 compositions which have relatively high Mn content and layered-to-spinel transformation was observed in these cathode materials. NMC-111 compound showed higher discharge capacity with a value of 180.5 mAhg<sup>-1</sup>, which was attributed to the low or negligible cation mixing as evidenced by high I<sub>[003]</sub>/I<sub>[104]</sub> intensity ratio. On the other hand, the NMC-622 composition showed the lowest capacity with 81.7 mAhg<sup>-1</sup>. The cation mixing in the structure, where I<sub>[003]</sub>/I<sub>[104]</sub> ratio, 0.6339, was much lower than the critical value of 1.2, could be responsible for such a low capacity. In addition to that, this might be also caused by the side reactions, especially at higher voltages as in the case of 4.5 V, at the cathode/electrolyte interface which is very common in Ni-rich compounds. Capacity retention in the cathode materials was determined as approximately 85%, 88%, 52% and 86% for NMC-226, NMC-262, NMC-622 and NMC-111, respectively after 31 charge-discharge cycles.

Doped NMC cathode materials were cycled between 2.7-4.25 V at a 0.1C rate (1C=170 mAhg<sup>-1</sup>). Mo-doped NMC-111 and NMC-622 exhibited a capacity of 139.55 mAhg<sup>-1</sup> and 140.75 mAhg<sup>-1</sup> with 80% and 81% capacity retention, respectively. Both Cu-doped NMC-111 and NMC-622 exhibited very similar first discharge capacity with a value of ~123 mAhg<sup>-1</sup> with 80% and 85% of capacity retention, respectively. 622-W showed a comparative capacity with 111 mAhg<sup>-1</sup> and its capacity retention was also good which was 83% after 21 cycles and 80% after 38 cycles. 226-W exhibited first discharge capacity of ~89 mAhg<sup>-1</sup>; however, it had lost 30% of its capacity after only 12 cycles. Of the doped cathode materials, 111-Ag and 111-W NMC performed the worst discharge capacity and rate capability with increasing impedance during cycling.

In the current study, two different type of morphology in the active materials causing the variation in the electrochemical performances. One is the aggregates which were densely packed with relative smaller primary particles. The second type is the aggregates which were loosely packed with larger primary particles. The loose aggregate morphology was generally observed in NMC-111 and NMC-622 cathode materials, while the others consisted of the densely packed aggregates. Here, it should be mentioned that the structure of loose aggregates with larger primary particles was dominant in particularly NMC-622 cathode materials. This loose aggregate structure often resulted in a higher discharge capacity with a lower internal resistance. This might be due to the fact that large primary particles with more open structure could make the intercalation/deintercalation of lithium ions easier. On the other hand, the densely packed aggregates with smaller primary particles might have brought some difficulties in electrode-electrolyte interaction causing higher internal resistance. Additionally, this higher capacity in doped NMC-622 cathode materials can be attributed to the hindering of cation mixing between Li/Ni by doping elements since the doping elements and the ratio in transitions metals substantially affected the particle morphology in the active materials.



## REFERENCES

- [1] Manthiram A. An Outlook on Lithium Ion Battery Technology. *ACS Cent Sci* 2017;3:1063–9. doi:10.1021/acscentsci.7b00288.
- [2] Mizushima K, Jones P, Wiseman P, Goodenough J.  $\text{Li}_x\text{CoO}_2$  ( $0 < x \leq 1$ ): A new cathode material for batteries of high energy density. *Solid State Ionics* 1981;3–4:171–4. doi:10.1016/0167-2738(81)90077-1.
- [3] Goodenough JB. Cathode materials: A personal perspective. *J Power Sources* 2007;174:996–1000. doi:https://doi.org/10.1016/j.jpowsour.2007.06.217.
- [4] Yazami R, Touzain P. A reversible graphite-lithium negative electrode for electrochemical generators. *J Power Sources* 1983;9:365–71. doi:10.1016/0378-7753(83)87040-2.
- [5] Ozawa K. Lithium-ion rechargeable batteries with  $\text{LiCoO}_2$  and carbon electrodes: the  $\text{LiCoO}_2/\text{C}$  system. *Solid State Ionics* 1994;69:212–21. doi:10.1016/0167-2738(94)90411-1.
- [6] Yuan X, Liu H, Zhang J. *Lithium-ion batteries advanced materials and technologies* 2012.
- [7] Padhi AK, Nanjundaswamy KS, Goodenough JB. Phospho-olivines as Positive-Electrode Materials for Rechargeable Lithium Batteries. *J Electrochem Soc* 1997;144:1188–94. doi:10.1684/agr.2014.0700.
- [8] Miara LJ, Richards WD, Wang YE, Ceder G. First-Principles Studies on Cation Dopants and Electrolyte|Cathode Interphases for Lithium Garnets. *Chem Mater* 2015;27:4040–7. doi:10.1021/acs.chemmater.5b01023.
- [9] Liu H, Li C, Zhang HP, Fu LJ, Wu YP, Wu HQ. Kinetic study on  $\text{LiFePO}_4/\text{C}$  nanocomposites synthesized by solid state technique. *J Power Sources* 2006;159:717–20. doi:10.1016/j.jpowsour.2005.10.098.

- [10] Hamid NA, Wennig S, Hardt S, Heinzl A, Schulz C, Wiggers H. High-capacity cathodes for lithium-ion batteries from nanostructured  $\text{LiFePO}_4$  synthesized by highly-flexible and scalable flame spray pyrolysis. *J Power Sources* 2012;216:76–83. doi:10.1016/j.jpowsour.2012.05.047.
- [11] Delacourt C, Laffont L, Bouchet R, Wurm C, Leriche J-B, Morcrette M, et al. Toward Understanding of Electrical Limitations (Electronic, Ionic) in  $\text{LiMPO}_4$  (M=Fe, Mn) Electrode Materials. *J Electrochem Soc* 2005;152:A913. doi:10.1149/1.1884787.
- [12] Chung S-Y, Bloking JT, Chiang Y-M. Electronically conductive phospho-olivines as lithium storage electrodes. *Nat Mater* 2002;1:123–8. doi:10.1038/nmat732.
- [13] Xiao J, Chernova NA, Stanley Whittingham M. Influence of manganese content on the performance of  $\text{LiNi}_{0.9-y}\text{Mn}_y\text{Co}_0.1\text{O}_2$  (0.45  $\leq y \leq$  0.60) as a cathode material for Li-Ion batteries. *Chem Mater* 2010;22:1180–5. doi:10.1021/cm902627w.
- [14] Kabir MM, Demirocak DE. Degradation mechanisms in Li-ion batteries: a state-of-the-art review. *Int J Energy Res* 2017;41:1963–86. doi:10.1002/er.3762.
- [15] Geetha A, Subramani C. A comprehensive review on energy management strategies of hybrid energy storage system for electric vehicles. *Int J Energy Res* 2017;41:1817–34. doi:10.1002/er.3730.
- [16] Lewis GN, Keyes FG. The Potential of the Lithium Electrode. *J Am Chem Soc* 1913;35:340–4. doi:10.1021/ja02193a004.
- [17] Whittingham MS. Electrical Energy Storage and Intercalation Chemistry. *Science* (80-) 1976;192:1126–7. doi:10.1126/science.192.4244.1126.
- [18] Armand M, Touzain P. Graphite intercalation compounds as cathode materials. *Mater Sci Eng* 1977;31:319–29. doi:https://doi.org/10.1016/0025-5416(77)90052-0.

- [19] Tarascon J-M, Armand M. Issues and challenges facing rechargeable lithium batteries. *Nature* 2001;414:359–67. doi:10.1038/35104644.
- [20] Kim Y-O, Park S-M. Intercalation Mechanism of Lithium Ions into Graphite Layers Studied by Nuclear Magnetic Resonance and Impedance Experiments. *J Electrochem Soc* 2001;148:A194. doi:10.1149/1.1345870.
- [21] Dahlin GR, Strom KE. *Lithium Batteries - Research, Technology and Applications*. 2010.
- [22] Batteries HOF, Library DE, Companies TM. *Handbook of batteries*. 2004. doi:10.1016/0378-7753(86)80059-3.
- [23] Zu C-X, Li H. Thermodynamic analysis on energy densities of batteries. *Energy Environ Sci* 2011;4:2614–24. doi:10.1039/C0EE00777C.
- [24] M.M. D. *Encyclopedia of Sustainability Science and Technology*. New York, NY: Springer New York; 2012. doi:10.1007/978-1-4419-0851-3.
- [25] Jung YS, Cavanagh AS, Dillon AC, Groner MD, George SM, Lee S-H. Enhanced stability of LiCoO<sub>2</sub> cathodes in lithium-ion batteries using surface modification by atomic layer deposition. *J Electrochem Soc* 2010;157:A75–81.
- [26] Dyer LD, Borie BS, Smith GP. Alkali Metal-Nickel Oxides of the Type MNiO<sub>2</sub>. *J Am Chem Soc* 1954;76:1499–503. doi:10.1021/ja01635a012.
- [27] Ohzuku T, Ueda A, Nagayama M. Electrochemistry and Structural Chemistry of LiNiO<sub>2</sub> (R3m) for 4 Volt Secondary Lithium Cells. *J Electrochem Soc* 1993;140:1862. doi:10.1149/1.2220730.
- [28] Dahn JR, Fuller EW, Obrovac M, Von Sacken U. Thermal stability of Li<sub>x</sub>CoO<sub>2</sub>, Li<sub>x</sub>NiO<sub>2</sub> and λ-MnO<sub>2</sub> and consequences for the safety of Li-ion cells. *Solid State Ionics* 1994;69:265–70.

- [29] Aurbach D, Markovsky B, Salitra G, Markevich E, Talyossef Y, Koltypin M, et al. Review on electrode-electrolyte solution interactions, related to cathode materials for Li-ion batteries. *J Power Sources* 2007;165:491–9. doi:10.1016/j.jpowsour.2006.10.025.
- [30] Delmas C, Pérès JP, Rougier A, Demourgues A, Weill F, Chadwick AV, et al. On the behavior of the  $\text{Li}_x\text{NiO}_2$  system: an electrochemical and structural overview. *J Power Sources* 1997;68:120–5. doi:10.1016/S0378-7753(97)02664-5.
- [31] Rougier A, Gravereau P, Delmas C. Optimization of the Composition of the  $\text{Li}_{1-z}\text{Ni}_{1+z}\text{O}_2$  Electrode Materials: Structural, Magnetic, and Electrochemical Studies. *J Electrochem Soc* 1996;143:1168–75.
- [32] Ohzuku T, Ueda A, Nagayama M, Iwakoshi Y, Komori H. Comparative study of  $\text{LiCoO}_2$ ,  $\text{LiNi}_{1/2}\text{Co}_{1/2}\text{O}_2$  and  $\text{LiNiO}_2$  for 4 volt secondary lithium cells. *Electrochim Acta* 1993;38:1159–67. doi:https://doi.org/10.1016/0013-4686(93)80046-3.
- [33] Nonaka T, Okuda C, Ukyo Y, Okamoto T. In situ XAFS study on cathode materials for lithium-ion batteries. *J Synchrotron Radiat* 2001;8:869–71.
- [34] Ito Y, Ukyo Y. Performance of  $\text{LiNiCoO}_2$  materials for advanced lithium-ion batteries. *J Power Sources* 2005;146:39–44. doi:https://doi.org/10.1016/j.jpowsour.2005.03.091.
- [35] Ueda A, Ohzuku T. Solid-State Redox Reactions of  $\text{LiNi}_{0.5}\text{Co}_{0.5}\text{O}_2$  ( $\text{R}3\text{m}$ ) for 4 Volt Secondary Lithium Cells. *J Electrochem Soc* 1994;141:2010. doi:10.1149/1.2055051.
- [36] Albrecht S, Kümpers J, Kruft M, Malcus S, Vogler C, Wahl M, et al. Electrochemical and thermal behavior of aluminum- and magnesium-doped spherical lithium nickel cobalt mixed oxides  $\text{Li}_{1-x}(\text{Ni}_{1-y-z}\text{Co}_y\text{M}_z)\text{O}_2$  ( $\text{M} = \text{Al}, \text{Mg}$ ). *J Power Sources* 2003;119–121:178–83. doi:10.1016/S0378-7753(03)00175-7.

- [37] Bloom I, Jones SA, Battaglia VS, Henriksen GL, Christophersen JP, Wright RB, et al. Effect of cathode composition on capacity fade, impedance rise and power fade in high-power, lithium-ion cells. *J Power Sources* 2003;124:538–50. doi:[https://doi.org/10.1016/S0378-7753\(03\)00806-1](https://doi.org/10.1016/S0378-7753(03)00806-1).
- [38] Armstrong AR, Bruce PG. Synthesis of layered LiMnO<sub>2</sub> as an electrode for rechargeable lithium batteries. *Nature* 1996;381:499.
- [39] Vetter J, Novák P, Wagner MR, Veit C, Möller K-C, Besenhard JO, et al. Ageing mechanisms in lithium-ion batteries. *J Power Sources* 2005;147:269–81. doi:10.1016/j.jpowsour.2005.01.006.
- [40] Gowda SR, Gallagher KG, Croy JR, Bettge M, Thackeray MM, Balasubramanian M. Oxidation state of cross-over manganese species on the graphite electrode of lithium-ion cells. *Phys Chem Chem Phys* 2014;16:6898–902. doi:10.1039/C4CP00764F.
- [41] Wohlfahrt-Mehrens M, Vogler C, Garche J. Aging mechanisms of lithium cathode materials. *J Power Sources* 2004;127:58–64. doi:<https://doi.org/10.1016/j.jpowsour.2003.09.034>.
- [42] Reed J, Ceder G. Role of Electronic Structure in the Susceptibility of Metastable Transition-Metal Oxide Structures to Transformation. *Chem Rev* 2004;104:4513–34. doi:10.1021/cr020733x.
- [43] Rossen E, Jones CDW, Dahn JR. Structure and electrochemistry of Li<sub>x</sub>MnyNi<sub>1-y</sub>O<sub>2</sub>. *Solid State Ionics* 1992;57:311–8. doi:[https://doi.org/10.1016/0167-2738\(92\)90164-K](https://doi.org/10.1016/0167-2738(92)90164-K).
- [44] Winter M, Besenhard JO, Spahr ME, Novák P. Insertion Electrode Materials for Rechargeable Lithium Batteries. *Adv Mater* 1998;10:725–63. doi:10.1002/(SICI)1521-4095(199807)10:10<725::AID-ADMA725>3.0.CO;2-Z.

- [45] Lu Z, Beaulieu LY, Donaberger RA, Thomas CL, Dahn JR. Synthesis, Structure, and Electrochemical Behavior of  $\text{Li}[\text{Ni}_{x}\text{Li}_{1/3-2x/3}\text{Mn}_{2/3-x/3}]\text{O}_2$ . *J Electrochem Soc* 2002;149:A778. doi:10.1149/1.1471541.
- [46] Makimura Y, Ohzuku T. Lithium insertion material of  $\text{LiNi}_{1/2}\text{Mn}_{1/2}\text{O}_2$  for advanced lithium-ion batteries. *J Power Sources* 2003;119–121:156–60. doi:https://doi.org/10.1016/S0378-7753(03)00170-8.
- [47] Yoshio M, Noguchi H, Itoh J ichi, Okada M, Mouri T. Preparation and properties of  $\text{LiCo}_y\text{Mn}_x\text{Ni}_{1-x-y}\text{O}_2$  as a cathode for lithium ion batteries. *J Power Sources* 2000;90:176–81. doi:10.1016/S0378-7753(00)00407-9.
- [48] Liu Z, Yu A, Lee JY. Synthesis and characterization of  $\text{LiNi}_{1-x-y}\text{Co}_x\text{Mn}_y\text{O}_2$  as the cathode materials of secondary lithium batteries. *J Power Sources* 1999;81–82:416–9. doi:10.1016/S0378-7753(99)00221-9.
- [49] Ariyoshi K, Makimura Y, Ohzuku T. Lithium Insertion Materials Having Spinel-Framework Structure for Advanced Batteries. *Lithium Ion Recharge Batter Mater Technol New Appl* 2010;4:11–38. doi:10.1002/9783527629022.ch2.
- [50] Li W, Dolocan A, Oh P, Celio H, Park S, Cho J, et al. Dynamic behaviour of interphases and its implication on high-energy-density cathode materials in lithium-ion batteries. *Nat Commun* 2017;8:14589.
- [51] Fergus JW. Recent developments in cathode materials for lithium ion batteries. *J Power Sources* 2010;195:939–54. doi:10.1016/j.jpowsour.2009.08.089.
- [52] Whittingham MS. Lithium batteries and cathode materials. *Chem Rev* 2004;104:4271–301. doi:10.1021/cr020731c.
- [53] Thomas MGSR, David WIF, Goodenough JB, Groves P. Synthesis and structural characterization of the normal spinel  $\text{Li}[\text{Ni}_2]\text{O}_4$ . *Mater Res Bull* 1985;20:1137–46. doi:https://doi.org/10.1016/0025-5408(85)90087-X.

- [54] Thackeray MM. Structural Considerations of Layered and Spinel Lithiated Oxides for Lithium Ion Batteries. *J Electrochem Soc* 1995;142:2558–63. doi:10.1149/1.2050053.
- [55] Jiao F, Bao J, Hill AH, Bruce PG. Synthesis of Ordered Mesoporous Li-Mn-O Spinel as a Positive Electrode for Rechargeable Lithium Batteries. *Angew Chemie* 2008;120:9857–62. doi:10.1002/ange.200803431.
- [56] Julien CM, Mauger A, Zaghbi K, Groult H. Comparative Issues of Cathode Materials for Li-Ion Batteries. *Inorganics* 2014;2:132–54. doi:10.3390/inorganics2020132.
- [57] Park M, Zhang X, Chung M, Less GB, Sastry AM. A review of conduction phenomena in Li-ion batteries. *J Power Sources* 2010;195:7904–29. doi:10.1016/j.jpowsour.2010.06.060.
- [58] Buchmann I. Battery University by Cadex Electronics Inc. 2017 n.d. [http://batteryuniversity.com/learn/article/types\\_of\\_lithium\\_ion](http://batteryuniversity.com/learn/article/types_of_lithium_ion) (accessed February 9, 2018).
- [59] Tarascon JM, Armand M. Issues and challenges facing rechargeable lithium batteries. *Nature* 2001;414:359–67. doi:10.1038/35104644.
- [60] Hausbrand R, Cherkashinin G, Ehrenberg H, Gröting M, Albe K, Hess C, et al. Fundamental degradation mechanisms of layered oxide Li-ion battery cathode materials: Methodology, insights and novel approaches. *Mater Sci Eng B* 2015;192:3–25. doi:10.1016/j.mseb.2014.11.014.
- [61] Julien C, Mauger A, Zaghbi K, Groult H. Optimization of layered cathode materials for lithium-ion batteries. *Materials (Basel)* 2016;9. doi:10.3390/MA9070595.
- [62] Wei T, Zeng R, Sun Y, Huang Y, Huang K. A reversible and stable flake-like LiCoO<sub>2</sub> cathode for lithium ion batteries. *Chem Commun* 2014;50:1962. doi:10.1039/c3cc48559e.

- [63] Lin F, Markus IM, Nordlund D, Weng T-C, Asta MD, Xin HL, et al. Surface reconstruction and chemical evolution of stoichiometric layered cathode materials for lithium-ion batteries. *Nat Commun* 2014;5:1–9. doi:10.1038/ncomms4529.
- [64] Ben-Kamel K, Amdouni N, Mauger A, Julien CM. Study of the local structure of  $\text{LiNi}_{0.33+\delta}\text{Mn}_{0.33+\delta}\text{Co}_{0.33-2\delta}\text{O}_2$  ( $0.025 \leq \delta \leq 0.075$ ) oxides. *J Alloys Compd* 2012;528:91–8. doi:10.1016/j.jallcom.2012.03.018.
- [65] Lee K-S, Myung S-T, Prakash J, Yashiro H, Sun Y-K. Optimization of microwave synthesis of  $\text{Li}[\text{Ni}_{0.4}\text{Co}_{0.2}\text{Mn}_{0.4}]\text{O}_2$  as a positive electrode material for lithium batteries. *Electrochim Acta* 2008;53:3065–74. doi:10.1016/j.electacta.2007.11.042.
- [66] Shaju KM, Bruce PG. Macroporous  $\text{Li}(\text{Ni}_{1/3}\text{Co}_{1/3}\text{Mn}_{1/3})\text{O}_2$ : A high-rate positive electrode for rechargeable lithium batteries. *J Power Sources* 2007;174:1201–5. doi:10.1016/j.jpowsour.2007.06.091.
- [67] Jouanneau S, Eberman KW, Krause LJ, Dahn JR. Synthesis, Characterization, and Electrochemical Behavior of Improved  $\text{Li}[\text{Ni}_{x}\text{Co}_{1-2x}\text{Mn}_x]\text{O}_2$  ( $0.1 \leq x \leq 0.5$ ). *J Electrochem Soc* 2003;150:A1637. doi:10.1149/1.1622956.
- [68] Arof AK. Characteristics of  $\text{LiMO}_2$  ( $M = \text{Co}, \text{Ni}, \text{Ni}_{0.2}\text{Co}_{0.8}, \text{Ni}_{0.8}\text{Co}_{0.2}$ ) powders prepared from solution of their acetates. *J Alloys Compd* 2008;449:288–91. doi:10.1016/j.jallcom.2005.12.129.
- [69] Julien C, Mauger A, Zaghib K, Groult H. Optimization of Layered Cathode Materials for Lithium-Ion Batteries. *Materials (Basel)* 2016;9.
- [70] Choi J, Manthiram A. Role of Chemical and Structural Stabilities on the Electrochemical Properties of Layered  $\text{LiNi}_{1/3}\text{Mn}_{1/3}\text{Co}_{1/3}\text{O}_2$  Cathodes. *J Electrochem Soc* 2005;152:A1714. doi:10.1149/1.1954927.

- [71] Mohanty D, Kalnaus S, Meisner R a., Rhodes KJ, Li J, Payzant EA, et al. Structural transformation of a lithium-rich  $\text{Li}_{1.2}\text{Co}_{0.1}\text{Mn}_{0.55}\text{Ni}_{0.15}\text{O}_2$  cathode during high voltage cycling resolved by in situ X-ray diffraction. *J Power Sources* 2013;229:239–48. doi:10.1016/j.jpowsour.2012.11.144.
- [72] Pimenta V, Sathiya M, Batuk D, Abakumov AM, Giaume D, Cassaignon S, et al. Synthesis of Li-Rich NMC: A Comprehensive Study. *Chem Mater* 2017;29:9923–36. doi:10.1021/acs.chemmater.7b03230.
- [73] Liu Z, Yu A, Lee JY. Synthesis and characterization of  $\text{LiNi}_{1-x-y}\text{Co}_x\text{Mn}_y\text{O}_2$  as the cathode materials of secondary lithium batteries. *J Power Sources* 1999;81–82:416–9. doi:10.1016/S0378-7753(99)00221-9.
- [74] Zheng J, Kan WH, Manthiram A. Role of Mn content on the electrochemical properties of Nickel-Rich layered  $\text{LiNi}_{0.8-x}\text{Co}_{0.1}\text{Mn}_{0.1+x}\text{O}_2$  (0.0  $x$  0.08) cathodes for lithium-ion batteries. *ACS Appl Mater Interfaces* 2015;7:6926–34. doi:10.1021/acsami.5b00788.
- [75] Sun HH, Choi W, Lee JK, Oh IH, Jung HG. Control of electrochemical properties of nickel-rich layered cathode materials for lithium ion batteries by variation of the manganese to cobalt ratio. *J Power Sources* 2015;275:877–83. doi:10.1016/j.jpowsour.2014.11.075.
- [76] Liu S, Xiong L, He C. Long cycle life lithium ion battery with lithium nickel cobalt manganese oxide (NCM) cathode. *J Power Sources* 2014;261:285–91. doi:10.1016/j.jpowsour.2014.03.083.
- [77] Jung R, Metzger M, Maglia F, Stinner C, Gasteiger HA. Chemical versus Electrochemical Electrolyte Oxidation on NMC111, NMC622, NMC811, LNMO, and Conductive Carbon. *J Phys Chem Lett* 2017;8:4820–5. doi:10.1021/acs.jpcllett.7b01927.
- [78] Erickson EM, Schipper F, Penki TR, Shin J-Y, Erk C, Chesneau F-F, et al. Review—Recent Advances and Remaining Challenges for Lithium Ion Battery Cathodes. *J Electrochem Soc* 2017;164:A6341–8. doi:10.1149/2.0461701jes.

- [79] Nam K-W, Bak S-M, Hu E, Yu X, Zhou Y, Wang X, et al. Combining In Situ Synchrotron X-Ray Diffraction and Absorption Techniques with Transmission Electron Microscopy to Study the Origin of Thermal Instability in Overcharged Cathode Materials for Lithium-Ion Batteries. *Adv Funct Mater* 2013;23:1047–63. doi:10.1002/adfm.201200693.
- [80] Mn L, Co O, Ngala JK, Chernova NA, Ma M, Mamak M, et al. The synthesis, characterization and electrochemical behavior of 2004.
- [81] Lin F, Nordlund D, Li Y, Quan MK, Cheng L, Weng TC, et al. Metal segregation in hierarchically structured cathode materials for high-energy lithium batteries. *Nat Energy* 2016;1:1–8. doi:10.1038/nenergy.2015.4.
- [82] Pierre-Etienne C, David P, Mikael C, Pascal M. Impact of morphological changes of  $\text{LiNi}_{1/3}\text{Mn}_{1/3}\text{Co}_{1/3}\text{O}_2$  on lithium-ion cathode performances. *J Power Sources* 2017;346:13–23. doi:10.1016/j.jpowsour.2017.02.025.
- [83] Wang Y, Sharma N, Su D, Bishop D, Ahn H, Wang G. High capacity spherical  $\text{Li}[\text{Li}_{0.24}\text{Mn}_{0.55}\text{Co}_{0.14}\text{Ni}_{0.07}]\text{O}_2$  cathode material for lithium ion batteries. *Solid State Ionics* 2013;233:12–9. doi:10.1016/j.ssi.2012.12.003.
- [84] Guo J, Jiao LF, Yuan HT, Li HX, Zhang M, Wang YM. Effect of synthesis condition on the structural and electrochemical properties of  $\text{Li}[\text{Ni}_{1/3}\text{Mn}_{1/3}\text{Co}_{1/3}]\text{O}_2$  prepared by the metal acetates decomposition method. *Electrochim Acta* 2006;51:3731–5. doi:10.1016/j.electacta.2005.10.037.
- [85] Yang F, Liu Y, Martha SK, Wu Z, Andrews JC, Ice GE, et al. Nanoscale morphological and chemical changes of high voltage lithium-manganese rich NMC composite cathodes with cycling. *Nano Lett* 2014;14:4334–41. doi:10.1021/nl502090z.
- [86] Son JT, Cairns EJ. Characterization of  $\text{LiCoO}_2$  coated  $\text{Li}_{1.05}\text{Ni}_{0.35}\text{Co}_{0.25}\text{Mn}_{0.4}\text{O}_2$  cathode material for lithium secondary cells. *J Power Sources* 2007;166:343–7. doi:https://doi.org/10.1016/j.jpowsour.2006.12.069.

- [87] Kim H-S, Kong M, Kim K, Kim I-J, Gu H-B. Effect of carbon coating on  $\text{LiNi}_{1/3}\text{Mn}_{1/3}\text{Co}_{1/3}\text{O}_2$  cathode material for lithium secondary batteries. *J Power Sources* 2007;171:917–21. doi:10.1016/j.jpowsour.2007.06.028.
- [88] Kim Y, Kim HS, Martin SW. Synthesis and electrochemical characteristics of  $\text{Al}_2\text{O}_3$ -coated  $\text{LiNi}_{1/3}\text{Co}_{1/3}\text{Mn}_{1/3}\text{O}_2$  cathode materials for lithium ion batteries. *Electrochim Acta* 2006;52:1316–22. doi:https://doi.org/10.1016/j.electacta.2006.07.033.
- [89] Na S-H, Kim H-S, Moon S-I. The effect of Si doping on the electrochemical characteristics of  $\text{LiNi}_x\text{Mn}_y\text{Co}_{(1-x-y)}\text{O}_2$ . *Solid State Ionics* 2005;176:313–7. doi:http://dx.doi.org/10.1016/j.ssi.2004.08.016.
- [90] Ding Z, Xu M, Liu J, Huang Q, Chen L, Wang P, et al. Understanding the Enhanced Kinetics of Gradient-Chemical-Doped Lithium-Rich Cathode Material. *ACS Appl Mater Interfaces* 2017;9:20519–26. doi:10.1021/acsami.7b02944.
- [91] Wilcox J, Patoux S, Doeff M. Structure and Electrochemistry of  $\text{LiNi}_{1/3}\text{Co}_{1/3-y}\text{MyMn}_{1/3}\text{O}_2$  (M = Ti, Al, Fe) Positive Electrode Materials. *J Electrochem Soc* 2009;156:A192–8. doi:10.1149/1.3056109.
- [92] Zhang Y-P, Liang E-Q, Wang J-X, Yu B-J, Wang C-Y, Li M-W. Effect of Aluminum Doping on the Stability of Lithium-Rich Layered Oxide  $\text{Li}[\text{Li}_{0.23}\text{Ni}_{0.15}\text{Mn}_{0.52}\text{Al}_{0.10}]\text{O}_2$  as Cathode Material. *Int J Electrochem Sci* 2017;12:9051–60.
- [93] Wang C-C, Lin Y-C, Chou P-H. Mitigation of layer to spinel conversion of a lithium-rich layered oxide cathode by substitution of Al in a lithium ion battery. *RSC Adv* 2015;5:68919–28.
- [94] Li Y, Li Y, Zhong S, Li F, Yang J. Synthesis and Electrochemical Properties of Y-Doped  $\text{LiNi}_{1/3}\text{Mn}_{1/3}\text{Co}_{1/3}\text{O}_2$  Cathode Materials for Li-Ion Battery. *Integr Ferroelectr* 2011;127:150–6. doi:10.1080/10584587.2011.575736.

- [95] Li J Bin, Xu YL, Du XF, Sun XF, Xiong LL. Improved electrochemical stability of Zn-doped  $\text{LiNi}_{1/3}\text{Co}_{1/3}\text{Mn}_{1/3}\text{O}_2$  cathode materials. *Wuli Huaxue Xuebao/ Acta Phys - Chim Sin* 2012;28:1899–905. doi:10.3866/PKU.WHXB201205152.
- [96] Wei X, Yang P, Li H, Wang S, Xing Y, Liu X, et al. Synthesis and properties of mesoporous Zn-doped  $\text{Li}_{1.2}\text{Mn}_{0.54}\text{Co}_{0.13}\text{Ni}_{0.13}\text{O}_2$  as cathode materials by a MOFs-assisted solvothermal method. *RSC Adv* 2017;7:35055–9. doi:10.1039/C7RA05106A.
- [97] Liu L, Sun K, Zhang N, Yang T. Improvement of high-voltage cycling behavior of  $\text{Li}(\text{Ni}_{1/3}\text{Co}_{1/3}\text{Mn}_{1/3})\text{O}_2$  cathodes by Mg, Cr, and Al substitution. *J Solid State Electrochem* 2009;13:1381–6. doi:10.1007/s10008-008-0695-z.
- [98] Büyükburç A, Aydinol MK. Effect of Cr and Mo doping on the electrochemical properties of freeze-dried  $\text{LiCoO}_2$ . *Int J Mater Res* 2014;105:983–91. doi:10.3139/146.111104.
- [99] Schipper F, Dixit M, Kovacheva D, Talianker M, Haik O, Grinblat J, et al. Stabilizing nickel-rich layered cathode materials by a high-charge cation doping strategy: zirconium-doped  $\text{LiNi}_{0.6}\text{Co}_{0.2}\text{Mn}_{0.2}\text{O}_2$ . *J Mater Chem A* 2016;4:16073–84. doi:10.1039/C6TA06740A.
- [100] Ates MN, Jia Q, Shah A, Busnaina A, Mukerjee S, Abraham KM. Mitigation of Layered to Spinel Conversion of a Li-Rich Layered Metal Oxide Cathode Material for Li-Ion Batteries. *J Electrochem Soc* 2013;161:A290–301. doi:10.1149/2.040403jes.
- [101] Schipper F, Nayak P, Erickson E, Amalraj S, Srur-Lavi O, Penki T, et al. Study of Cathode Materials for Lithium-Ion Batteries: Recent Progress and New Challenges. *Inorganics* 2017;5:32. doi:10.3390/inorganics5020032.
- [102] Prakasha KR, Sathish M, Bera P, Prakash AS. Mitigating the Surface Degradation and Voltage Decay of  $\text{Li}_{1.2}\text{Ni}_{0.13}\text{Mn}_{0.54}\text{Co}_{0.13}\text{O}_2$  Cathode Material through Surface Modification Using  $\text{Li}_2\text{ZrO}_3$ . *ACS Omega* 2017;2:2308–16. doi:10.1021/acsomega.7b00381.

- [103] Ju SH, Kim DY, Kang YC. The characteristics of Li(Ni<sub>1/3</sub>Co<sub>1/3</sub>Mn<sub>1/3</sub>)O<sub>2</sub> particles prepared from precursor particles with spherical shape obtained by spray pyrolysis. *Ceram Int* 2007;33:1093–8. doi:10.1016/j.ceramint.2006.03.013.
- [104] Luo X, Wang X, Liao L, Gamboa S, Sebastian PJ. Synthesis and characterization of high tap-density layered Li[Ni<sub>1/3</sub>Co<sub>1/3</sub>Mn<sub>1/3</sub>]O<sub>2</sub> cathode material via hydroxide co-precipitation. *J Power Sources* 2006;158:654–8. doi:10.1016/j.jpowsour.2005.09.047.
- [105] Lin Y-K, Lu C-H. Preparation and electrochemical properties of layer-structured LiNi<sub>1/3</sub>Co<sub>1/3</sub>Mn<sub>1/3</sub>-yAl<sub>y</sub>O<sub>2</sub>. *J Power Sources* 2009;189:353–8. doi:10.1016/j.jpowsour.2008.08.072.
- [106] Zhang Y, Wu X, Lin Y, Wang D, Zhang C, He D. Synthesis of LiNi<sub>1/3</sub>Co<sub>1/3</sub>Mn<sub>1/3</sub>O<sub>2</sub> cathode material by a modified sol-gel method for lithium-ion battery. *J Sol-Gel Sci Technol* 2013;68:169–74. doi:10.1007/s10971-013-3148-9.
- [107] Tan L, Liu H. High rate charge-discharge properties of LiNi<sub>1/3</sub>Co<sub>1/3</sub>Mn<sub>1/3</sub>O<sub>2</sub> synthesized via a low temperature solid-state method. *Solid State Ionics* 2010;181:1530–3. doi:https://doi.org/10.1016/j.ssi.2010.08.016.
- [108] Liang Y, Han X, Zhou X, Sun J, Zhou Y. Significant improved electrochemical performance of Li(Ni<sub>1/3</sub>Co<sub>1/3</sub>Mn<sub>1/3</sub>)O<sub>2</sub> cathode on volumetric energy density and cycling stability at high rate. *Electrochem Commun* 2007;9:965–70. doi:10.1016/j.elecom.2006.11.039.
- [109] He Y-S, Ma Z-F, Liao X-Z, Jiang Y. Synthesis and characterization of submicron-sized LiNi<sub>1/3</sub>Co<sub>1/3</sub>Mn<sub>1/3</sub>O<sub>2</sub> by a simple self-propagating solid-state metathesis method. *J Power Sources* 2007;163:1053–8. doi:10.1016/j.jpowsour.2006.09.061.

- [110] Liu Z, Hu G, Peng Z, Deng X, Liu Y. Synthesis and characterization of layered  $\text{Li}(\text{Ni}_{1/3}\text{Mn}_{1/3}\text{Co}_{1/3})\text{O}_2$  cathode materials by spray-drying method. *Trans Nonferrous Met Soc China* 2007;17:291–5. doi:10.1016/S1003-6326(07)60087-9.
- [111] Lin B, Wen Z, Gu Z, Xu X. Preparation and electrochemical properties of  $\text{Li}[\text{Ni}_{1/3}\text{Co}_{1/3}\text{Mn}_{1-x/3}\text{Zr}_{x/3}]\text{O}_2$  cathode materials for Li-ion batteries. *J Power Sources* 2007;174:544–7. doi:https://doi.org/10.1016/j.jpowsour.2007.06.125.
- [112] Nithya C, Thirunakaran R, Sivashanmugam A, Gopukumar S. Microwave synthesis of novel high voltage (4.6 V) high capacity  $\text{LiCu}_x\text{Co}_{1-x}\text{O}_2$  cathode material for lithium rechargeable cells. *J Power Sources* 2011;196:6788–93. doi:10.1016/j.jpowsour.2010.10.053.
- [113] Ting-Kuo Fey G, Chang C-S, Kumar TP. Synthesis and surface treatment of  $\text{LiNi}_{1/3}\text{Co}_{1/3}\text{Mn}_{1/3}\text{O}_2$  cathode materials for Li-ion batteries. *J Solid State Electrochem* 2010;14:17–26. doi:10.1007/s10008-008-0772-3.
- [114] Taniguchi I. Powder properties of partially substituted  $\text{LiM}_x\text{Mn}_{2-x}\text{O}_4$  (M=Al, Cr, Fe and Co) synthesized by ultrasonic spray pyrolysis. *Mater Chem Phys* 2005;92:172–9. doi:https://doi.org/10.1016/j.matchemphys.2005.01.020.
- [115] Zhang S, Qiu X, He Z, Weng D, Zhu W. Nanoparticled  $\text{Li}(\text{Ni}_{1/3}\text{Co}_{1/3}\text{Mn}_{1/3})\text{O}_2$  as cathode material for high-rate lithium-ion batteries. *J Power Sources* 2006;153:350–3. doi:10.1016/j.jpowsour.2005.05.021.
- [116] Ding Y, Zhang P, Jiang Y, Gao D. Effect of rare earth elements doping on structure and electrochemical properties of  $\text{LiNi}_{1/3}\text{Co}_{1/3}\text{Mn}_{1/3}\text{O}_2$  for lithium-ion battery. *Solid State Ionics* 2007;178:967–71. doi:10.1016/j.ssi.2007.04.012.
- [117] Rao KJ, Vaidyanathan B, Ganguli M, Ramakrishnan PA. Synthesis of Inorganic Solids Using Microwaves. *Chem Mater* 1999;11:882–95. doi:10.1021/cm9803859.

- [118] Yan H, Huang X, Li H, Chen L. Electrochemical study on LiCoO<sub>2</sub> synthesized by microwave energy. *Solid State Ionics* 1998;115:11–5.
- [119] Kalyani P, Kalaiselvi N, Renganathan NG. Microwave-assisted synthesis of LiNiO<sub>2</sub>—a preliminary investigation. *J Power Sources* 2003;123:53–60. doi:10.1016/S0378-7753(03)00458-0.
- [120] Nakayama M. Grain size control of LiMn<sub>2</sub>O<sub>4</sub> cathode material using microwave synthesis method. *Solid State Ionics* 2003;164:35–42. doi:10.1016/j.ssi.2003.08.048.
- [121] Bao S-J, Liang Y-Y, Zhou W-J, He B-L, Li H-L. Synthesis and electrochemical properties of LiAl<sub>0.1</sub>Mn<sub>1.9</sub>O<sub>4</sub> by microwave-assisted sol-gel method. *J Power Sources* 2006;154:239–45. doi:10.1016/j.jpowsour.2005.03.220.
- [122] Jang H, Seong C, Suh Y, Kim H, Lee C. Synthesis of Lithium-Cobalt Oxide Nanoparticles by Flame Spray Pyrolysis. *Aerosol Sci Technol* 2004;38:1027–32. doi:10.1080/027868290524016.
- [123] Yilmaz M, Turgut G, Aydin S, Ertugrul M. LiCoO<sub>2</sub> Structures by Spray Pyrolysis Technique for Rechargeable Li-ion Battery 1. *JChemSocPak* 2012;34:283.
- [124] Kim SH, Kim CS. Improving the rate performance of LiCoO<sub>2</sub> by Zr doping. *J Electroceramics* 2009;23:254–7. doi:10.1007/s10832-008-9414-5.
- [125] Gao F, Tang Z, Xue J. Preparation and characterization of nano-particle LiFePO<sub>4</sub> and LiFePO<sub>4</sub>/C by spray-drying and post-annealing method. *Electrochim Acta* 2007;53:1939–44. doi:10.1016/j.electacta.2007.08.048.
- [126] Ju SH, Kim DY, Jo EB, Kang YC. LiMn<sub>2</sub>O<sub>4</sub> particles prepared by spray pyrolysis from spray solution with citric acid and ethylene glycol. *J Mater Sci* 2007;42:5369–74. doi:10.1007/s10853-006-0903-0.

- [127] Sorensen CM, Li Q, Xu HK, Tang ZX, Klabunde KJ, Hadjipanayis GC. *Aerosol Spray Pyrolysis Synthesis Techniques*. Nanophase Mater., Dordrecht: Springer Netherlands; 1994, p. 109–16. doi:10.1007/978-94-011-1076-1\_15.
- [128] Okuyama K, Shimada M, Adachi M, Tohge N. Preparation of ultrafine superconductive Bi<sub>2</sub>CaSr<sub>2</sub>CU<sub>2</sub>O<sub>x</sub> particles by metalorganic chemical vapor deposition. *J Aerosol Sci* 1993;24:357–66. doi:10.1016/0021-8502(93)90008-W.
- [129] Bakenov Z, Taniguchi I. Cathode Materials for Lithium-Ion Batteries. *Lithium-Ion Batter Adv Mater Technol* 2011:51.
- [130] Che S, Sakurai O, Shinozaki K, Mizutani N. Particle structure control through intraparticle reactions by spray pyrolysis. *J Aerosol Sci* 1998;29:271–8. doi:10.1016/S0021-8502(97)10012-X.
- [131] Jung DS, Park S Bin, Kang YC. Design of particles by spray pyrolysis and recent progress in its application. *Korean J Chem Eng* 2010;27:1621–45. doi:10.1007/s11814-010-0402-5.
- [132] Chen Q, Wang J, Zhang Y, Lu J. Activation energy study of intrinsic microcrystalline silicon thin film prepared by VHF-PECVD. *Optik (Stuttg)* 2016;127:7312–8. doi:10.1016/j.ijleo.2016.05.062.
- [133] Nie P, Xu G, Jiang J, Dou H, Wu Y, Zhang Y, et al. Aerosol-Spray Pyrolysis toward Preparation of Nanostructured Materials for Batteries and Supercapacitors. *Small Methods* 2018;2:1700272. doi:10.1002/smt.201700272.
- [134] Lutterotti L, Matthies S, Wenk HR. MAUD: a friendly Java program for material analysis using diffraction. *News1 CPD* 1999;21:14–5.
- [135] Büyükburç A. Development and characterization of high energy cathode materials for lithium-ion batteries. Middle East Technical University, 2013.

- [136] Savaş C. Ultrasonic Sound Assisted Processing And Characterization Of Li(Ni-Co-Al) Oxide As Cathode Active Material For Li-Ion Batteries. Middle East Technical University, 2017.
- [137] Barsoukov E, Macdonald JR. Impedance Spectroscopy. Hoboken, NJ, USA: John Wiley & Sons, Inc.; 2005. doi:10.1002/0471716243.
- [138] Illig JN. Physically based Impedance Modelling of Lithium-ion Cells. 2014. doi:10.5445/KSP/1000042281.
- [139] Hyttinen N, Otkjær R V., Iyer S, Kjaergaard HG, Rissanen MP, Wennberg PO, et al. Computational Comparison of Different Reagent Ions in the Chemical Ionization of Oxidized Multifunctional Compounds. *J Phys Chem A* 2018;122:269–79. doi:10.1021/acs.jpca.7b10015.
- [140] Shunmugasundaram R, Senthil Arumugam R, Harris KJ, Goward GR, Dahn JR. A Search for Low-Irreversible Capacity and High-Reversible Capacity Positive Electrode Materials in the Li-Ni-Mn-Co Pseudoquaternary System. *Chem Mater* 2016;28:55–66. doi:10.1021/acs.chemmater.5b02104.
- [141] Choi HW, Kim SJ, Rim YH, Yang YS. Effect of Lithium Deficiency on Lithium-Ion Battery Cathode  $\text{Li}_x\text{Ni}_{0.5}\text{Mn}_{1.5}\text{O}_4$ . *J Phys Chem C* 2015;119:27192–9. doi:10.1021/acs.jpcc.5b06501.
- [142] Aurbach D. Review of selected electrode–solution interactions which determine the performance of Li and Li ion batteries. *J Power Sources* 2000;89:206–18. doi:10.1016/S0378-7753(00)00431-6.
- [143] Schipper F, Nayak P, Erickson E, Amalraj S, Srur-Lavi O, Penki T, et al. Study of Cathode Materials for Lithium-Ion Batteries: Recent Progress and New Challenges. *Inorganics* 2017;5:32. doi:10.3390/inorganics5020032.
- [144] Shannon RD. Revised effective ionic radii and systematic studies of interatomic distances in halides and chalcogenides. *Acta Crystallogr Sect A* 1976;32:751–67. doi:10.1107/S0567739476001551.

- [145] R.D.Shannon, C.T.Prewitt. Effective ionic radii in oxides and fluorides. *Acta Cryst* 1969;B25:925. doi:10.1007/s13398-014-0173-7.2.
- [146] Wen Y, Xiao D, Liu X, Gu L. Microstructure dynamics of rechargeable battery materials studied by advanced transmission electron microscopy. *NPG Asia Mater* 2017;9:e360-12. doi:10.1038/am.2017.19.
- [147] Lin F, Markus IM, Doeff MM, Xin HL. Chemical and structural stability of lithium-ion battery electrode materials under electron beam. *Sci Rep* 2014;4:5694. doi:10.1038/srep05694.
- [148] Yan P, Nie A, Zheng J, Zhou Y, Lu D, Zhang X, et al. Evolution of Lattice Structure and Chemical Composition of the Surface Reconstruction Layer in Li 1.2 Ni 0.2 Mn 0.6 O 2 Cathode Material for Lithium Ion Batteries. *Nano Lett* 2015;15:514–22. doi:10.1021/nl5038598.
- [149] Shchukarev A, Korolkov D. XPS Study of group IA carbonates. *Open Chem* 2004;2:347–62. doi:10.2478/BF02475578.
- [150] Nohira H, Tsai W, Besling W, Young E, Petry J, Conard T, et al. Characterization of ALCVD-Al<sub>2</sub>O<sub>3</sub> and ZrO<sub>2</sub> layer using X-ray photoelectron spectroscopy. *J Non Cryst Solids* 2002;303:83–7. doi:10.1016/S0022-3093(02)00970-5.
- [151] Bodenes L, Dedryvere R, Martinez H, Fischer F, Tessier C, Peres J-P. Lithium-Ion Batteries Working at 85 C: Aging Phenomena and Electrode/Electrolyte Interfaces Studied by XPS. *J Electrochem Soc* 2012;159:A1739–46. doi:10.1149/2.061210jes.
- [152] Ilton ES, Post JE, Heaney PJ, Ling FT, Kerisit SN. XPS determination of Mn oxidation states in Mn (hydr)oxides. *Appl Surf Sci* 2016;366:475–85. doi:10.1016/j.apsusc.2015.12.159.

- [153] Biesinger MC, Payne BP, Grosvenor AP, Lau LWM, Gerson AR, Smart RSC. Resolving surface chemical states in XPS analysis of first row transition metals, oxides and hydroxides: Cr, Mn, Fe, Co and Ni. *Appl Surf Sci* 2011;257:2717–30. doi:10.1016/j.apsusc.2010.10.051.
- [154] Baggetto L, Mohanty D, Meisner RA, Bridges CA, Daniel C, Wood III DL, et al. Degradation mechanisms of lithium-rich nickel manganese cobalt oxide cathode thin films. *RSC Adv* 2014;4:23364. doi:10.1039/c4ra03674c.
- [155] Baltrusaitis J, Mendoza-Sanchez B, Fernandez V, Veenstra R, Dukstiene N, Roberts A, et al. Generalized molybdenum oxide surface chemical state XPS determination via informed amorphous sample model. *Appl Surf Sci* 2015;326:151–61. doi:10.1016/j.apsusc.2014.11.077.
- [156] McCreary KM, Hanbicki AT, Jernigan GG, Culbertson JC, Jonker BT. Synthesis of Large-Area WS<sub>2</sub> monolayers with Exceptional Photoluminescence. *Sci Rep* 2016;6:19159. doi:10.1038/srep19159.
- [157] Biesinger MC. Advanced analysis of copper X-ray photoelectron spectra. *Surf Interface Anal* 2017;49:1325–34. doi:10.1002/sia.6239.
- [158] Zatsopin DA, Galakhov VR, Korotin MA, Fedorenko V V., Kurmaev EZ, Bartkowski S, et al. Valence states of copper ions and electronic structure of LiCu<sub>2</sub>O<sub>2</sub>. *Phys Rev B* 1998;57:4377–81. doi:10.1103/PhysRevB.57.4377.
- [159] Bettge M, Li Y, Gallagher K, Zhu Y, Wu Q, Lu W, et al. Voltage Fade of Layered Oxides: Its Measurement and Impact on Energy Density. *J Electrochem Soc* 2013;160:A2046–55. doi:10.1149/2.034311jes.
- [160] Smith AJ, Burns JC, Dahn JR. A High Precision Study of the Coulombic Efficiency of Li-Ion Batteries. *Electrochem Solid-State Lett* 2010;13:A177. doi:10.1149/1.3487637.

- [161] Yang F, Wang D, Zhao Y, Tsui K-L, Bae SJ. A study of the relationship between coulombic efficiency and capacity degradation of commercial lithium-ion batteries. *Energy* 2018;145:486–95. doi:10.1016/j.energy.2017.12.144.
- [162] An SJ, Li J, Du Z, Daniel C, Wood DL. Fast formation cycling for lithium ion batteries. *J Power Sources* 2017;342:846–52. doi:10.1016/j.jpowsour.2017.01.011.
- [163] Lengyel M. Optimization of layered battery cathode materials synthesized via spray pyrolysis. All Theses and Dissertations (ETDs)., 2014.
- [164] Aurbach D, Zaban A. Impedance spectroscopy of lithium electrodes: Part 1. General behavior in propylene carbonate solutions and the correlation to surface chemistry and cycling efficiency. *J Electroanal Chem* 1993;348:155–79. doi:https://doi.org/10.1016/0022-0728(93)80129-6.
- [165] Aurbach D, Zaban A. Impedance spectroscopy of lithium electrodes: Part 2. The behaviour in propylene carbonate solutions — the significance of the data obtained. *J Electroanal Chem* 1994;367:15–25. doi:https://doi.org/10.1016/0022-0728(93)02998-W.
- [166] Song J, Bazant MZ. Effects of Nanoparticle Geometry and Size Distribution on Diffusion Impedance of Battery Electrodes. *J Electrochem Soc* 2012;160:A15–24. doi:10.1149/2.023301jes.

## APPENDICES

### A. PERMISSION LICENSES

#### ELSEVIER LICENSE

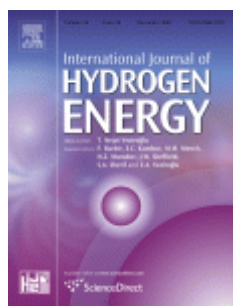


4/6/2018

RightsLink®



Rightslink® by Copyright Clearance Center



**Title:** Development and characterization of layered Li(NixMnyCo1-x-y)O2 cathode materials for lithium ion batteries

**Author:** Berke Pişkin, Mehmet Kadri Aydinol

**Publication:** International Journal of Hydrogen Energy

**Publisher:** Elsevier

**Date:** 22 June 2016

© 2016 Hydrogen Energy Publications LLC. Published by Elsevier Ltd. All rights reserved.

<a href="#">LOGIN</a>
If you're a <a href="#">copyright.com</a> user, you can login to RightsLink using your copyright.com credentials.
Already a <a href="#">RightsLink</a> user or want to <a href="#">learn more?</a>

Please note that, as the author of this Elsevier article, you retain the right to include it in a thesis or dissertation, provided it is not published commercially. Permission is not required, but please ensure that you reference the journal as the original source. For more information on this and on your other retained rights, please visit: <https://www.elsevier.com/about/our-business/policies/copyright#Author-rights>



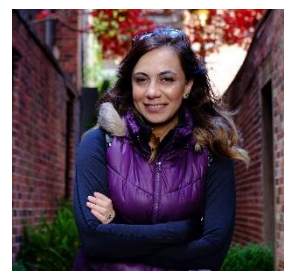
Copyright © 2018 [Copyright Clearance Center, Inc.](#) All Rights Reserved. [Privacy statement](#). [Terms and Conditions](#).  
Comments? We would like to hear from you. E-mail us at [customercare@copyright.com](mailto:customercare@copyright.com)



## CURRICULUM VITAE

### PERSONAL INFORMATION

Last Name, Name : Pişkin, Berke  
Nationality : Turkish (T.C.)  
Date and Place of Birth : 09 February 1986, Konya  
Marital Status : Married  
Voice : +90 534-424 20 45  
E-mail : berkepiskin@mu.edu.tr



### EDUCATION

Degree	Institution	Year of Graduation
Ph.D.	Middle East Technical University	2018
M.Sc.	Middle East Technical University	2012
B.Sc.	Anadolu University	2009

### WORK EXPERIENCE

Year	Place	Enrollment
2018-present	MSKU, Metallurgical and Materials Eng.	Research Assistant
2012-2018	METU, Metallurgical and Materials Eng.	Research Assistant
Sept.2016- Sept.2017	Dept. of Materials Science and Eng., Massachusetts Institute of Technology (MIT)	Visiting Scholar
2011-2012	MSKU, Metallurgical and Materials Eng.	Research Assistant

## PUBLICATIONS

Köse Özgün K., **Pişkin B.**, Aydınol M.K., Chemical and Structural Optimization of ZnCl<sub>2</sub> Activated Carbons via High Temperature CO<sub>2</sub> Treatment for EDLC Applications”, Int. J. Hydrogen Energy, 2018, doi: 10.1016/j.ijhydene.2018.03.222

**Pişkin B.**, Savaş Uygur C., Aydınol M.K., Mo Doping of Layered Li(Ni<sub>x</sub>Mn<sub>y</sub>Co<sub>1-x-y-z</sub>M<sub>z</sub>)O<sub>2</sub> Cathode Materials for Lithium Ion Batteries, International Journal of Energy Research, 2017, accepted

Savaş Uygur C., **Pişkin B.**, Aydınol M.K., Electrochemical and Structural Behavior of Ultrasonic Sound Assisted Processed Li<sub>x</sub>(Ni<sub>0.80</sub>Co<sub>0.15</sub>Al<sub>0.05</sub>)O<sub>2</sub> Cathode Active Materials for Lithium-Ion Batteries to Ionics, 2018, submitted

**Pişkin B.**, Aydınol M.K., “Development and Characterization of Layered Li(Ni<sub>x</sub>Mn<sub>y</sub>Co<sub>1-x-y</sub>)O<sub>2</sub>, Cathode Materials for Lithium Ion Batteries”, Int. J. Hydrogen Energy 41, 9852–9859, 2016.